The Dissertation Committee for Haixia Mei Certifies that this is the approved version of the following dissertation:

FRACTURE AND DELAMINATION OF ELASTIC THIN FILMS ON COMPLIANT SUBSTRATES: MODELING AND SIMULATIONS

Committee:

Rui Huang, Supervisor

Kenneth Liechti

Chad Landis

Mark Mear

Paul Ho

FRACTURE AND DELAMINATION OF ELASTIC THIN FILMS ON COMPLIANT SUBSTRATES: MODELING AND SIMULATIONS

by

Haixia Mei, B.E., M.E.

Dissertation

Presented to the Faculty of the Graduate School of

The University of Texas at Austin

in Partial Fulfillment

of the Requirements

for the Degree of

Doctor of Philosophy

The University of Texas at Austin

August, 2011

Dedication

To my family

Acknowledgements

On completion of this dissertation, I owe my gratitude to all those people who have made this possible.

First and foremost, I would like to express my sincerest appreciation to my supervisor, Dr. Rui Huang, for his continuous guidance, patience, and support during my doctoral study. Dr. Huang is a highly esteemed scholar and a gracious mentor who encouraged me to grow as a serious mechanician and an independent thinker. His encouragement and advice will definitely keep leading me throughout my future career. I must also thank Dr. Kenneth Liechti and his student Shravan Gowrishankar. It is a great experience working closely with them in the joint project. I would also like to extend my thanks to Dr. Chad Landis for his professional help on my research. I am honored to have Dr. Kenneth Liechti, Dr. Mark Mear, Dr. Chad Landis, and Dr. Paul Ho as the members of my Ph.D. committees, and I would like to gratefully thank them for their commitments and help.

I would like to especially acknowledge my friends, Se-hyuk Im, Min Kyoo Kang, Suk-Kyu Ryu, Ying Tian and many others who have helped me through these years. Special thanks to Suk-Kyu Ryu, Guanyu Hu and Xun Guo for their assistance during my job hunting.

Finally, I would like to express my heartily appreciation to my family. Without their unending support, encouragement, and unwavering love, the completion of this work would not have been possible. I owe them everything.

Fracture and Delamination of Elastic Thin Films on Compliant Substrates: Modeling and Simulations

Haixia Mei, Ph.D.

The University of Texas at Austin, 2011

Supervisor: Rui Huang

Different fracture modes have been observed in thin film structures. One common approach used in fracture analysis is based on the principle of linear elastic fracture mechanics (LEFM), which assumes pre-existing cracks and treats the materials as linear elastic except for the damage zone around the crack tip. Alternatively, a nonlinear cohesive zone model (CZM) can be used to simulate both nucleation and growth of cracks. In this dissertation, the approaches of LEFM and CZM are employed to study fracture and delamination of elastic thin films on compliant substrates under various loading conditions.

First, compression-induced buckling of elastic thin films on elastic compliant substrates is studied by analytical and numerical methods. The critical condition for onset of buckling instability without and with a pre-existing delamination crack is predicted. By comparing the critical strains, a map for the initial buckling modes is constructed with respect to the film/substrate stiffness ratio and the interfacial defect size. For an elastic film on a highly compliant substrate, nonlinear post-buckling analysis is conducted to simulate concomitant wrinkling and buckle-delamination, with a long-range interaction between the two buckling modes through the compliant substrate. By using a layer of cohesive elements for the interface, progressive co-evolution of wrinkling and

delamination is simulated. In particular, the effects of interfacial properties (strength and toughness) on the initiation and propagation of wrinkle-induced interfacial delamination are examined.

Next, using a set of finite element models, the effects of interfacial delamination and substrate penetration on channel cracking of brittle thin films are analyzed. It is found that, depending on the elastic mismatch and the toughness of interface and substrate, a channel crack may grow with interfacial delamination and/or substrate cracking. By comparing the effective energy release rates, the competition between the two fracture modes is discussed. Cohesive zone modeling is then employed to simulate nucleation and growth of delamination and penetration from the root of a channel crack. By comparing the results from the approaches of LEFM and CZM, the characteristic fracture resistance from small-scale bridging to large-scale bridging is identified.

Finally, to determine the nonlinear traction-separation relation for cohesive zone modeling of a bimaterial interface, a hybrid approach is developed by combining experimental measurements and finite element simulations. In particular, both analytical and numerical models for wedge-loaded double cantilever beam specimens are developed. A two-step fitting procedure is proposed to determine the interface toughness and strength based on the measurements of the steady-state crack length and the local crack opening displacements.

Table of Contents

List of Figures

Chapter 1

Introduction

1.1 Background and motivation

Thin film materials on mechanically compliant substrates are used in a wide range of technological applications. For example, low-k dielectric materials with increasingly low stiffness and strength are required for high performance integrated circuits in microelectronics [1, 2]. In stretchable electronics [3-6], compliant polymer substrates have to be used extensively along with mechanically stiffer films for functional devices and interconnects. Similar layered structures integrating soft and hard materials are abundant in nature [7, 8]. Due to the sharp contrast in their mechanical properties, the mechanical interaction between a stiff film and a compliant substrate leads to a rich variety of phenomena that either limit or inspire practical applications of the hybrid system. Among others, buckling and cracking of thin films are commonly observed. They represent two major failure mechanisms for many applications. On the other hand, they have also been exploited as enabling mechanisms for a variety of novel applications [9-13].

Figure 1.1 shows optical images of various wrinkle patterns by Bowden et al. [9]. A thin metal film was deposited on heated PDMS substrate. Upon cooling, a biaxial compressive stress was induced in the film and caused surface wrinkling as a result of mechanical instability. To generate ordered wrinkle patterns, pre-defined bas-relief

surface patterns were introduced. Alternatively, by mechanically applying uniaxial compression, parallel wrinkles (with defects) can be generated, as shown in Fig. 1.2. With a simple mechanics model that relates the wrinkle wavelength to the elastic modulus of the thin film, the wrinkling phenomenon has been used in thin film metrology to measure the elastic moduli of thin films [14, 15].

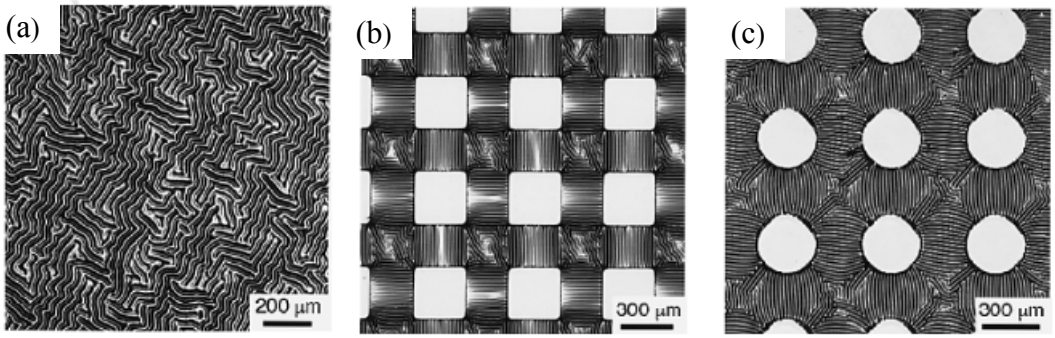

Figure 1.1: Optical images of wrinkle patterns [9].

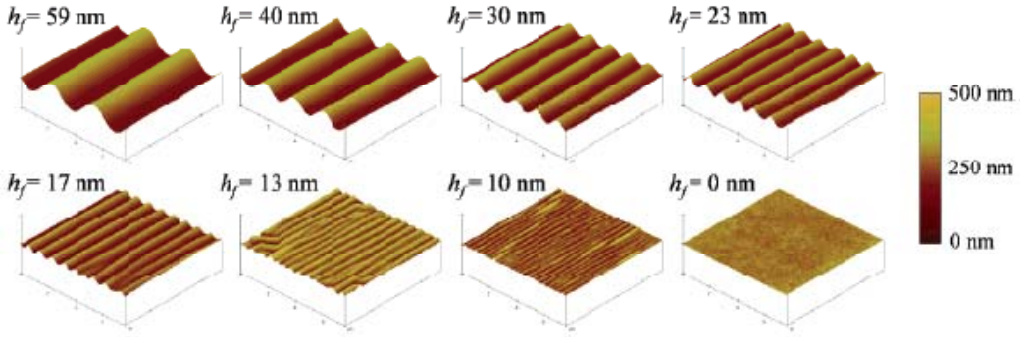

Figure 1.2: AFM height images of parallel wrinkle patterns of PS films supported on PDMS for a series of film thicknesses (h_f). For all images, the scan size is 7.5 μm × 7.5 μm and the height scale is 500 nm. Adopted from Stafford et al. [16].

Buckling of thin films has also been observed along with interfacial delamination.

Figure 1.3a shows a telephone cord blister due to buckle-delamination of a diamond-like carbon (DLC) film on a glass substrate [17]. On a compliant substrate, both surface wrinkling (without delamination) and buckle-delamination have been observed [18-20]. Figure 1.3b shows an optical micrograph of a PS film ($E_f \approx 4$ GPa, $h_f \approx 300$ nm) on PDMS ($E_s \approx 0.5$ MPa), with both surface wrinkling and buckle-delamination [21]. Apparently, the interfacial property plays an important role in determining the buckling mode (i.e., with or without delamination). It has been suggested that measurement of the buckling profile (along with the delamination width) may provide a convenient method for characterizing interfacial adhesion [20, 22, 23].

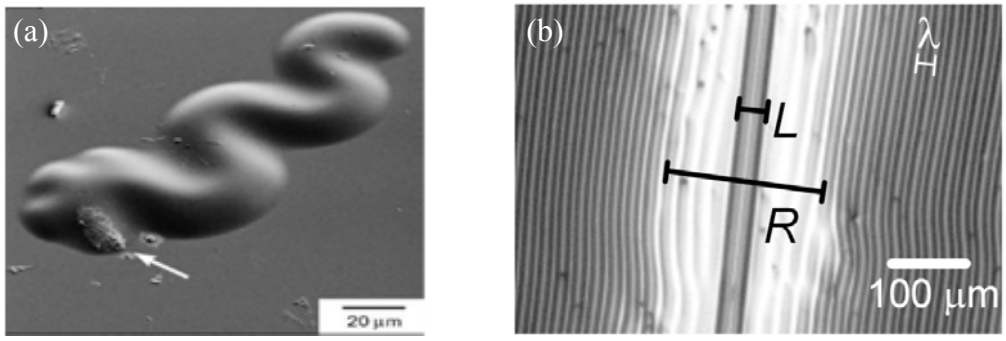

Figure 1.3: (a) A telephone cord blister due to buckle-delamination of a DLC film on a glass substrate [17]; (b) An optical micrograph of a PS film on PDMS, with both surface wrinkling and buckle-delamination [21].

Fracture of a brittle thin film under tension results in channel cracks, as shown in Fig. 1.4. The driving force for growth of a channel crack depends on the mechanical constraint of the substrate [24, 25]. As a result, the crack driving force can be lowered by reducing the film thickness. On a compliant substrate, however, the effect of substrate

constraint is weak and the crack driving force can be significantly higher than on a relatively stiff substrate [26, 27]. Furthermore, it has been observed that, in some cases, channel cracks grow along with interfacial delamination [25, 28], as shown in Fig. 1.5. In this case, interfacial delamination reduces the substrate constraint and thus raises the driving force for the growth of channel cracks. The study of channel cracks has also inspired novel applications to generate channels for microfluidics [29, 30] and controlled fabrication of nanostructures [31-36].

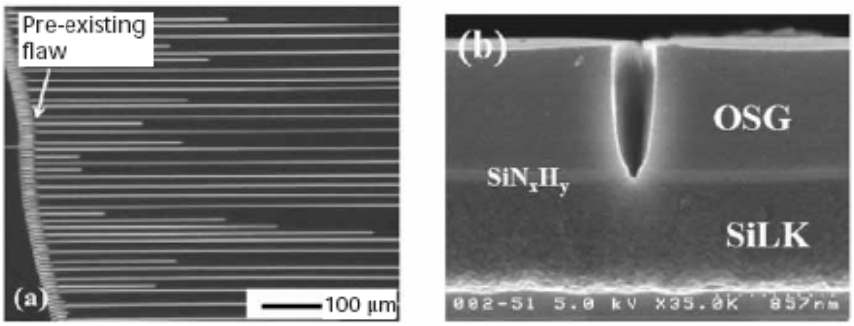

Figure 1.4: (a) Top view, (b) cross-sectional view of channel cracks in thin film stacks of low-k materials [37].

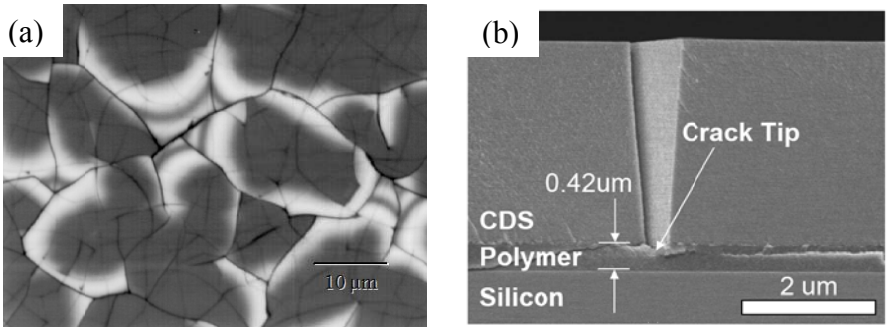

Figure 1.5: (a) Channel cracks of a SiN film on Si (Courtesy of Q. Ma, Intel Corp.); (b) cross-sectional view of interfacial delamination with a channel crack in a thin film of low-k material [25].

Both buckling and cracking of thin films have been studied extensively over the last decades [38, 39]. However, the effects of interfacial properties have not been well understood, especially for thin films on compliant substrates. On one hand, buckling or cracking of thin films may induce growth of interfacial delamination. On the other hand, interfacial delamination may determine the buckling mode and affect the crack driving force. This dissertation presents a systematic study on the mechanical interaction between elastic thin films and elastic compliant substrates through the interfaces based on theoretical modeling and numerical simulations. Both buckling and cracking are considered, with an emphasis on the effects of interfacial delamination.

1.2 Interfacial fracture mechanics

Two approaches are commonly used for the study of interfacial delamination. One is based on linear elastic fracture mechanics (LEFM), and the other is by cohesive zone modeling (CZM). Both approaches are used in the present study. For completeness, a brief summary of the two approaches is presented in this section.

1.2.1 Linear elastic fracture mechanics

Consider a crack along the interface between two isotropic elastic solids as shown in Fig. 1.6. By the LEFM approach, the stress field around the crack tip is analyzed to determine the driving force (i.e., elastic energy release rate) for growth of the interfacial crack, and the criterion for crack growth is established by comparing the energy release rate to the fracture toughness (or adhesion energy) of the interface. Solutions to bimaterial interface crack problems were presented by many since 1950s [40-44], which

have been summarized by Rice [45] and Hutchinson and Suo [39]. Under the plane-strain condition, the singular stress field around the crack tip is represented by using a complex-valued interfacial stress intensity factor, $K = K_1 + \mathrm{i}K_2$, where K_1 and K_2 are the real and imaginary parts, respectively, and they play similar roles to the conventional mode I and mode II stress intensity factors. The normal and shear tractions on the interface directly ahead of the crack tip are of the form

$$\sigma_{22} = \frac{\mathrm{Re}\left[Kr^{i\varepsilon}\right]}{\sqrt{2\pi r}} \quad \text{and} \quad \sigma_{21} = \frac{\mathrm{Im}\left[Kr^{i\varepsilon}\right]}{\sqrt{2\pi r}} \tag{1.1}$$

where r is the distance from the crack tip, and ε is the index of oscillatory singularity depending on the second Dundurs' parameter for the two materials, namely

$$\varepsilon = \frac{1}{2\pi}\ln\left(\frac{1-\beta}{1+\beta}\right) \tag{1.2}$$

Two Dundars' parameters are defined to characterize the mismatch in the elastic properties between the two isotropic elastic materials (e.g., the film and the substrate) [46]:

$$\alpha = \frac{\overline{E}_f - \overline{E}_s}{\overline{E}_f + \overline{E}_s} \quad \text{and} \quad \beta = \frac{\overline{E}_f\left(1-\nu_f\right)\left(1-2\nu_s\right) - \overline{E}_s\left(1-\nu_s\right)\left(1-2\nu_f\right)}{2\left(1-\nu_f\right)\left(1-\nu_s\right)\left(\overline{E}_f + \overline{E}_s\right)} \tag{1.3}$$

where $\overline{E} = E/\left(1-\nu^2\right)$ is the plane strain modulus and ν is Poisson's ratio, with the subscripts f and s for the film and substrate, respectively. Note that $\alpha = \beta = 0$ when the two materials have identical elastic properties. For a stiff film on a relatively compliant substrate, $\alpha > 0$, and it approaches 1 when the substrate is extremely compliant compared to the film. In plane strain problems, β vanishes when both materials are incompressible

($\nu_f = \nu_s = 1/2$) and $\beta = \alpha/4$ when $\nu_f = \nu_s = 1/3$.

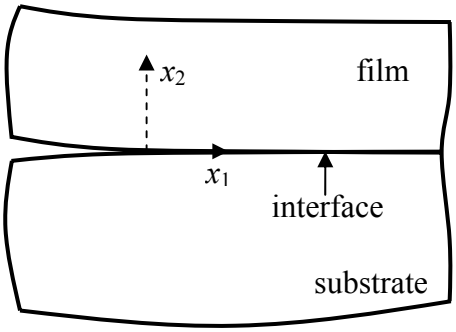

Figure 1.6: A crack lies in the film-substrate interface.

Due to asymmetry in the elastic moduli with respect to the interface, an interfacial crack is typically under the mixed-mode condition. When $\varepsilon = 0$, the interfacial crack-tip stress field reduces to the homogeneous crack-tip field, where K_1 and K_2 are the conventional mode I and mode II stress-intensity factors. In this case, the ratio of the shear traction to the normal traction is simply K_2/K_1, which defines the mode mix. When $\varepsilon \neq 0$, however, the stress field around an interfacial crack tip in general cannot be decoupled into pure mode I (opening) and mode II (shearing) fields. The definition of mode mix as a measure of the proportion of mode II to mode I requires a length quantity since the ratio of the shear traction to the normal traction varies with the distance r. As suggested by Rice [45], an arbitrary length scale (l) may be used to define a phase angle for the interfacial crack, namely,

$$\psi = \tan^{-1}\left[\frac{\mathrm{Im}\left(Kl^{i\varepsilon}\right)}{\mathrm{Re}\left(Kl^{i\varepsilon}\right)}\right] \tag{1.4}$$

The choice of the length l can be based on the specimen geometry, such as the film thickness, or on a material length scale, such as the plastic zone size at the crack tip.

The energy release rate for a crack advancing along an interface is related to the interfacial stress-intensity factors by

$$G = \frac{\left(1-\beta^2\right)\left(K_1^2 + K_2^2\right)}{2}\left(\frac{1}{\bar{\bar{E}}_f} + \frac{1}{\bar{\bar{E}}_s}\right) \tag{1.5}$$

The energy release rate can also be calculated by the J-integral method [41, 47]. The criterion for growth of an interfacial crack is then stated as $G = \Gamma(\psi)$, where Γ is the interface fracture toughness as a function of the phase angle ψ. Based on such a criterion, the interface fracture toughness can be measured experimentally [48-51].

The LEFM approach assumes that a crack pre-exists and the materials are elastic except for the damage zone (or process zone) localized around the crack tip, whose size is much smaller compared to a characteristic size such as the film thickness and the crack length. The microscopic mechanisms of fracture are essentially ignored, and all material aspects are lumped into one parameter, fracture toughness, to qualify the material resistance to fracture.

1.2.2 Cohesive zone models

The LEFM approach cannot predict crack nucleation. Furthermore, when the nonlinear process zone size becomes comparable to or larger than the characteristic size (e.g., the film thickness), the small-scale process zone assumption of LEFM becomes invalid and a nonlinear fracture mechanics approach is required. By using cohesive zone

models, both nucleation and growth of interfacial delamination can be analyzed [52-58].

The first cohesive zone model may be dated back to 1950s by Barrenblatt [59], who modeled the separation process for purely brittle fracture by using an array of nonlinear springs, characterized by a traction-separation curve. In his model, two halves of a body were joined by an array of nonlinear springs, and the boundary-value problem was solved by combining the nonlinear springs with the linear elastic body. An early example of nonlinear fracture mechanics with large-scale bridging was introduced by Dugdale [60], who observed that the plastic zone ahead of a crack tip in a thin sheet of mild steel was primarily a narrow strip of height comparable to the sheet thickness (localized plastic deformation, or necking), while the length of the strip was much longer. The elastic-plastic fracture problem was then modeled by an elastic plane-stress problem with a strip of plastic zone ahead of each crack tip. Barenblatt [61] generalized the plastic strip model to a cohesive zone model (CZM) in which the stress in the cohesive zone ahead of the crack is a function of the displacement rather than a constant yield stress. Cottrell [62] put forward the concept of crack bridging as a unifying theory for fracture at various length scales, from atomic bond breaking in monolithic ceramics to fiber pull-out in composite materials. In each case, the microscopic mechanisms of fracture and associated inelastic processes are represented by a bridging law that relates the face tractions in the bridging zone (or cohesive zone) to the relative displacements, as illustrated in Fig. 1.7. The essential features of crack bridging were reviewed by Bao and Suo [63], emphasizing their implications for strength and fracture resistance of ceramic matrix composites. The concept has also been widely used for modeling interfaces

between elastic-plastic materials [64].

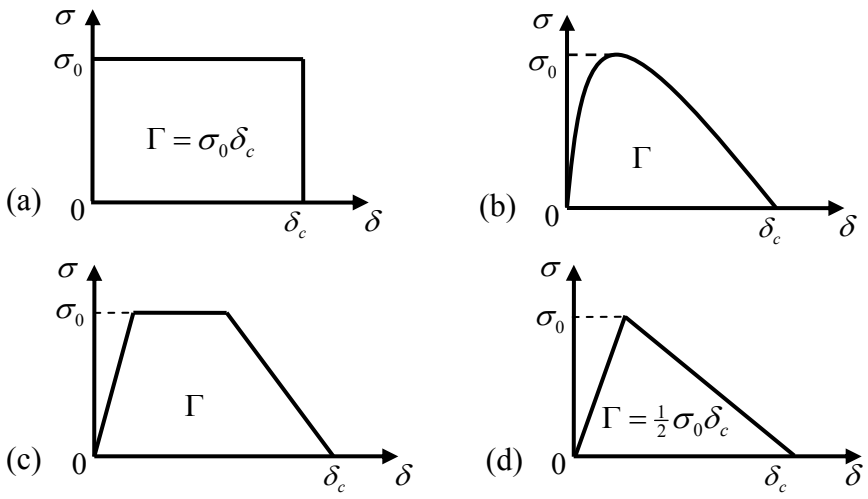

Figure 1.7: A few examples for the traction-separation relationship as the bridging law for the cohesive zone modeling: (a) constant traction for perfect plasticity [60]; (b) smooth nonlinear [65]; (c) trapezoidal [66]; (4) bilinear or triangular [54].

Unlike LEFM where no microscopic details in the damage zone are mentioned, the bridging law or the traction-separation relation in the cohesive zone model depends on the material and the associated fracture mechanism. For example, in an ideally brittle material, fracture occurs by atomic bond breaking, for which a bridging law may be derived from an interatomic bond potential. For metals, however, the fracture mechanism is different, with large plastic deformation (local necking) and void nucleation, growth, and coalescence ahead of the crack tip. The bridging law, $\sigma(\delta)$, may be derived from detailed micromechanics models or may be determined experimentally [65, 66]. On the other hand, relatively simple bridging laws are often used in theoretical and numerical analyses. For example, the Dugdale model assumes a constant traction in the bridging

zone [60]. A triangular or trapezoidal shaped traction-displacement curve is frequently used in practice [54, 57, 66]. In any case, the maximum stress σ_0 and the critical displacement δ_c (or fracture toughness Γ) are the two most important parameters. Given a traction-separation law, the fracture toughness (energy per unit area) is then

$$\Gamma = \int_0^{\delta_c} \sigma(\delta) d\delta \sim \sigma_0 \delta_c \tag{1.6}$$

For brittle fracture, an order-of-magnitude estimate gives that $\Gamma \sim 1$ J/m^2, which is essentially the surface energy per unit area of the solid. For ductile fracture of metals, σ_0 corresponds to the yield stress (~10^8 N/m^2) and δ_c is typically in the order of 10^{-6} m (depending on the microstructures), which lead to a fracture energy much higher than the surface energy, $\Gamma \sim 10^2$ J/m^2.

Cohesive zone modeling is particularly suitable for adhesion and debonding of interfaces between two dissimilar materials [64], where the constituent materials can be either linear elastic or elastic-plastic. Depending on the material systems, the maximum stress of the interfacial bridging law σ_0 can be either small or large compared to the yield stresses of the constituent materials. When σ_0 is greater than the yield stress, plastic deformation in the constituent material occurs during interfacial fracture, and the total energy of fracture is greater than the intrinsic fracture energy of the interface ($\Gamma \sim \sigma_0 \delta_c$). Therefore, the effect of plasticity can be analyzed by coupling the bridging law for the interface with continuum elastic-plastic models for the constituent materials [67].

The size of the bridging zone ahead of the crack tip may be estimated under the condition of small-scale bridging (similar to the small-scaling yielding condition for

linear elastic fracture mechanics). Assume that the bridging zone size is small compared to the crack size, $L << a$. In this case, the external load can be represented by the stress intensity factor K or energy release rate G, ignoring the details of the bridging zone. The crack starts to grow when $G = \Gamma_0$, where Γ_0 is the fracture energy for initiation. As the crack front advances, a bridging zone develops (see Fig. 1.8). An application of the J-integral along a contour at the boundary of the bridging zone gives that [63]

$$G = J = G_{tip} + \int_0^{\delta^*} \sigma(\delta) d\delta \tag{1.7}$$

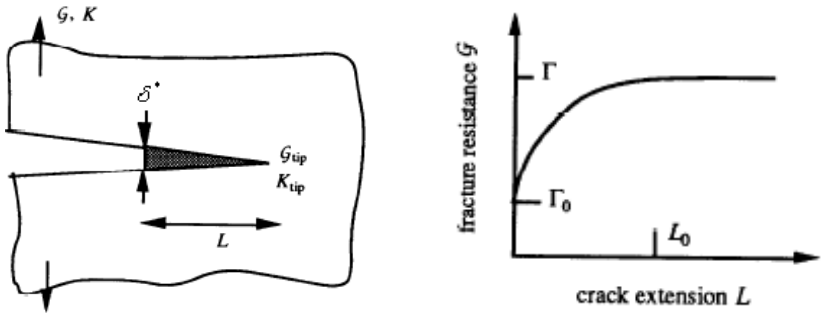

Figure 1.8: A schematic of cohesive zone and *R*-curve (small-scale bridging model [63]).

where δ^* is the opening displacement at the end of the cohesive zone and G_{tip} is the energy release rate at the crack tip. While fracture at the tip of the bridging zone occurs with $G_{tip} = \Gamma_0$, the energy dissipation in the bridging zone requires a larger energy release rate $G > \Gamma_0$, as the size of the cohesive zone increases. The size of the bridging zone L increases as the applied load increases, until a steady state is reached when the separation at the end of the cohesive zone reaches the critical value, $\delta^* = \delta_c$. Subsequently, the

cohesive zone size remains a constant, $L = L_{ss}$, as the crack grows. The required energy release rate for the steady state crack growth is thus:

$$G_{ss} = \Gamma_0 + \int_0^{\delta_c} \sigma(\delta) d\delta \tag{1.8}$$

The so-called resistance curve (*R*-curve) is obtained by plotting the energy release rate as a function of the crack extension, in which G increases from Γ_0 to G_{ss} (Fig. 1.8). To determine the *R*-curve and the steady-state cohesive zone size, a boundary value problem has to be solved. Within the cohesive zone, the face traction is related to the opening displacement by the traction-separation relation. The outer boundary condition is given by the K field corresponding to the applied energy release rate G, under the condition of small-scale bridging. A dimensional analysis [63] leads to scaling law for the steady-state cohesive zone size:

$$L_{ss} \sim \frac{EG_{ss}}{\sigma_0^2} \tag{1.9}$$

However, the small-scale bridging condition is rarely satisfied in practice for composites and interfaces. When large-scale bridging occurs, the *R*-curve depends sensitively on the specimen geometry and thus cannot be used to predict the strength and load carrying capacity of components of different sizes and geometry. A full-scale stress analysis coupling the specimen geometry and the bridging law must be carried out to predict the mechanical properties including the resistance to fracture [63]. In the case of interfacial fracture, the traction-separation relation must be experimentally characterized and then incorporated in the stress analysis as part of the material properties to analyze the interfacial reliability.

1.3 Implementation of cohesive zone model in ABAQUS

The cohesive zone model has been implemented in the commercial finite element package, ABAQUS [68]. In particular, cohesive elements are defined along the potential paths of crack growth (e.g., a bimaterial interface). The constitutive properties of the cohesive elements are specified in terms of the traction-separation relation. Several types of traction-separation relations have been implemented, and self-developed user subroutines may be developed for the cohesive elements with non-standard traction-separation relations. As mentioned, many previous studies [53, 57, 69] have shown that cohesive strength and fracture toughness are the two most important parameters, and the shape of the traction-separation relation is secondary and often ignored. For the present study, the bilinear traction-separation relation as implemented in ABAQUS is adopted in all models with cohesive elements. Similar cohesive zone models have been used in previous works [70-72].

Figure 1.9 illustrates the parameters required to define the interfacial elements: an initial elastic stiffness K_0, a cohesive strength σ_0, and a critical separation δ_c (or interface toughness Γ). Subject to an opening stress σ, the interface first opens elastically with the initial stiffness until the stress reaches the cohesive strength of the interface ($\sigma = \sigma_0$), at which point damage initiation occurs. A damage parameter D is used to describe the state of the interface, which evolves from 0 to 1 based on a damage evolution rule:

$$D = \frac{\delta_c(\delta_{\max} - \delta_0)}{\delta_{\max}(\delta_c - \delta_0)} \tag{1.10}$$

where $\delta_0 = \sigma_0/K_0$ is the critical separation for damage initiation and $\delta_{\max}$ is the maximum

separation for the interface element over the entire loading history. When the interface element is partly damaged ($0 < D < 1$), the opening stress is related to the opening displacement linearly as

$$\sigma = (1-D)K_0\delta \tag{1.11}$$

During loading, $\delta_{max} = \delta$, and the damage parameter D increases as the opening displacement increases. Combining Eqs. (1.10) and (1.11) gives that the stress decreases linearly with the displacement δ ($\delta_0 \le \delta \le \delta_c$):

$$\sigma = \sigma_0 \frac{\delta_c - \delta}{\delta_c - \delta_0} \tag{1.12}$$

When $\delta \ge \delta_c$, $D = 1$ and $\sigma = 0$, indicating that the cohesive element is fully fractured. During unloading, δ_{max} remains as a constant, and so does D. Therefore, the stress decreases linearly as the opening displacement decreases, with the slope $K = (1\text{-}D)K_0$, as illustrated by the dashed line in Fig. 1.9.

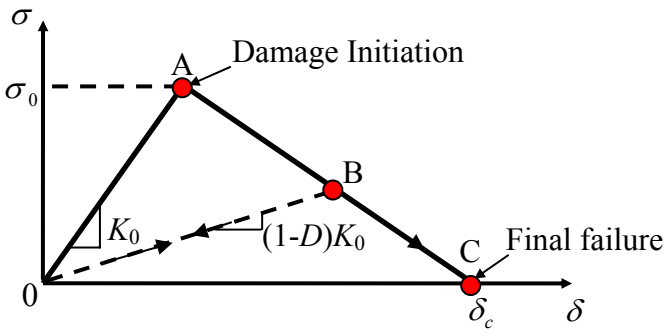

Figure 1.9: Illustration of the bilinear traction-separation law in ABAQUS.

The effect of mode mix for interfacial delamination may be taken into account by defining the traction-separation laws separately for the opening and shearing fracture modes (modes I, II, and III), each with a set of similar parameters as the opening mode. The criteria for mixed-mode damage initiation and final failure must be specified, which may be used to simulate mode-dependent fracture processes. In the present study, the effect of mode mix is ignored in the cohesive zone modeling by taking identical parameters for both opening and shearing modes.

1.4 Scope of this dissertation

In this dissertation, based on the approaches of LEFM and cohesive zone modeling, the common failure mechanisms of elastic thin films on compliant substrates under tensile and compressive film stresses are studied, with a focus on the effects of interfacial delamination. Furthermore, a hybrid approach combining numerical simulations with experimental measurements is developed to determine traction-separation relations for cohesive zone modeling of interfacial delamination. This dissertation is organized as follows.

As an introduction, Chapter 1 gives a brief account of the background and motivation for this work. A summary of the linear elastic fracture mechanics of interfaces and cohesive zone models is presented.

Chapter 2 presents a study on compression-induced buckling of elastic thin films on elastic compliant substrates by analytical and numerical methods. The critical condition for the onset of buckling instability without and with a pre-existing

delamination crack is predicted along with the initial buckling mode. For an elastic film on a highly compliant substrate, nonlinear post-buckling analysis is conducted to simulate concomitant wrinkling and buckle-delamination. By cohesive zone modeling, progressive co-evolution of wrinkling and delamination is simulated.

Chapter 3 considers fracture of brittle thin films on elastic substrates, focusing on the effects of interfacial delamination and substrate penetration. The competition between delamination and penetration is discussed by comparing the effective energy release rates based on LEFM. Cohesive zone models are employed to simulate interfacial delamination and substrate penetration emanating from the root of a channel crack.

In Chapter 4, by combining experimental measurements with cohesive zone modeling, a hybrid approach is developed to determine the traction-separation relation for a bimaterial interface.

In conclusion, Chapter 5 summarizes the results from the present study and remarks on potential directions for future work.

Chapter 2

Buckling of elastic thin films on elastic substrates

Compressing a thin elastic film attached to a thick compliant substrate can lead to buckling instability. Compression-induced buckling and surface wrinkling were first studied as potential failure mechanisms for the stiff skin layers in sandwich panels for aircraft structures [73, 74]. Recent interests in micro/nano-scale thin film materials have exploited the mechanical instability as an enabling mechanism for novel applications [10-13]. Meanwhile, mechanics of surface wrinkling has been studied extensively over the last decade [75-85]. While most of these studies have assumed perfect bonding between the film and the substrate, it has been occasionally pointed out that wrinkling may cause interfacial delamination [75, 86-89]. On the other hand, interfacial delamination is a necessary condition for buckling of thin films attached to relatively stiff substrates [17, 90, 91]. Simultaneous buckling and delamination has also been observed in compressed thin films on compliant substrates [18-20]. More recently, some experiments have shown both surface wrinkling and buckle-delamination co-existing in the same film/substrate system [21].

The characteristics of the two buckling modes are often observable in experiments, with periodic patterns for surface wrinkling (Fig. 2.1a) and localized patterns for buckle-delamination (Fig. 2.1b). One question to be answered is: *what determines the selection of either buckling mode for a given material system?* Furthermore, when the two buckling modes co-exist (Fig. 2.1c), how do they interact with each other in the subsequent growth

of wrinkling and interfacial delamination? In this chapter, by analytical and finite element methods, the critical condition and the post-buckling behavior for elastic thin films on elastic compliant substrates are studied, with an emphasis on the effect of interfacial delamination.

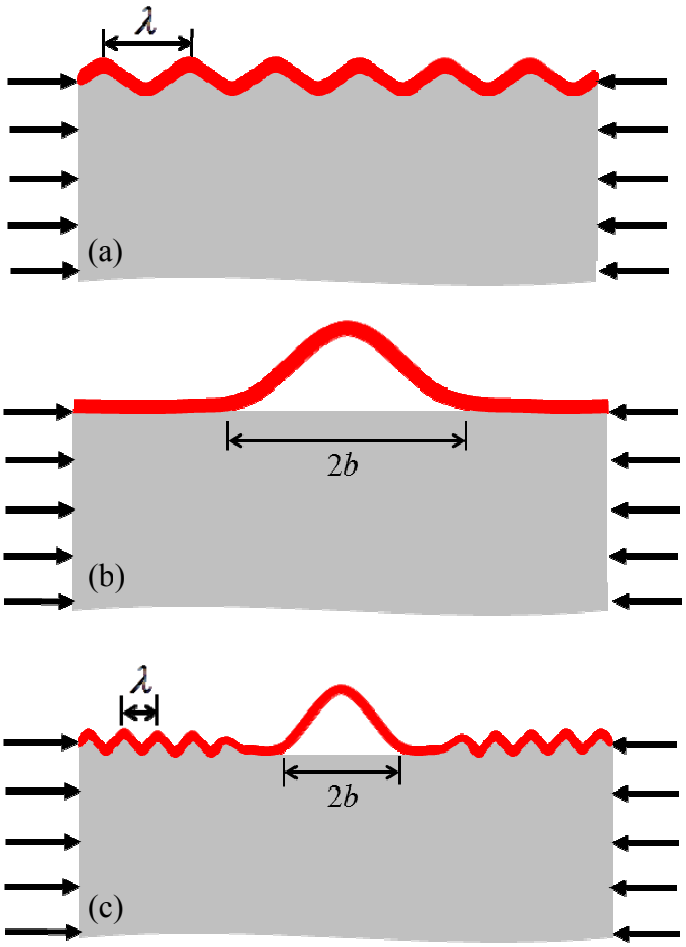

Figure 2.1: Schematic illustration of buckling modes for an elastic thin film on an elastic compliant substrate. (a) Surface wrinkling with no delamination; (b) buckle-delamination; (c) concomitant wrinkling and buckle-delamination.

2.1 Wrinkling, with no delamination

2.1.1 Analytical solution

Consider an elastic thin film on an elastic compliant substrate, subject to lateral compression. Both the film and the substrate are taken to be linear elastic and isotropic, restricted to small, plane-strain deformation for the present study. Let h be the thickness of the film, while the substrate is considered infinitely thick. Let ε be the nominal compressive strain, relative to the stress-free state of the film. When ε is relatively small, the film/substrate bilayer is uniformly compressed and the surface is flat. When the strain exceeds a critical value, the film buckles and the substrate deforms coherently, forming surface wrinkles, as illustrated in Fig. 2.1a. The interface between the film and the substrate is assumed to be perfectly bonded in this section, and the effect of interfacial delamination will be discussed in Section 2.2. A well-known analytical solution predicts the critical strain for onset of wrinkling [78, 92]:

$$\varepsilon_c(kh) = \frac{(kh)^2}{12} + \frac{1}{2kh}\frac{\overline{E}_s}{\overline{E}_f} \tag{2.1}$$

where k is the wave number so that $\lambda = 2\pi/k$ is the wrinkle wavelength, $\overline{E} = E/(1-\nu^2)$ is the plane-strain modulus with E for Young's modulus and ν for Poisson's ratio, and the subscripts f and s denote the film and substrate, respectively. For a given ratio, $\overline{E}_s/\overline{E}_f$, the critical strain in Eq. (2.1) minimizes at a particular wavelength,

$$\lambda^* = 2\pi h\left(\frac{\overline{E}_f}{3\overline{E}_s}\right)^{1/3} \tag{2.2}$$

and the corresponding critical strain is

$$\varepsilon_c^* = \frac{1}{4}\left(\frac{3\overline{E}_s}{\overline{E}_f}\right)^{2/3} \tag{2.3}$$

In deriving the above analytical solution, the shear traction at the film/substrate interface was assumed to be zero. Alternatively, by assuming zero tangential displacement at the interface, a similar analytical solution was obtained [82, 93]. The two solutions are identical if the substrate is incompressible (v_s = 0.5), in which case both the shear traction and tangential displacement are zero. However, when the substrate is compressible (v_s < 0.5), neither the shear traction nor the tangential displacement is zero at the interface as the film wrinkles. As a result, neither analytical solution accurately accounts for the effect of Poisson's ratio of the substrate, which could cause considerable errors in prediction of the critical strain as well as subsequent evolution of wrinkles [85]. Here we present a more accurate analytical solution, taking into account both the shear traction and the tangential displacement at the interface.

The deformation of the thin film is described by the linear plate equations, which are sufficient for linear perturbation analysis here to predict the critical condition for onset of wrinkling. Assume a small perturbation with normal deflection (w) and tangential displacement (u) in the film. The equilibrium condition of the film requires that

$$q = -\frac{\overline{E}_f h^3}{12}\frac{d^4 w}{dx^4} + \varepsilon \overline{E}_f h \frac{d^2 w}{dx^2} \tag{2.4}$$

$$\tau = \overline{E}_f h \frac{d^2 u}{dx^2} \tag{2.5}$$

where q and τ are the normal and shear tractions at the film/substrate interface, respectively.

Both the displacements and the tractions are assumed to be continuous across the interface. Consequently, in addition to Eqs. (2.4) and (2.5), they are related to each other by the equilibrium condition for the substrate. Assume a pair of periodic tractions, $\tau = \tau_m \sin(kx)$ and $q = q_m \cos(kx)$, acting on the surface of an infinitely thick substrate. By solving the equations of linear elasticity under the plane-strain condition [93], the surface displacements of the substrate are obtained as

$$u(x) = \frac{1}{k\overline{E}_s}\left[2\tau_m + \frac{1-2\nu_s}{1-\nu_x} q_m\right]\sin(kx) \tag{2.6}$$

$$w(x) = \frac{1}{k\overline{E}_s}\left[\frac{1-2\nu_s}{1-\nu_s}\tau_m + 2q_m\right]\cos(kx) \tag{2.7}$$

Inserting Eqs. (2.6) and (2.7) into (2.4) and (2.5) results in a linear eigenvalue problem, namely

$$\left(\frac{\overline{E}_s}{\overline{E}_f}\frac{1}{kh} + 2\right)\tau_m + \frac{1-2\nu_s}{1-\nu_s} q_m = 0 \tag{2.8}$$

$$\frac{1-2\nu_s}{1-2\nu_s}\tau_m + \left[\frac{\overline{E}_s}{\overline{E}_f}\left(\frac{1}{12}(kh)^3 + \varepsilon kh\right)^{-1} + 2\right] q_m = 0 \tag{2.9}$$

By setting the determinant of the coefficient matrix in Eqs. (2.8) and (2.9) to zero, we obtain the critical strain for wrinkling as a function of kh,

$$\varepsilon_c(kh) = \frac{(kh)^2}{12} + \frac{1}{2kh}\left(\frac{\overline{E}_s}{\overline{E}_f}\right)\left[1 - \frac{1}{2}\left(\frac{1-2\nu_s}{1-\nu_s}\right)^2\left(\frac{\overline{E}_s}{\overline{E}_f}\frac{1}{kh} + 2\right)^{-1}\right]^{-1} \tag{2.10}$$

For a very compliant substrate, assuming $\overline{E}_s/\overline{E}_f << 2kh$, the critical strain in Eq. (2.10) is approximately

$$\varepsilon_c(kh) \approx \frac{(kh)^2}{12} + \frac{1}{2kh}\left(\frac{\overline{E}_s}{\overline{E}_f}\right)\left[1 - \frac{1}{4}\left(\frac{1-2\nu_s}{1-\nu_s}\right)^2\right]^{-1} \tag{2.11}$$

Both Eqs. (2.10) and (2.11) reduce to (2.1) when $\nu_s = 0.5$.

The critical strain in Eq. (2.11) is minimized at a particular wavelength

$$\lambda^{**} = 2\pi h\left(\frac{\overline{E}_f}{3\overline{E}_s}\right)^{1/3}\left[1 - \frac{1}{4}\left(\frac{1-2\nu_s}{1-\nu_s}\right)^2\right]^{1/3} \tag{2.12}$$

and the corresponding minimum critical strain is

$$\varepsilon_c^{**} = \frac{1}{4}\left(\frac{3\overline{E}_s}{\overline{E}_f}\right)^{2/3}\left[1 - \frac{1}{4}\left(\frac{1-2\nu_s}{1-\nu_s}\right)^2\right]^{2/3} \tag{2.13}$$

Figure 2.2 shows the effect of Poisson's ratio (ν_s) on the critical strain and the wrinkle wavelength, comparing the analytical solutions in Eqs. (2.12) and (2.13) with those in Eqs. (2.2) and (2.3). As ν_s increases, the ratio between the two critical strains, $\varepsilon_c^{**}/\varepsilon_c^{*}$, decreases, while the ratio between the two wrinkle wavelengths, λ^{**}/λ^{*}, increases. For an incompressible substrate ($\nu_s = 0.5$), both ratios are identically one. For a compressible substrate ($\nu_s < 0.5$), however, Eq. (2.3) underestimates the critical strain and Eq. (2.2) overestimates the wrinkle wavelength. The difference can be significant, up to about 20% for the critical strain and nearly 10% for the wavelength.

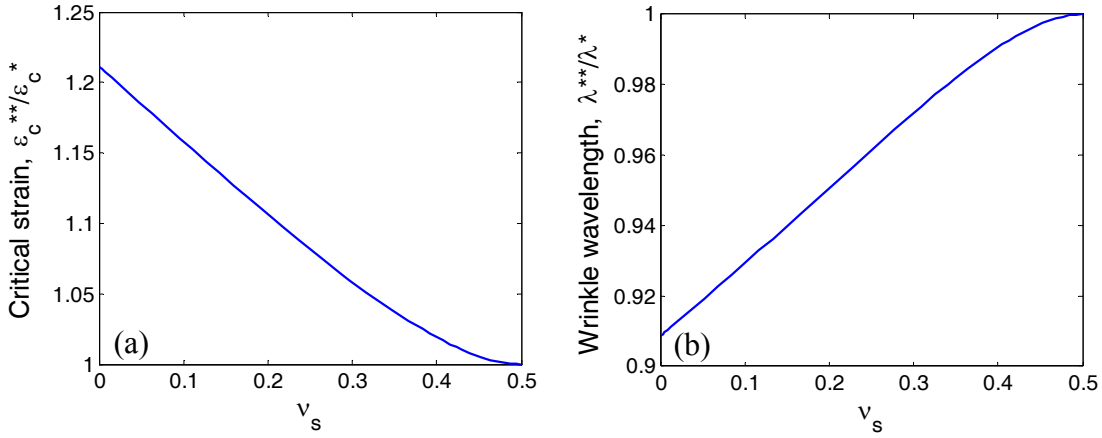

Figure 2.2: Effects of the substrate Poisson's ratio on wrinkling: (a) critical strain for onset of wrinkling; (b) wrinkle wavelength.

Beyond the critical strain, the wrinkle amplitude grows as a function of the nominal strain ε. An approximate solution for the wrinkle amplitude was obtained previously by a nonlinear approach that minimizes the strain energy in the film and the substrate [92, 93]. For an arbitrary wavelength (λ), the equilibrium wrinkle amplitude is

$$A_W(\lambda) = \frac{\lambda}{\pi}\sqrt{\varepsilon - \varepsilon_c} \tag{2.14}$$

When the wavelength $\lambda = \lambda^*$, the equilibrium amplitude becomes

$$A_W^* = h\sqrt{\frac{\varepsilon}{\varepsilon_c^*} - 1} \tag{2.15}$$

Apparently, using an underestimated critical strain would result in an overestimate of the wrinkle amplitude by Eq. (2.14) or (2.15). Thus, the prediction of wrinkle amplitude should also take into account the effect of substrate Poisson's ratio, which however is beyond the analytical approach.

2.1.2 Finite element analysis of wrinkling

Next we present results from finite element analysis (FEA) of wrinkling, in comparison with the analytical solution. As illustrated in Fig. 2.3, a two-dimensional (2D) plane-strain model is constructed using the commercial FEA package, ABAQUS. Besides the film thickness h, the thickness of the substrate is H and the length is L in the FEA model. The effects of H and L on the results will be discussed. The film/substrate bilayer is subject to compression by a prescribed horizontal displacement ($\hat{u}$) along the right side, while the horizontal displacement is zero along the left side. The nominal compressive strain is thus, $\varepsilon = \hat{u}/L$. The shear traction is zero on both sides. The lower surface of the substrate is subject to zero normal displacement and zero shear traction, while the upper surface of the film is traction free. Both the film and the substrate are modeled by 2D quadrilateral elements (CPE8R). A uniform mesh is used for the film with at least 4 elements across the film thickness. The mesh size for the substrate is graded in the thickness direction, finer near the interface. The mesh independence of the numerical results is constantly checked and confirmed. An alternative finite element method is described in Appendix A, in which the substrate is treated analytically as a semi-infinite half plane and the film is modeled by using one-dimensional (1D) elements. The results from both methods will be compared. For most numerical results in this chapter, we set the linear elastic material properties for the film and the substrate with E_f/E_s=1000 and $\nu_f = \nu_s$ =1/3. The high modulus ratio represents a typical material system with a stiff skin layer on a soft substrate [87].

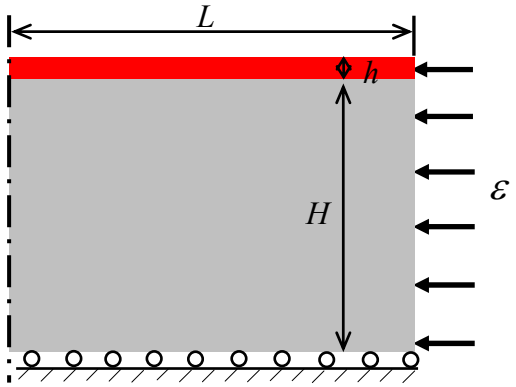

Figure 2.3: Schematic illustration of the finite element model for wrinkling.

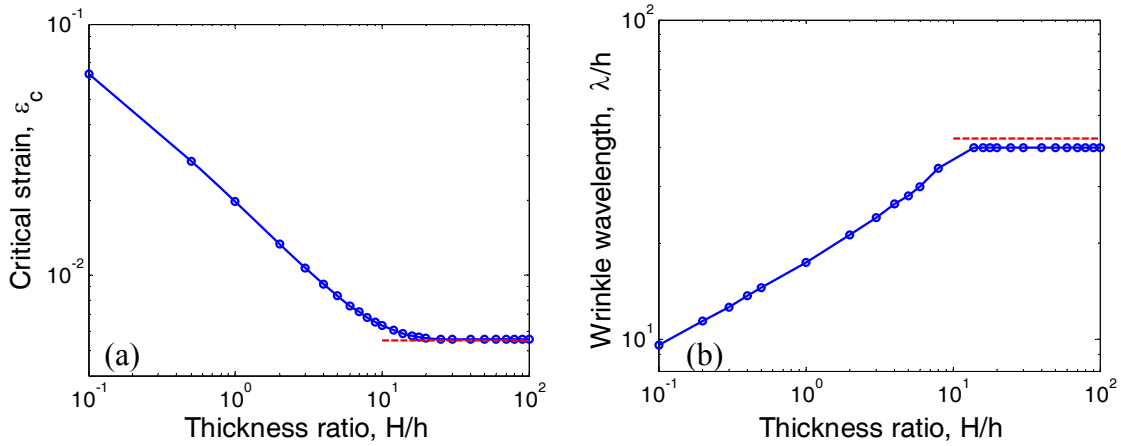

Figure 2.4: Effect of substrate thickness on the finite element analysis of wrinkling: (a) critical strain; (b) wrinkle wavelength. The material properties are E_f/E_s = 1000, and v_f = v_s =1/3. The horizontal dashed lines indicate the analytical solutions for an infinitely thick substrate.

A linear eigenvalue analysis is performed with the finite element model to predict the critical strain for onset of wrinkling and the corresponding eigen mode. To compare with the analytical solution for an infinitely thick substrate, we examine the effect of the substrate thickness (H) in the finite element model and use a sufficiently large thickness

for the subsequent analysis. Figure 2.4a shows the critical strain as a function of H by the finite-element eigenvalue analysis, and Fig. 2.4b shows the corresponding wrinkle wavelength of the eigen mode. Both the critical strain and the wrinkle wavelength become independent of the substrate thickness for $H > 20h$, while the wrinkle wavelength is about $40h$. To simulate an infinitely thick substrate, we set $H = 100h$ in the 2D finite element model unless noted otherwise.

Figure 2.5 compares the FEA results with the analytical solution in Eq. (2.11) for different values of Poisson's ratio (v_s). Each eigenvalue analysis predicts a set of eigenvalues and eigen modes, based on which the critical strain for each eigen mode of a particular wavelength is obtained. To satisfy the prescribed boundary conditions, the wavelengths of permissible eigen modes take discrete values such that $L/\lambda = n/2$ (n = 1, 2, …). For a finite length L, e.g., $L = 120h$ in the present model, the critical strain is obtained as discrete points in Fig. 2.5. On the other hand, the analytical solution for the critical strain in Eq. (2.11) is plotted as continuous solid lines. The numerical results agree closely with the analytical solution, showing an appreciable dependence on Poisson's ratio. In particular, for $v_s = v_f = 1/3$, the minimum critical strain predicted by the analytical solution in Eq. (2.13) is $\varepsilon_c^{**} = 0.00543$ and the corresponding wrinkle wavelength is $\lambda^{**} = 42.6h$. With a discrete set of eigen modes for the finite element model, the wavelength of the first eigen mode is $\lambda = 40h$, with the critical strain $\varepsilon_c = 0.00556$. Due to the slightly different wavelength, the minimum critical strain obtained by FEA is slightly higher than the analytical solution. The agreement can be improved by using a larger value of L or by choosing L to be a multiple of the predicted wrinkle wavelength

(λ^{**}). The results from the 2D and 1D finite element methods are practically indistinguishable for the eigenvalue analysis.

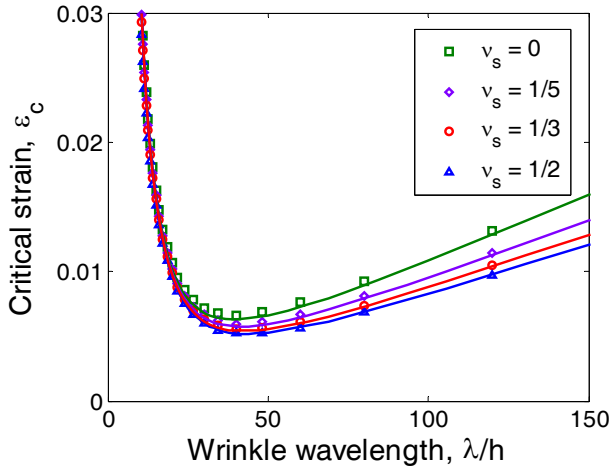

Figure 2.5: Critical strain for wrinkling from the finite element eigenvalue analysis, in comparison with the analytical solution in Eq. (2.11), with $E_f/E_s = 1000$, and $\nu_f = \nu_s = 1/3$.

To simulate wrinkle growth beyond the critical strain, a nonlinear post-buckling analysis is performed with the 2D finite element model. The first eigen mode obtained from the linear analysis is used as the initial geometric imperfection to trigger buckling instability. Figure 2.6 shows the wrinkle amplitude as a function of the nominal strain. For comparison, the approximate analytical solution in Eq. (2.14) is plotted as a continuous solid line with $\lambda = 40h$ and $\varepsilon_c = 0.00556$ for the first eigen mode. The numerical results vary slightly as the amplitude of the initial imperfection (A_0/h) varies. The onset of wrinkling at the critical strain becomes less abrupt if the amplitude of the initial imperfection is relatively large. Using a small initial imperfection ($A_0/h = 10^{-4}$), the

numerical results compare closely with the analytical solution, with an abrupt transition at the critical strain. In the 1D finite element model, instead of the geometric imperfection, a displacement perturbation is introduced for the post-buckling analysis, and the wrinkle amplitude is found to be in excellent agreement with the analytical solution with no dependence on the perturbation amplitude. It is thus concluded that the analytical solution in Eq. (2.14) is a good approximation for the wrinkle amplitude as long as the critical strain and the wrinkle wavelength are used accurately. By setting $\lambda = \lambda^{**}$ and $\varepsilon_c = \varepsilon_c^{**}$ in Eq. (2.14), we obtain that

$$A_W^{**} = h\sqrt{\frac{\varepsilon}{\varepsilon_c^{**}} - 1} \tag{2.16}$$

The effect of the substrate Poisson's ratio on the wrinkle amplitude is thus fully accounted for by using the critical strain in Eq. (2.13) instead of Eq. (2.3).

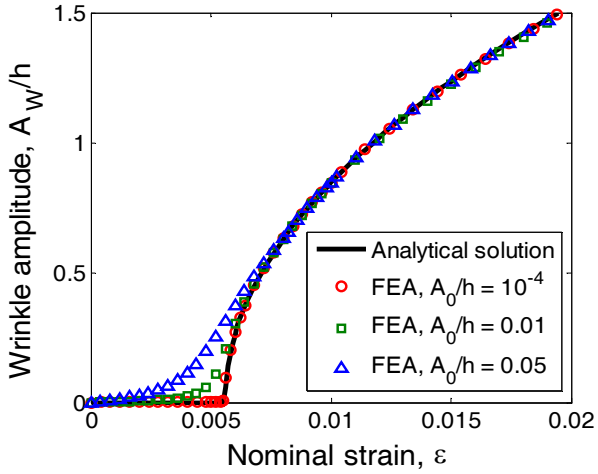

Figure 2.6: Wrinkle amplitude as a function of the nominal strain, comparing the results from post-buckling finite element analysis with the analytical solution in Eq. (2.14) for $E_f/E_s = 1000$, and $\nu_f = \nu_s = 1/3$.

2.1.3 Wrinkle-induced delamination

As the wrinkle amplitude grows, the normal and shear tractions acting on the film/substrate interface increase, which may cause delamination [75, 86, 88]. To estimate the interfacial tractions in the nonlinear post-buckling regime, we assume zero tangential displacement in Eq. (2.6) so that the maximum shear traction is linearly related to the maximum normal traction, namely

$$\tau_m = -\frac{1-2\nu_s}{2(1-\nu_s)} q_m \tag{2.17}$$

Inserting Eq. (2.17) into (2.7) along with (2.14) for the wrinkle amplitude, we obtain the maximum normal traction as a function of the nominal strain:

$$q_m = \frac{4(1-\nu_s)^2 \overline{E}_s}{3-4\nu_s} \sqrt{\varepsilon - \varepsilon_c} \tag{2.18}$$

Alternatively, the normal traction may be estimated by assuming zero shear traction in Eq. (2.7). By comparing to the FEA results, as shown in Fig. 2.7, it is found that the zero tangential displacement assumption offers a better approximation for estimating the wrinkle-induced tractions at the interface. The maximum normal traction by FEA follows Eq. (2.18) remarkably well. While the formula in Eq. (2.17) underestimates the maximum shear traction, it is clear that the shear traction is not zero at the interface.

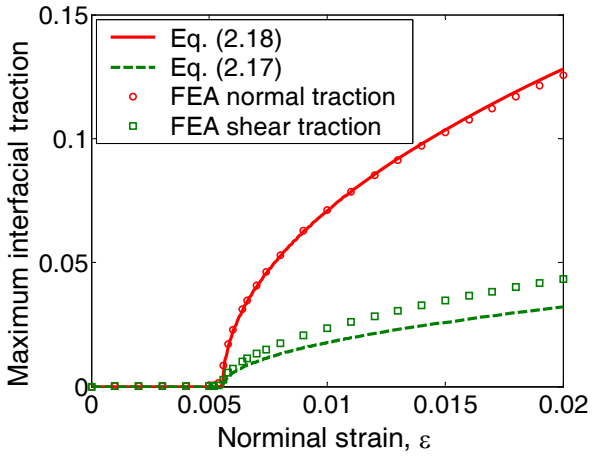

Figure 2.7: The maximum normal and shear tractions at the film/substrate interface, in comparison with the analytical solutions in Eqs. (2.17) and (2.18). The tractions are normalized by the substrate modulus $\overline{E}_s$.

The close agreement for the maximum normal traction in Fig. 2.7 suggests that the formula in Eq. (2.18) may be used as a good approximation to estimate the critical strain for initiation of wrinkle-induced interfacial delamination. As will be shown in Section 2.4 by using a cohesive zone model, the initiation of delamination is predominantly determined by the strength of the interface subject to the normal traction. Similar results have been reported by Goyal et al. [88]. By setting the maximum normal traction in Eq. (2.18) equal the interfacial strength ($\hat{\sigma}_{\text{int}}$), we obtain the critical strain for initiation of wrinkle-induced delamination, namely

$$\varepsilon_{WID} = \varepsilon_c + \left(\frac{3-4\nu_s}{4(1-\nu_s)^2} \frac{\hat{\sigma}_{\text{int}}}{\overline{E}_s} \right)^2 \tag{2.19}$$

where ε_c is the critical strain for wrinkling with no delamination as given in Eq. (2.10) or (2.11), and $\hat{\sigma}_{\text{int}}$ is the peak stress in the normal traction-separation relation for the

interface as described by a cohesive zone model [64]. Beyond the critical strain ε_{WID}, the interfacial delamination grows concomitantly with wrinkling. As a result, the two buckling modes, wrinkling with no delamination and buckle-delamination, may co-exist and interact with each other. Equation (2.19) suggests that for applications that require perfect bonding at the interface, a strength criterion may be used to determine the critical nominal strain for wrinkle-induced interfacial delamination.

2.2 Onset of buckling, with delamination

For a thin film bonded to a relatively stiff substrate, wrinkling is unlikely, due to the effect of substrate constraint that requires a high critical strain for wrinkling without delamination. However, with defects at the film/substrate interface, such as partial delamination of the film, buckling of the film under compression may occur, which in turn drives growth of delamination (Fig. 2.1b), known as buckle-delamination [17, 39, 91]. The co-development of buckling and delamination leads to abundant blister patterns such as telephone-cord blisters. Compared to wrinkling, the buckle-delamination patterns are typically localized and sensitive to interfacial defects [17, 94]. For a compliant substrate, with the presence of interfacial delamination, both wrinkling and buckle-delamination are possible and they may co-exist [21, 87]. In this section, we discuss the effect of pre-existing interfacial delamination on the critical strain for onset of buckling and the initial buckling mode.

2.2.1 Semi-analytical solution

Early studies of buckle-delamination often assumed a fixed-end condition at the

edge of delamination, which essentially neglected the effect of elastic deformation in the substrate [39]. Under such a condition, the critical strain for onset of buckling is identical to that for a freestanding sheet with clamped edges, namely

$$\varepsilon_B = \frac{\pi^2}{12}\left(\frac{h}{b}\right)^2 \tag{2.20}$$

where b is the half-width of the delamination (see Fig. 2.1b).

Recent studies [18, 19, 95] have shown that the critical strain for buckling can be significantly lower than that predicted by Eq. (2.20) when elastic deformation of the substrate is taken into account, especially for relatively compliant substrates. By a semi-analytical approach, Yu and Hutchinson [95] derived an implicit formula for the critical strain of buckling (ε_B^*):

$$\sqrt{\frac{\varepsilon_B}{\varepsilon_B^*}}\tan\left(\pi\sqrt{\frac{\varepsilon_B^*}{\varepsilon_B}}\right) = \frac{\pi h}{12b}\left(\frac{a_{12}^2}{a_{11}+b/h} - a_{22}\right) \tag{2.21}$$

The dimensionless coefficients a_{ij} in Eq. (2.21) depend on the ratio b/h and Dundurs' parameters for elastic mismatch between the film and the substrate as defined in Eq. (1.3). The values of a_{ij} can be determined numerically, either by solving an integral equation [95] or by a finite element method [18]. In the present study, the finite element method is used to calculate a_{ij} as summarized in Appendix B. The critical strain for buckling, ε_B^*, can then be obtained from Eq. (2.21) as a function of b/h and Dundurs' parameters (α and β), namely

$$\varepsilon_B^* = \frac{\pi^2}{12}\left(\frac{h}{b}\right)^2 f\left(\frac{b}{h},\alpha,\beta\right) \tag{2.22}$$

Figure 2.8 shows the critical buckling strain as a function of b/h for two types of elastic mismatch ($\nu_f = \nu_s = 0.5$ and $\nu_f = \nu_s = 1/3$). As noted by Yu and Hutchinson [95], the second Dundurs' parameter, β, typically plays a less important role. Consequently, the results for different β in the two figures are nearly identical. In this study, we focus on the effect of the modulus ratio, $\overline{E}_f / \overline{E}_s$, which is directly related to the first Dundur's parameter α as $\overline{E}_f / \overline{E}_s = (1+\alpha)/(1-\alpha)$. As shown in Fig. 2.8, the critical strain decreases as the ratio $\overline{E}_f / \overline{E}_s$ increases, which can be significantly lower than the prediction by Eq. (2.20).

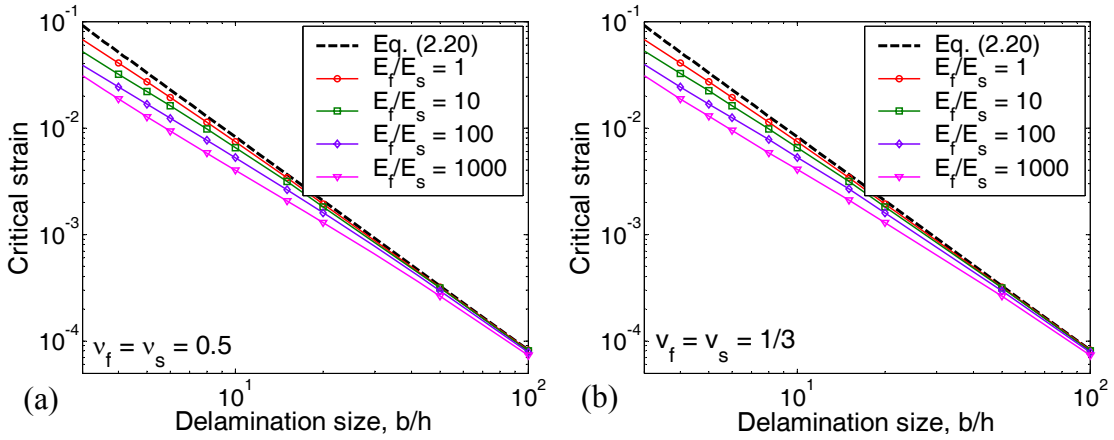

Figure 2.8: The critical buckling strain as a function of delamination size, b/h, as predicted by the semi-analytical solution in Eq. (2.21). (a) $\nu_f = \nu_s = 0.5$ ($\beta = 0$) and (b) $\nu_f = \nu_s = 1/3$ ($\beta = \alpha/4$).

2.2.2 Selection of initial buckling mode

By comparing the critical strain for buckling (with delamination) to the critical

strain for wrinkling (without delamination) in Section 2.1, the favored buckling mode is predicted at the onset of buckling. As shown in Fig. 2.9, both the critical strains decrease as the modulus ratio, $\overline{E}_f/\overline{E}_s$, increases. In the log-log plot, the critical strain for wrinkling (ε_W^*) as given in Eq. (2.13) is a straight line with a slope -2/3. The critical strain for buckling (ε_B^*) in Eq. (2.22) decreases in a much slower rate. In addition, the buckling strain depends on the relative delamination size *b*/*h*, while the wrinkle strain does not. For a constant delamination size, the intersection of the two critical strains defines a critical modulus ratio, R_c. When the modulus ratio is smaller (i.e. $\overline{E}_f/\overline{E}_s < R_c$), the buckling strain is lower than the wrinkling strain, indicating that localized buckle-delamination would occur first as the compressive strain develops in the film. On the other hand, for larger modulus ratios with more compliant substrates ($\overline{E}_f/\overline{E}_s > R_c$), the wrinkling strain is lower and the film would wrinkle everywhere without the need of delamination. Therefore, a transition in the buckling mode is predicted as the modulus ratio between the film and the substrate varies. The critical modulus ratio R_c as a function of the delamination size is determined by setting $\varepsilon_B^* = \varepsilon_W^*$, as plotted in Fig. 2.10. This plot represents a buckling mode selection map: if the film-substrate modulus ratio and the interfacial defect size render a point below the R_c curve, localized buckle-delamination is energetically favored; otherwise, wrinkling is favored. It should be noted that the presented discussion is limited to the onset of the initial buckling mode only.

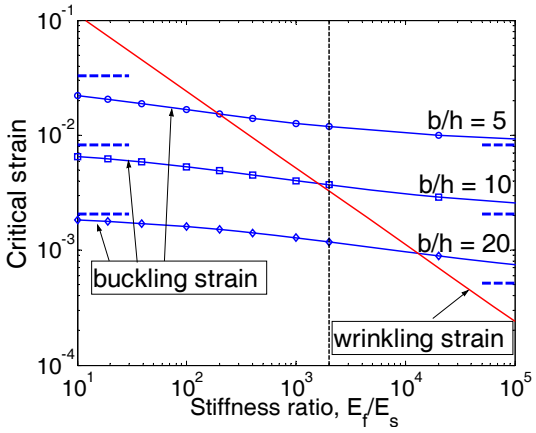

Figure 2.9: Comparison between the critical strain for buckle-delamination and the critical strain for wrinkling. The vertical line represents the PS/PDMS system with $\overline{E}_f / \overline{E}_s = 2000$.

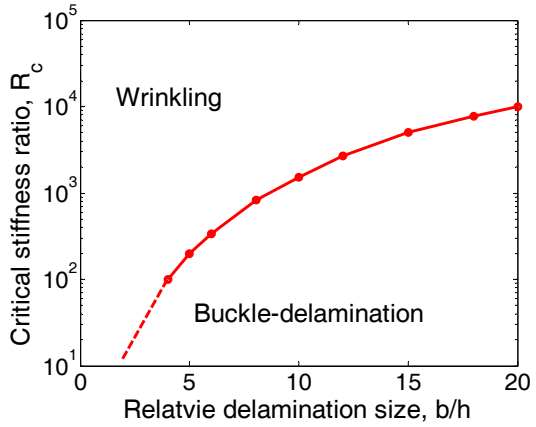

Figure 2.10: The critical modulus ratio as a function of the relative delamination size. Above the line, wrinkling is favored; below the line, buckle-delamination is favored. The dashed portion shows the qualitative trend beyond the limit of the plate theory used in deriving the semi-analytical solution in Eq. (2.21).

The transition of the initial buckling mode as illustrated in Figs. 2.9 and 2.10 is demonstrated qualitatively by an experiment [87]. A polystyrene (PS) film (h = 120 nm) was bonded to a polydimethylsiloxane (PDMS) substrate. The materials' elastic moduli

are estimated as $\overline{E}_f \sim 4$ GPa and $\overline{E}_s \sim 2$ MPa, with a ratio $\overline{E}_f / \overline{E}_s = 2000$ [14]. The Poisson's ratios are taken to be $\nu_f = \nu_s = 0.5$ approximately. From Eq. (2.13), the critical strain for wrinkling is $\varepsilon_W^* \sim 0.00325$, corresponding to a critical compressive stress of 13 MPa. By annealing the specimen at 120°C, which is above the glass transition temperature of PS ($T_g \sim 105$ ºC), and then slowly cooling, a compressive stress develops in the PS film due to its different thermal expansion. Assuming an initially small defect at the interface (e.g., $b/h = 5$), as illustrated by the vertical line in Fig. 2.9, the thermally induced compressive stress in the PS film first reaches the wrinkling strain, at which point wrinkling occurs spontaneously over the film surface. As the temperature is further decreased, the stress eventually reaches the critical buckling strain for the initial defect size, and buckle-delamination occurs alongside with the existing wrinkles. Figure 2.11 shows a set of optical images of the PS film on the PDMS substrate, which demonstrates the occurrence of wrinkling followed by buckle-delamination during the first cooling cycle (top row). The inset Fourier spectrum shows a well-defined wrinkle wavelength at 60 °C. When the material system is heated back to 120°C, the compressive stress in the film is relaxed and the elastic film recovers with no observable buckling or wrinkling. Next, the system is subjected to a second cooling (Fig. 2.11, second row). Compared to the first cooling, the interfacial defect size has increased due to the growth of buckle-delamination in the first cycle. An estimate of the delamination width (Fig. 2.11, top row, 35°C) gives that $b/h \sim 20$ for the second cycle, for which the buckling strain is lower than the wrinkling strain with $\overline{E}_f / \overline{E}_s = 2000$ as shown in Fig. 2.9. Consequently, localized

buckle-delamination occurs first, at locations similar to those observed in the first cycle. Further cooling leads to growth of buckle-delamination and eventually wrinkling of the bonded region as well. Slightly different buckling and wrinkling patterns are observed at the end of the first and second cycles, which can be attributed to the different evolution paths for mode transition and interactions.

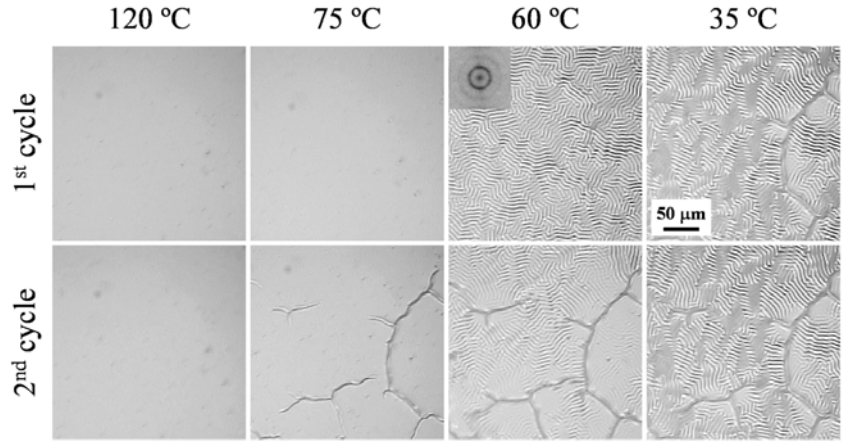

Figure 2.11: Optical micrographs of a 120 nm PS thin film on a PDMS substrate cooled from 120 °C to 35 °C, where wrinkling is the favored buckling mode during the 1st cooling cycle (top row) and buckle-delamination is favored in the 2nd cycle. The Fourier spectrum at 60 °C (inset) in the first cycle shows a well-defined wrinkle wavelength.

It is noted that, for each delamination size, the buckling strain (ε_B^*) as determined from Eq. (2.21) has two limits: for low film/substrate modulus ratios, the buckling strain approaches ε_B as given by Eq. (2.20), which sets the upper limit; for very high modulus ratios, the buckling strain approaches $\varepsilon_B/4$ as the lower limit. These limiting strains are plotted as horizontal dashed lines in Fig. 2.9. While the upper limit corresponds to the buckling of the delaminated film with fixed ends as an approximation for a rigid substrate,

the lower limit is identical to that for buckling of a free-standing film of length 2*b* simply supported at both ends. Therefore, as the substrate stiffness decreases, the effective constraint at the edges of delamination relaxes from essentially fixed ends (constraint on both displacement and rotation) to simply supports (no constraint on rotation). This is reasonable if one consider buckling of the delaminated region only. However, as discussed above, when $\overline{E}_f/\overline{E}_s > R_c$, buckling is no longer limited to the delaminated region. Consequently, the semi-analytical solution in Eq. (2.21) should be valid only for the regime $\overline{E}_f/\overline{E}_s < R_c$. Another limit for the semi-analytical solution is set by the use of the plate equations for the delaminated part, which requires the ratio *b*/*h* to be relatively large (e.g., $b/h > 5$).

2.2.3 Finite element eigenvalue analysis

To overcome the limitations of the semi-analytical solution, an eigenvalue buckling analysis is performed to predict the critical strain for onset of buckling, by introducing an interfacial crack in the 2D finite element model, as illustrated in Fig. 2.12. By symmetry, only half of the delamination crack is modeled, with a relatively fine mesh near the crack tip. The boundary conditions are same as those used for the finite element analysis of wrinkling (Fig. 2.3). Here, since the film is modeled by 2D solid elements, relatively short interfacial crack can be considered. Moreover, the buckling mode is not prescribed in the finite-element eigenvalue analysis, which searches for all possible eigen modes that satisfy the boundary conditions. The eigenvalue for the first eigen mode gives the critical strain for onset of buckling instability.

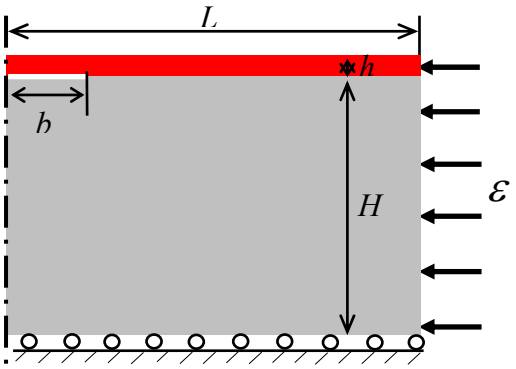

Figure 2.12: Schematic illustration of the finite element model for buckle-delamination.

For a thin film system with E_f/E_s =1000 and $\nu_f = \nu_s$ =1/3, the critical strain for buckling as a function of b/h is determined by the finite-element eigenvalue analysis, as plotted in Fig. 2.13a. For comparison, the analytical solution predicted by Eq. (2.20) and the semi-analytical solution by Eq. (2.21) are also shown in the figure. For $b/h > 20$, the FEA results agree closely with the prediction by Eq. (2.21). For a shorter crack, however, the FEA result deviates from the semi-analytical solution. As b/h decreases, the FEA-predicted critical strain approaches a plateau that corresponds to the critical strain for wrinkling with no delamination, shown as the horizontal dot-dashed line. The corresponding eigen modes shown in Fig. 2.14 reveal a transition from the localized mode of buckle-delamination to the periodic wrinkling mode. When b/h is relatively large, buckling occurs predominantly at the location of delamination. When b/h is small, buckling is not restricted to the delaminated part and periodic wrinkles form. The smooth transition of the critical strain in Fig. 2.13a suggests that a mixed mode of buckling occurs with an intermediate delamination length ($3 < b/h < 20$), for which the analytical

solutions for both buckle-delamination and wrinkling overestimate the critical strain. The results from the 1D finite element model (Appendix A) are in close agreement with the 2D FEA results. Figure 2.13a also shows that the analytical solutions in Eqs. (2.20) and (2.21) converge for increasingly large b/h. However, for a typical delamination size, the discrepancy is significant (e.g., 0.00405 vs 0.0082 for b/h = 10).

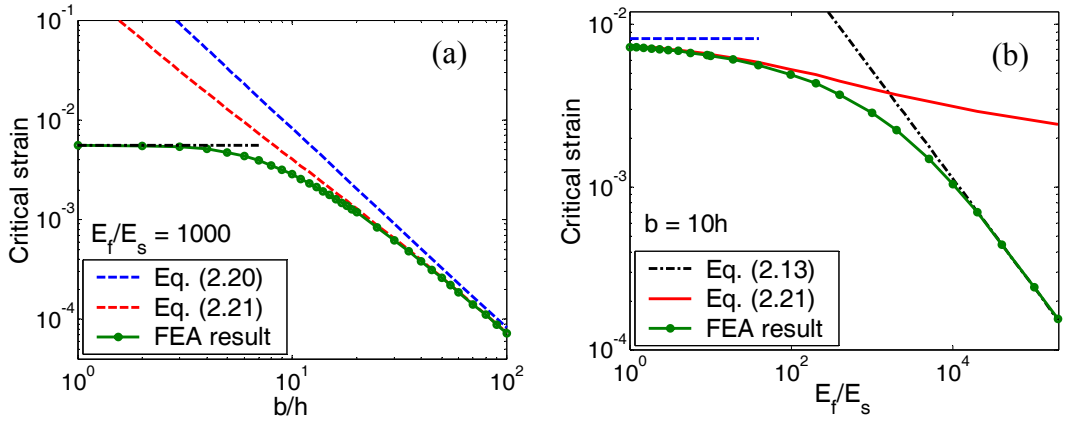

Figure 2.13: (a) Comparison of the critical strain for buckling between analytical solutions and the finite element eigenvalue analysis. The horizontal dot-dashed line represents the critical strain for wrinkling with no delamination. (b) The critical strain for buckling as a function of the modulus ratio for b/h = 10. The horizontal dashed line represents the analytical solution in Eq. (2.20).

The elastic mismatch between the film and the substrate plays an important role in the transition of the initial buckling mode. For a fixed delamination size (e.g., b/h = 10), the critical strain is obtained as a function of the ratio, E_f/E_s, shown in Fig. 2.13b. The FEA results are plotted along with the two analytical solutions. Again, a smooth transition is predicted. For a very compliant substrate ($E_f/E_s > 10^4$), the FEA-predicted critical strain compares closely with the analytical solution in Eq. (2.13) for wrinkling with no

delamination. For a stiff substrate ($E_f/E_s < 100$), the critical strain approaches the semi-analytical solution as predicted by Eq. (2.21) for buckle-delamination. When the substrate is very stiff ($E_f/E_s < 1$), both the FEA results and the semi-analytical solution approach the analytical solution in Eq. (2.20), which is independent of the modulus ratio. For an intermediate modulus ratio ($100 < E_f/E_s < 10^4$), the film buckles in the mixed mode with the critical strain lower than the analytical solutions for both wrinkling and buckle-delamination.

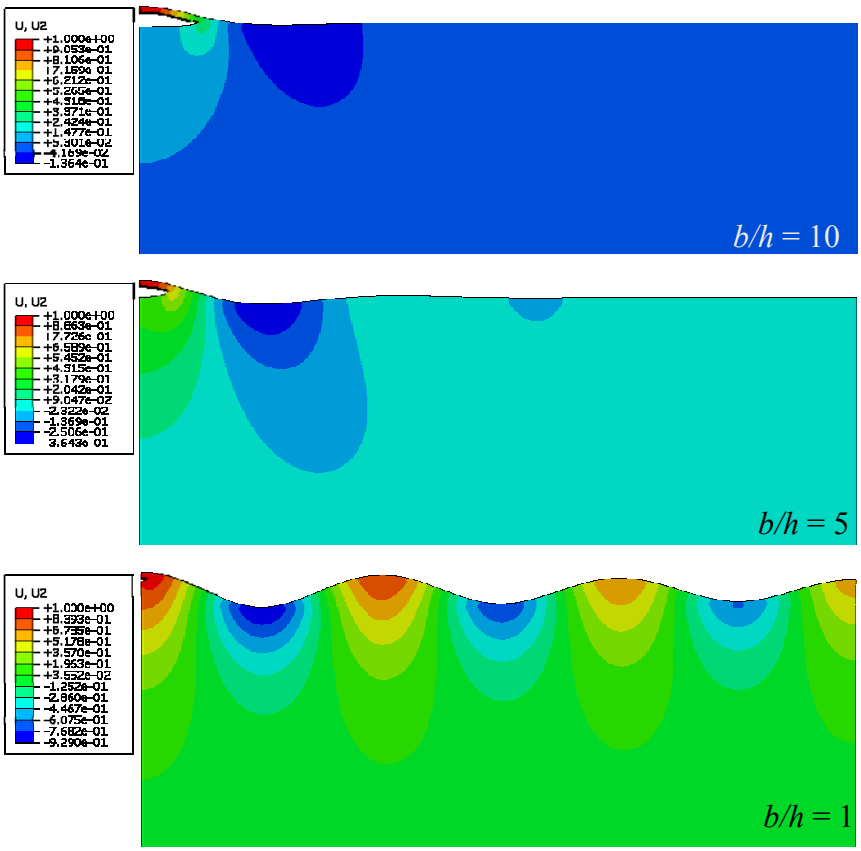

Figure 2.14: Eigen modes of an elastic thin film on an elastic compliant substrate with pre-existing interfacial delamination of different sizes (b/h = 10, 5, and 1).

Based on the finite-element eigenvalue analysis, a diagram for the initial buckling modes may be constructed in the plane with the ratio E_f/E_s and b/h as the coordinates, as schematically shown in Fig. 2.15. In addition to the two primary modes (buckle-delamination and wrinkling) as shown in Fig. 2.10, there exists a mixed mode in between, which facilitates the smooth transition of the primary buckling modes. As shown in Fig. 2.13, the critical strain for the onset of buckling in the mixed mode cannot be predicted accurately by either the analytical solution for wrinkling or the semi-analytical solution for buckle-delamination.

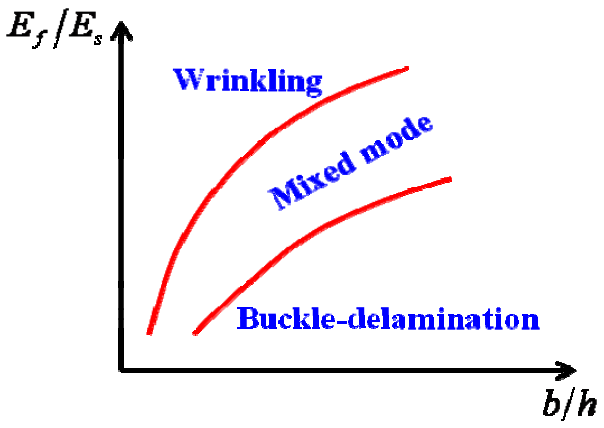

Figure 2.15: A schematic diagram for the buckling modes.

2.3 Post-buckling analysis with delamination

Beyond the critical strain, the buckle amplitude increases with the nominal strain, and the delamination crack may grow. For an elastic film on a rigid substrate, the buckle amplitude is obtained analytically [39] as

$$A_B = \frac{2h}{\sqrt{3}}\sqrt{\frac{\varepsilon}{\varepsilon_B} - 1} \tag{2.23}$$

where ε_B is the critical strain for onset of buckling as given in Eq. (2.20). The energy release rate driving growth of the interfacial delamination is

$$G = G_0\left(1 - \frac{\varepsilon_B}{\varepsilon}\right)\left(1 + \frac{3\varepsilon_B}{\varepsilon}\right) \tag{2.24}$$

where $G_0 = \overline{E}_f h\varepsilon^2/2$. The delamination grows when the energy release rate exceeds the interfacial toughness and arrests when it drops below the toughness.

For an elastic compliant substrate, both the buckle amplitude and the energy release rate can be significantly greater than the predictions by the rigid-substrate model [18, 19, 95]. Following Yu and Hutchinson [95], a semi-analytical approach for the post-buckling analysis is summarized in Appendix B, which takes into account the effects of substrate compliance on the buckle amplitude and energy release rate. However, as discussed in Section 2.2, the semi-analytical approach tends to overestimate the critical strain for onset of buckling, which in turn affects the prediction of post-buckling behavior, especially for relatively short cracks and very compliant substrates. Using the finite element model with delamination (Fig. 2.12), a nonlinear post-buckling analysis is performed to study the evolution of the buckling mode beyond the critical strain. The eigen mode obtained by the linear analysis in Section 2.2 is used as the initial imperfection with a small amplitude ($A_0/h = 10^{-4}$).

Figure 2.16a shows the evolution of the buckling profile as the nominal strain increases. For the numerical results in this section, the linear elastic properties for the

film and the substrate are set with E_f/E_s =1000 and $\nu_f = \nu_s$ =1/3. For b/h = 10, the critical strain predicted by the eigenvalue analysis is 0.00284. The film remains flat when $\varepsilon <$ 0.00284. Beyond the critical strain, the buckling deformation is predominantly localized near the location of delamination, and the film remains flat far away from the delamination. As the film buckles, the substrate surface is pulled up significantly near the edge of delamination, as shown by the dashed lines. The film deforms with both out-of-plane displacement and rotation at the edge of delamination. Beyond the edge, the film first bends down and then up, forming a valley before it becomes nearly flat. Far away from the delamination, the film and the substrate surface moves up slightly due to Poisson's effect. We define the buckle amplitude A_B as the difference between the vertical displacement at the peak and that at the valley. Figure 2.16b plots the buckle amplitude as a function of the nominal strain for b/h = 1, 5, 10, and 20. As b/h increases, the critical strain for onset of buckling decreases, and the buckling amplitude increases. For small b/h, the buckling profile becomes periodic wrinkles, and as expected the buckle amplitude approaches twice the wrinkle amplitude as predicted by the analytical solution in Eq. (2.14). It is noted that the presence of even a short interfacial delamination could raise the apparent wrinkle amplitude beyond the analytical prediction. Therefore, the winkle amplitude is typically not a reliable quantity for the measurement of elastic properties since it depends sensitively on the pre-existing delamination, which is often not well controlled in experiments.

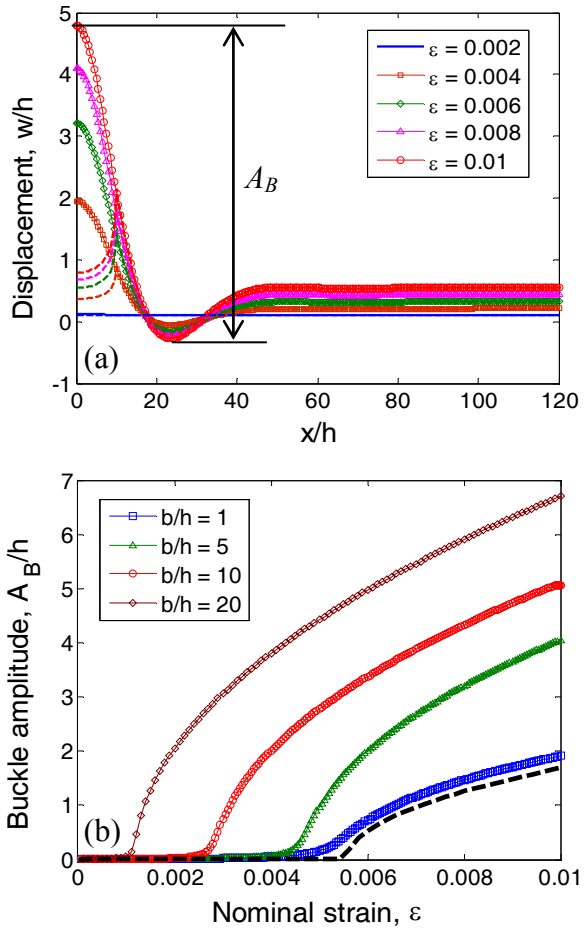

Figure 2.16: (a) Out-of-plane displacements of the film (solid lines) and the substrate surface (dashed lines) by the post-buckling finite element analysis for b/h = 10 and L/h = 120. (b) Buckle amplitude as a function of the nominal strain for different b/h. The dashed line in (b) shows twice of the wrinkle amplitude with no delamination as predicted by the analytical solution in Eq. (2.14).

It is found that the results from the post-buckling analysis strongly depend on the ratio, L/b, in the finite element model. As shown in Fig. 2.17a, the buckle amplitude increases with increasing L/b, while the critical strain for onset of buckling is independent of L/b. Correspondingly, the energy release rate for buckle-driven delamination, calculated by the method of J-integral [47], also increases as L/b increases (Fig. 2.17b).

For comparison, the rigid-substrate solution in Eqs. (2.23) and (2.24) are plotted as the thick dashed lines, and the semi-analytical solutions by Yu-Hutchinson approach are plotted as the thick solid lines. It is expected that the FEA results eventually converge towards the semi-analytical solution for a sufficiently large L/b. Such convergence can be easily achieved for a relatively stiff substrate (e.g., E_f/E_s <100). For a compliant substrate, however, the convergence can be very slow. Figure 2.18 shows the energy release rate, normalized by the semi-analytical solution (G_∞), as a function of L/b for different modulus ratios. For E_f/E_s =100, the calculated energy release rate agrees closely with G_∞ for L/b = 60 and beyond. With E_f/E_s =1000, the convergence is not reached for L/b up to 100. Such a slow convergence may be qualitatively understood as the shear-lag effect. The stress in the film is partly relaxed by buckling at the delamination but unaffected far away from the delamination. In between, the stress in the film varies over a characteristic length scale for load transfer, depending on the stiffness of the substrate as defined in a shear lag model [96]. The length scale is much longer for a compliant substrate than for a stiff substrate. For the finite element model with L smaller or comparable to the shear lag length, due to interaction between buckle-delamination at one end of the film and the boundary conditions at the other end, both the buckle amplitude and the energy release rate depend on L. Alternatively, the results in Fig. 2.17 and Fig.2.18 may be understood as the post-buckling behavior for a periodic array of buckle-delamination with a spacing $2(L-b)$ between the adjacent delamination cracks, for which the effect of spacing is similar to that for a periodic array of channeling cracks in an elastic thin film on a compliant substrate [27, 96].

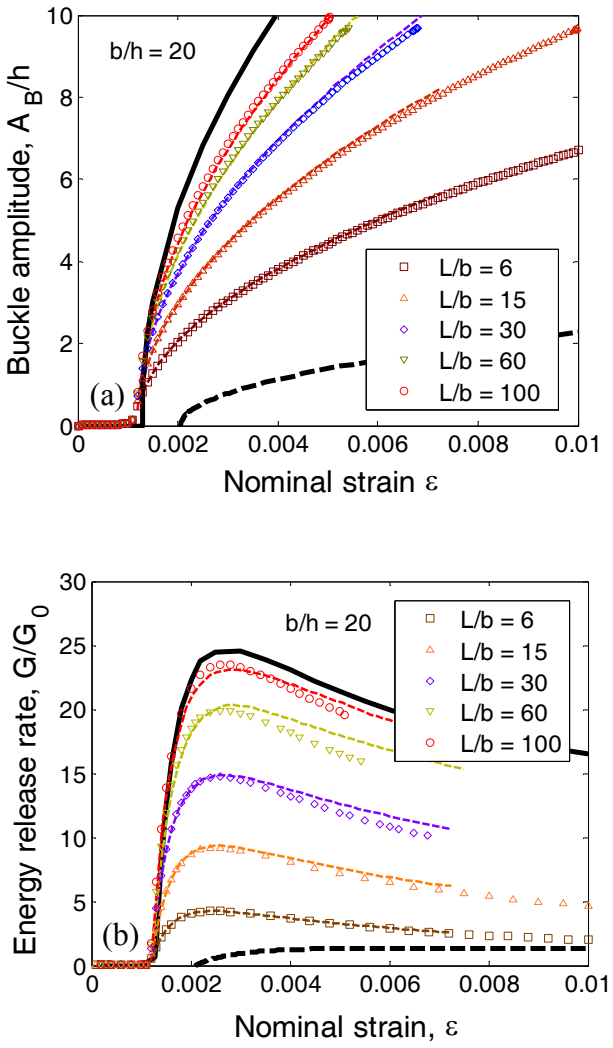

Figure 2.17: (a) Buckle amplitude and (b) energy release rate for $b/h = 20$. Two different finite element models are used and compared along with the semi-analytical solution (thick solid lines). The results from the 2D model are the open symbols, and those from the 1D model are the dashed lines. The thick dashed lines are the rigid-substrate solution in Eqs. (2.23) and (2.24).

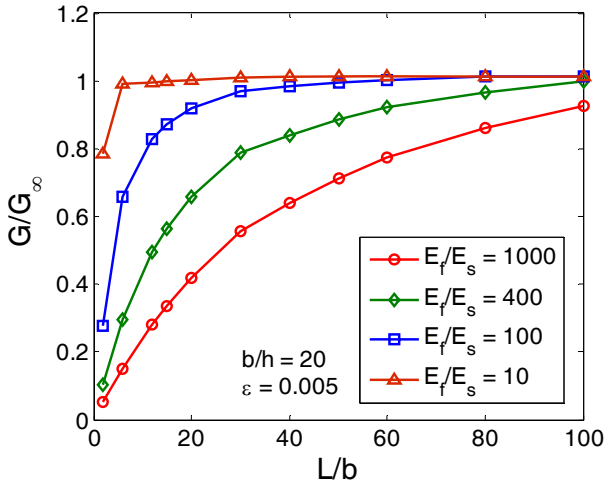

Figure 2.18: Dependence of the energy release rate for buckle-delamination on the length ratio (L/b) and the modulus ratio (E_f/E_s).

The thickness of the substrate in the 2D finite element model must be sufficiently large to simulate an infinitely thick substrate. As shown in Fig. 2.4, the thickness ratio H/h = 100 is sufficient for the wrinkling analysis. For buckling with delamination, the thickness ratio depends on the delamination size, and H/h = 200 is found to be sufficient for b/h up to 50 in the present study. For comparison, the results from the 1D finite element method (Appendix A) are shown in Fig. 2.17, in which the substrate is modeled exactly as an infinite half plane. The results from both finite element methods are in close agreement for the wrinkling analysis and for the eigenvalue analysis of buckling with delamination. For the post-buckling analysis, the two methods agree closely for the buckle amplitude but differ slightly for the energy release rate. The discrepancy may be attributed to the calculation of the J-integral with different models for the film (i.e., 2D solid elements vs 1D beam elements) and for the substrate (i.e., finite thickness vs

infinite).

For a very compliant substrate, it is found that localized buckle-delamination and periodic wrinkles may co-exist when L/b is sufficiently large. Figure 2.19 shows two examples, one for $b/h = 10$ and the other for $b/h = 50$. In both cases, the onset of buckle-delamination occurs first, followed by formation of periodic wrinkles. The buckle amplitude is much larger than the wrinkle amplitude, and the film is nearly flat in a region between buckle-delamination and periodic wrinkles. The wrinkle wavelength agrees closely with the prediction by the analytical solution in Eq. (2.12). This implies that the wrinkle wavelength is a reliable quantity for the measurement of elastic properties, as long as the nominal strain is within the limit of linear elasticity. Unless the substrate is nearly incompressible ($\nu_s \sim 0.5$), the effect of Poisson's ratio should be taken into account by using Eq. (2.12) instead of Eq. (2.2). Figure 2.20 shows the surface contours for $b/h = 50$ at two different strain levels, mimicking what may be observed in experiments by an optical micrograph shown in Fig. 1.3b [21]. When the nominal strain is low, only the localized buckle is observable at the location of pre-existing delamination. At a higher strain, periodic wrinkles form at a distance away from the delamination. Between the wrinkles and buckle-delamination is a region of interaction, where the compressive stress in the film is partly relaxed by buckle-delamination at one side and by wrinkling at the other side. The stress varies over a distance that depends on the size of delamination (b/h) as well as the substrate compliance by the shear lag effect. The stress variation is reflected by the variation of the wrinkle amplitude from zero to nearly constant (Fig. 2.19).

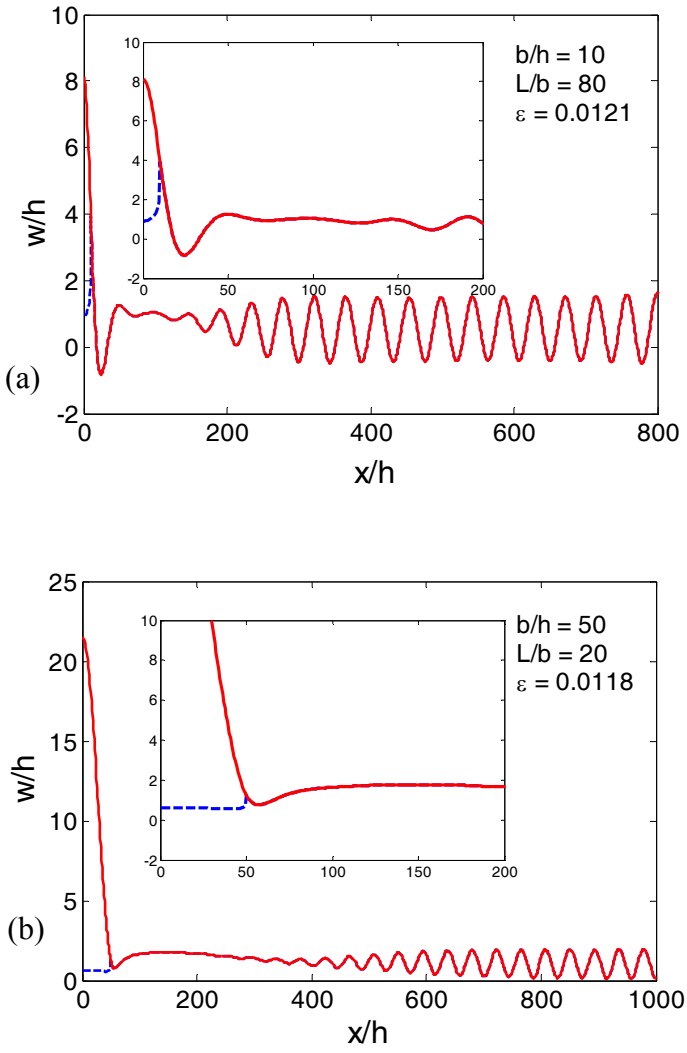

Figure 2.19: Concomitant wrinkling and buckle-delamination of a thin film on a compliant substrate (E_f/E_s = 1000) with (a) b/h = 10 (L/h = 800) and (b) b/h = 50 (L/h = 1000). The dashed line indicates the substrate surface. The insets show the local view near the edge of delamination.

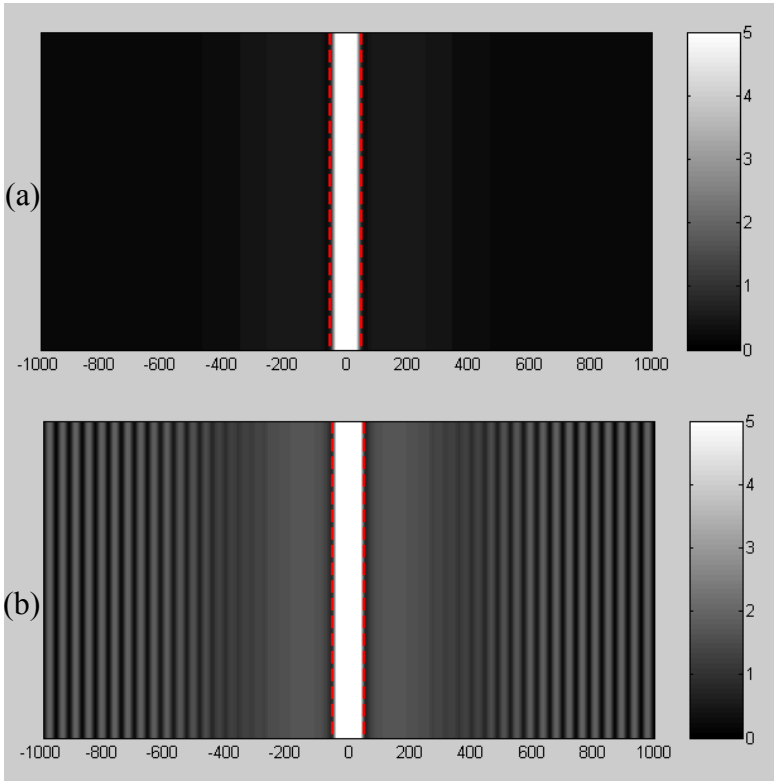

Figure 2.20: Gray-scale contour plots of the surface profiles for $b/h = 50$ at two different strain levels: (a) $\varepsilon = 0.0032$; (b) $\varepsilon = 0.0118$. The red dashed lines indicate the edges of delamination.

Figure 2.21a plots the buckle amplitude as a function of the nominal strain for the case with $b/h = 50$ and $L/b = 20$, and Fig. 2.21b plots the energy release rate for growth of the delamination. The critical strain for onset of buckling in this case is very small (~0.00026). Beyond the critical strain, the buckle amplitude and the energy release rate increase. For comparison, the rigid-substrate solution in Eqs. (2.23) and (2.24) are plotted as the thick dashed lines, and the semi-analytical solutions by Yu-Hutchinson approach are plotted as the thick solid lines. Both the buckle amplitude and the energy release rate by the finite element model are lower than the semi-analytical solution, because the ratio

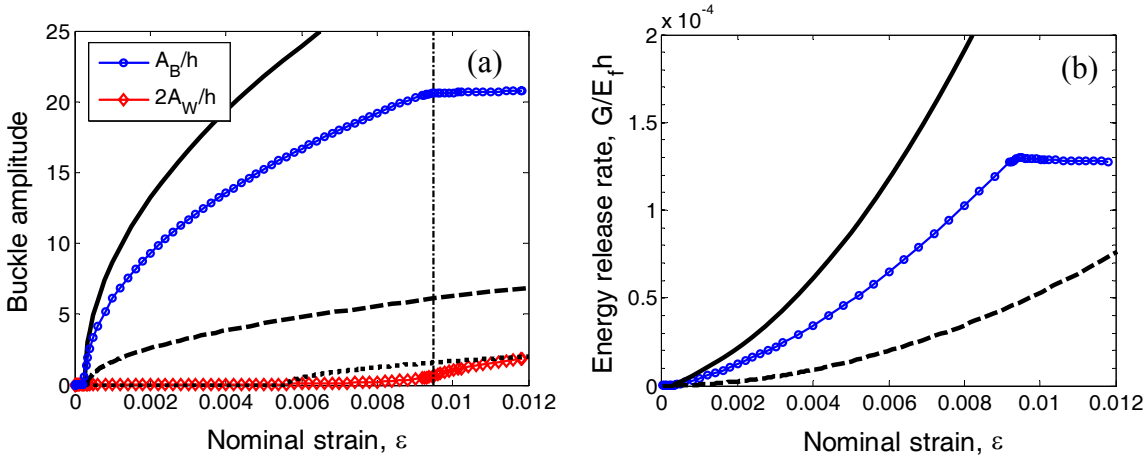

Figure 2.21: (a) Amplitudes of buckling and wrinkling for b/h = 50 (L/b = 20 and H/h = 200). (b) Energy release rate for delamination. The thick solid lines are the semi-analytical solution, and the thick dashed lines are the rigid-substrate solution in Eqs. (2.23) and (2.24). The thick dotted line in (a) is twice the wrinkle amplitude by Eq. (2.16) assuming no delamination.

L/b = 20 is not large enough to simulate an infinite substrate as assumed by the semi-analytical solution. Furthermore, when the nominal strain reaches around 0.0092, both the buckle amplitude and the energy release rate stop increasing. This change of behavior coincides with the onset of wrinkling away from the delamination (Fig. 2.21a). The effect of the growth of wrinkling on the energy release rate and thus the growth of delamination indicates that in some cases the pre-existing delamination could be pinned by the wrinkles, as the energy release rate stops increasing once wrinkles start to grow. On the other hand, it is noted that the nominal strain for onset of wrinkling in Fig. 2.21a is greater than the analytical prediction by Eq. (2.13). Therefore, while the growth of wrinkling reduces the buckle amplitude and the energy release rate, the presence of buckle-delamination delays onset of wrinkling. With a very compliant substrate, the two

buckling modes interact over a long range with a length scale more than three orders of magnitude greater than the film thickness.

2.4 Cohesive zone modeling

The previous sections have considered two scenarios for concomitant wrinkling and buckle-delamination of an elastic thin film on a compliant substrate. First, if the film/substrate interface is perfectly bonded, wrinkling occurs beyond a critical strain. Subsequently, nucleation of interfacial delamination may occur at a larger nominal strain when the wrinkle-induced normal traction at the interface exceeds the strength of the interface. The growth of the interfacial delamination however requires further studies, for which a cohesive zone model may be adopted for the interface [88]. Second, if interfacial delamination pre-exists, the initial buckling mode depends on the size of the pre-existing delamination. With a relatively large delamination, localized buckle-delamination occurs first, followed by wrinkling away from the delamination. Again, the growth of interfacial delamination may be studied by using the cohesive zone model. In this section, the approach of cohesive zone model is employed to study the nucleation and subsequent growth of wrinkle-induced delamination without assuming a pre-existing interfacial crack.

As illustrated in Fig. 2.22, a two-dimensional finite element model is constructed in ABAQUS, subject to the same boundary conditions as the finite element model in Fig. 2.3. Both the film and the substrate are modeled by 2D quadrilateral elements (CPE8R). In addition, a layer of cohesive elements (COH2D4) is assigned along the interface to model the interaction between the film and the substrate. The bilinear traction-separation

relation, as illustrated in Fig. 1.9, is used to characterize the constitutive behavior of the cohesive elements.

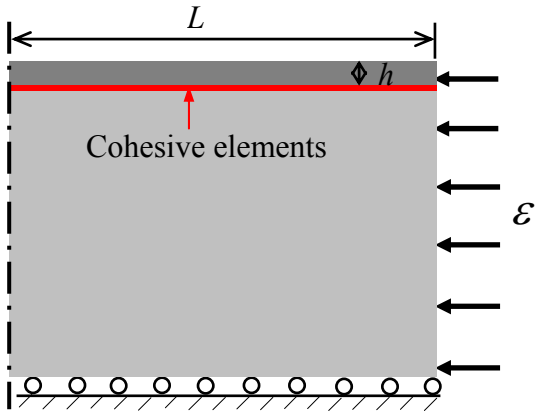

Figure 2.22: Schematic illustration of the finite element model, with a layer of cohesive elements along the interface between the film and the substrate.

A crack along an interface is typically under a mixed-mode condition due to elastic mismatch between the film and the substrate. Consequently, as introduced in Chapter 1, both the properties in modes I and II are required to define the interfacial constitutive behavior. For the bilinear traction-separation model, the interfacial properties to be specified include: the initial elastic stiffness K_n and K_s, the cohesive strength σ_n and τ_s, and the interface toughness Γ_I and Γ_{II}. In this section, however, we ignore the effect of mode mix by taking $K_n = K_s = K_0$, $\sigma_n = \tau_s = \sigma_0$ and $\Gamma_I = \Gamma_{II} = \Gamma$ for the interface. Previous studies have suggested that the initial elastic stiffness K_0 plays a less important role in cohesive zone modeling. In the present study, the initial stiffness K_0 is taken to be a constant (with $K_0 h / \overline{E}_f = 1$) in all simulations, while the strength (σ_0) and toughness (Γ)

are varied. The elastic properties for the film and the substrate are such that E_f/E_s =1000 and $\nu_f = \nu_s = 1/3$.

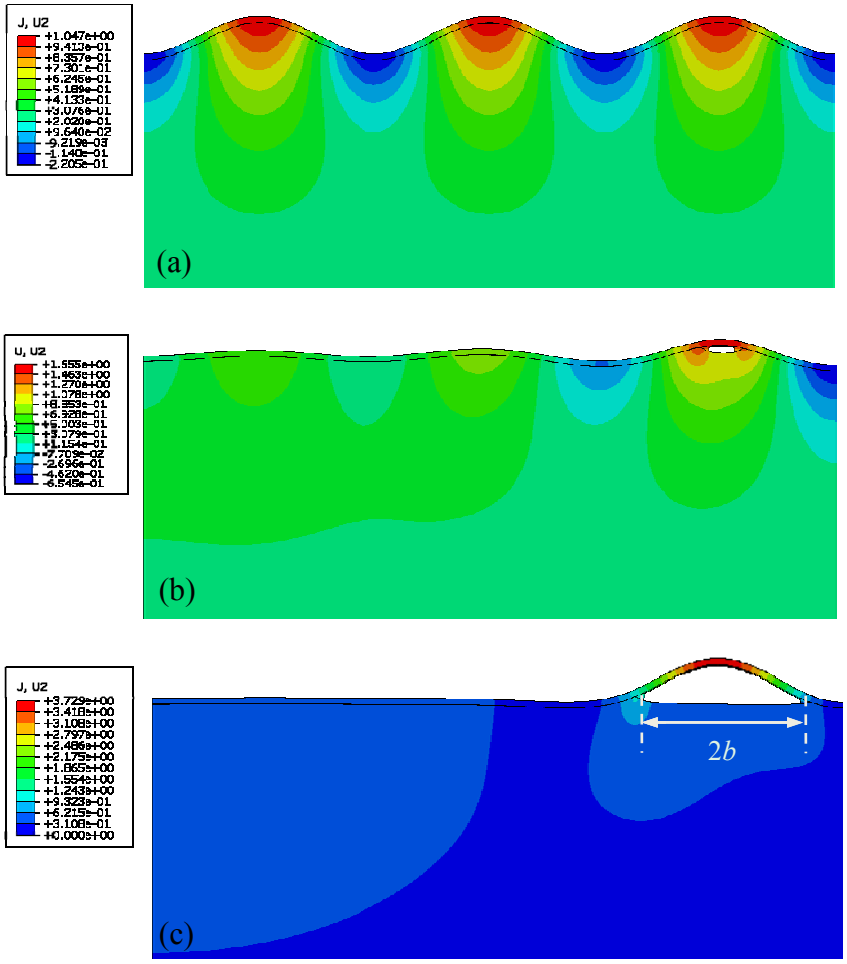

Figure 2.23: Numerical simulation of progressive wrinkling and interfacial delamination for an elastic thin film on a compliant substrate subject to increasing compression: (a) wrinkling with no delamination; (b) initiation of wrinkle-induced delamination; (c) subsequent growth of interfacial delamination.

Figure 2.23 shows an example of the numerical simulation, with snapshots of the deformation profile at three different stages: (a) wrinkling without interfacial

delamination, (b) initiation of wrinkle-induced delamination, and (c) subsequent growth of interfacial delamination, starting from an elastic film perfectly bonded to a compliant substrate. As the applied compressive strain increases, the film wrinkles first, followed by nucleation of an interfacial crack at one of the wrinkle crests. Upon subsequent growth of the delamination, buckling of the film becomes localized while the neighboring wrinkles are flattened. In this section, the onset of wrinkle-induced delamination is discussed first, and then the evolution of buckle-delamination is studied.

2.4.1 Initiation of wrinkle-induced delamination

In Section 2.1.3, initiation of wrinkle-induced delamination is predicted by comparing the maximum normal traction at the interface with the strength of the interface. This strength-based criterion for crack initiation is found to be in good agreement with the numerical results by the cohesive zone modeling approach. With the 2D finite element model with cohesive interface elements, a linear eigenvalue analysis is performed first. Using the first three eigen modes as the initial geometric imperfection, a nonlinear post-buckling analysis is performed to simulate progressive wrinkling and wrinkle-induce delamination, as shown in Fig. 2.23. The amplitude of wrinkling or buckling is plotted as a function of the nominal strain in Fig. 2.24 for three different values of the interfacial strength, whereas the interfacial toughness is taken to be a constant, $\Gamma/\bar{E}_f h = 10^{-5}$. For comparison, the wrinkle amplitude from the post-buckling analysis without using the cohesive elements (Section 2.1.2) is plotted as a continuous solid line. For each value of the interfacial strength, the wrinkle amplitude follows the

solid line before the initiation of delamination. At a critical nominal strain that depends on the interfacial strength, a delamination crack is nucleated (Fig. 2.23b) and the buckle amplitude at the location of delamination increases abruptly, deviating from the solid line. Thus, the initiation of delamination may be readily observable in experiments by measuring the buckle amplitude.

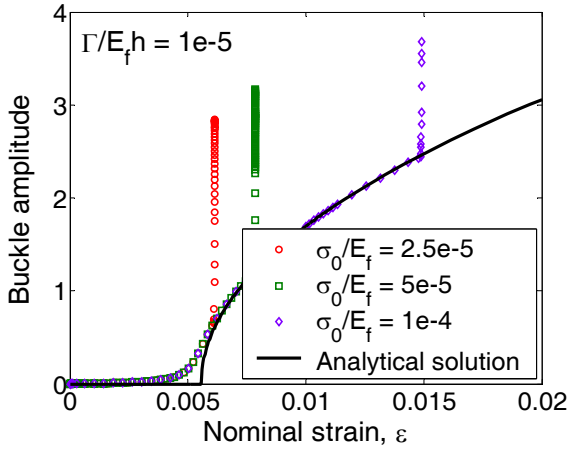

Figure 2.24: Buckle amplitude as a function of the nominal strain, for three different values of interfacial strength, $\sigma_0/\overline{E}_f$ = 2.5×10^{-5}, 5×10^{-5}, and 10^{-4}. The solid line represents the wrinkle amplitude by the analytical solution in Eq. (2.16).

The critical strain for initiation of wrinkle-induced delamination may be determined from Fig. 2.24. Alternatively, by the cohesive zone model, each cohesive element is characterized by a damage parameter (D), which varies between 0 and 1 during the separation process as discussed in Chapter 1. Thus, the critical strain for crack nucleation can be determined numerically when the damage parameter reaches 1 for at least one of the cohesive elements. Figure 2.25 plots the critical strain for wrinkle-

induced delamination as a function of the interfacial strength, obtained from the cohesive zone modeling approach for three different values of interface toughness. For comparison, the critical strain predicted by the analytical formula in Eq. (2.19) is plotted as the solid line. Clearly, the critical strain is nearly independent of the interface toughness, justifying the strength-based criterion. The numerical results by the cohesive zone modeling approach agree closely with the analytical prediction by Eq. (2.19) for relatively low interfacial strengths (e.g., $\sigma_0/\overline{E}_f < 10^{-4}$). For higher interfacial strengths, however, Eq. (2.19) underestimates the critical strain from the cohesive zone model. Apparently, as the critical strain increases with increasing interfacial strength, the linear approximation of the normal traction that leads to Eq. (2.19) becomes increasingly inaccurate as the strain goes beyond a few per cent.

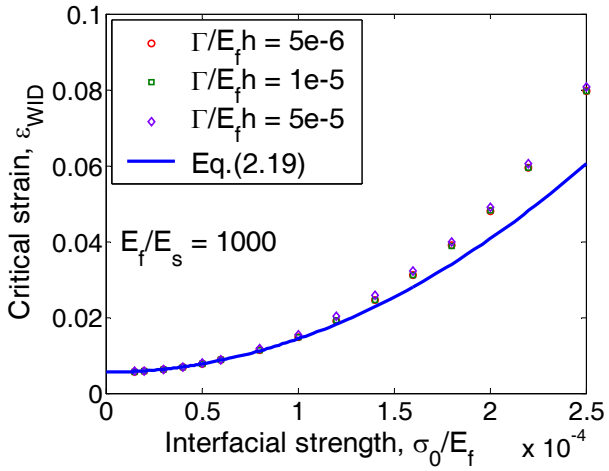

Figure 2.25: The critical strain for initiation of winkle-induced delamination as a function of the interfacial strength, comparing the results from cohesive zone modeling and the analytical prediction by Eq. (2.19).

2.4.2 Co-evolution of buckling and delamination

While the initiation of wrinkle-induced delamination is independent of the interface toughness, subsequent growth of the delamination crack does depend on the interface toughness. As shown in Fig. 2.26, for an interfacial strength $\sigma_0/\overline{E}_f = 5\times10^{-5}$,

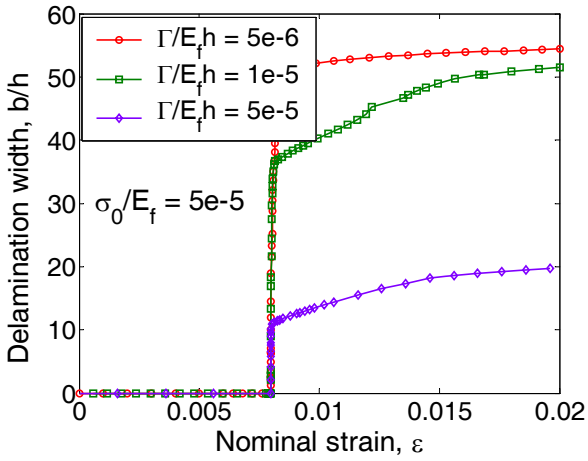

Figure 2.26: Delamination width as a function of the nominal strain for different values of interface toughness.

the delamination width (b) as a function of the nominal strain is plotted for three different values of interface toughness. The delamination width is determined from the cohesive zone model based on the damage parameters of the cohesive elements. The delamination width remains zero until the critical strain is reached. Upon initiation, the delamination crack grows rapidly, which in turn leads to rapid growth of the buckle amplitude as shown in Fig. 2.24. The growth of the interfacial crack is eventually stabilized with a delamination width depending on the interface toughness. Further increasing the

compressive strain, the delamination grows slowly and stably. Apparently, under the same nominal strain (greater than the critical strain), the delamination width decreases as the interface toughness increases.

The cohesive zone elements as implemented in ABAQUS assume an irreversible damage process, which may be used to simulate damage accumulation under cyclic loading. As an example, numerical simulation of a loading-unloading-reloading process is performed, with $\sigma_0 / \overline{E}_f = 5 \times 10^{-5}$ and $\Gamma / \overline{E}_f h = 10^{-5}$. Figure 2.27a shows the buckle amplitude versus the nominal strain. Before the first loading, the interface is perfectly bonded with no damage (D = 0). As the nominal strain increases, wrinkling occurs first at point A ($\varepsilon \sim 0.00556$), and wrinkle-induced delamination initiates at B ($\varepsilon \sim 0.0076$). Subsequently, delamination and buckling co-evolve. The corresponding delamination width is shown in Fig. 2.27b. Start unloading at point C (ε = 0.01). The delamination width remains a constant ($b/h \sim 40$) during unloading. Meanwhile, the buckle amplitude decreases, following a different path from C to D. The buckle amplitude is nearly zero at D, with the nominal strain ($\varepsilon \sim 0.000384$) corresponding to the critical strain for onset of buckling with $b/h \sim 40$. Upon reloading, the buckle amplitude follows the same path of unloading from D to C, during which the delamination does not grow. Further increasing the nominal strain beyond C to point E (ε = 0.02), the delamination grows and the buckle amplitude increases. Apparently, the buckle amplitude during reloading follows a drastically different path compared to that for the first loading. Such a behavior qualitatively agrees with an experiment by Vella et al. [20]. However, in their experiment, a discontinuous jump of the buckle amplitude during the first loading was reported,

presumably due to the unstable growth of the delamination.

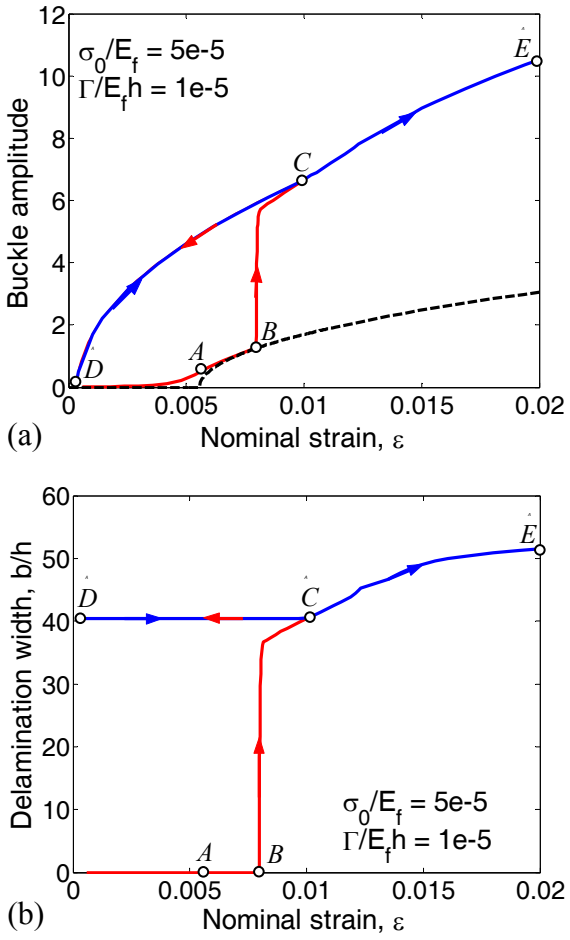

Figure 2.27: (a) Buckle amplitude and (b) delamination width as a function of the nominal strain during a loading-unloading-reloading cycle.

It is noted that the growth of buckle-delamination is strongly influenced by the boundary condition. When the crack tip approaches one end of the model, where the symmetric boundary condition is assumed, the energy release rate drops rapidly and the crack is arrested when the energy release rate is less than the interface toughness. Figure

2.28 shows the delamination width as a function of the nominal strain by finite element models with three different lengths (L). Apparently, as L increases, the delamination width increases upon initiation, while the critical strain for initiation is insensitive to the model size.

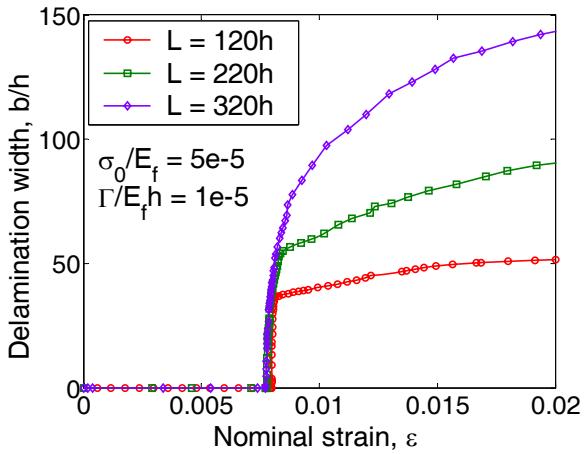

Figure 2.28: Delamination width as a function of the nominal strain for different lengths used in the finite element model, with interfacial properties $\sigma_0/\overline{E}_f = 5\times10^{-5}$ and $\Gamma/\overline{E}_f h = 10^{-5}$.

In section 2.3, it has been found that the results from the post-buckling analysis strongly depend on the ratio, L/b, in the finite element model, and the substrate thickness (H) must be sufficiently large to simulate an infinitely thick substrate for buckling with delamination. With a sufficiently large L/b, the localized buckle-delamination and periodic wrinkles may co-exist, as shown in Figs. 2.19 and 2.20. To simulate both initiation and co-evolution of wrinkling and buckle-delamination, the finite element model with cohesive elements is employed with $L = 1000h$ and $H = 200h$. The bilinear

traction-separation relation is assumed for the interface with $\sigma_0/\overline{E}_f = 5\times10^{-5}$ and $\Gamma/\overline{E}_f h = 5\times10^{-5}$. Similar to previous simulations, the first three eigen modes are obtained from a linear eigenvalue analysis and used as the initial imperfection for the post-buckling analysis. Figure 2.29 shows the evolution of deformation profiles of the film (solid lines) and the substrate surface (dashed lines) with increasing nominal strain. The film remains flat until the nominal strain reaches the critical strain for wrinkling ($\varepsilon_W = 0.00556$). Beyond the critical strain, periodic wrinkles form as shown in Fig. 2.29a at ε = 0.00758. The wrinkle wavelength and amplitude agree closely with the analytic predictions in Section 2.1.1. As the nominal strain increases to the critical value for wrinkle-induced delamination ($\varepsilon_{WID} = 0.0076$), an interfacial crack initiates and grows rapidly, as shown in Figs. 2.29b and 2.29c for two strains slightly above the critical strain. The growth of delamination leads to large, localized buckling, which relaxes the compressive stress in the film over a region close to the delamination. As a result, the wrinkles are flattened in the relaxation region. Further away from the delamination, the film remains wrinkled. As discussed in Section 2.3, where the delamination width is fixed, the size of the relaxation region depends on the relative compliance of the substrate and the delamination width. With continuous growth of the delamination and a finite length ($L = 1000h$) in the finite element model, all the wrinkles are flatted eventually, as shown in Fig. 2.29d.

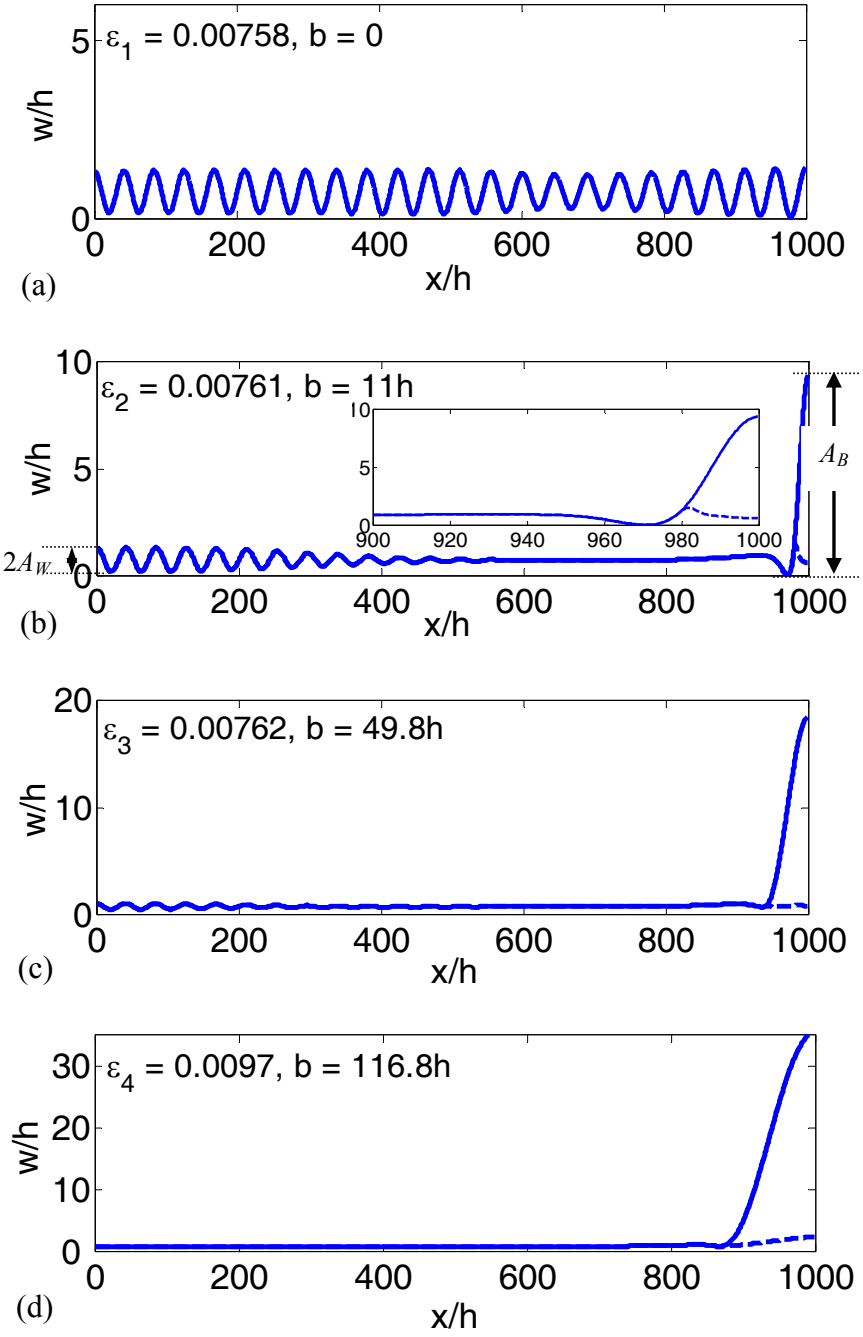

Figure 2.29: Out-of-plane displacement of the film (solid lines) and the substrate surface (dashed lines) at four different nominal strains: (a) ε = 0.00758 before delamination; (b) ε = 0.00761 ($b = 11h$); (c) ε = 0.00762 ($b = 49.8h$); (d) ε = 0.0097 ($b = 116.8h$). The inset in (b) shows the local view near the edge of delamination.

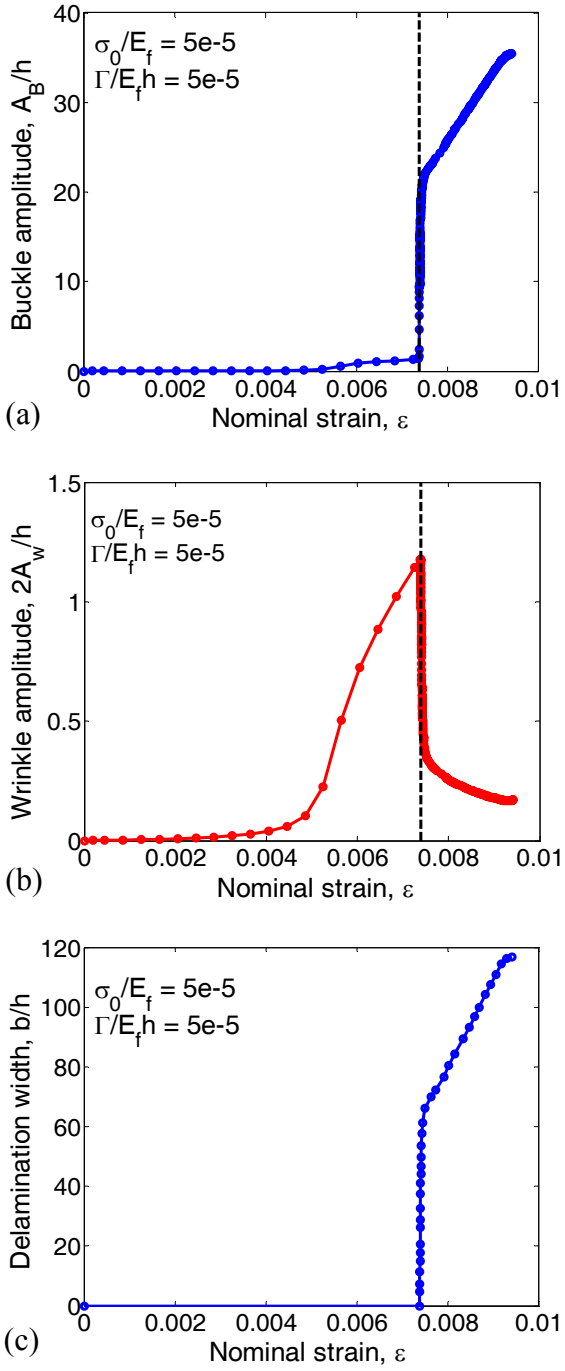

Figure 2.30: (a) Buckle amplitude, (b) wrinkle amplitude, and (c) delamination width, as a function of the nominal strain, with interfacial properties $\sigma_0 / \overline{E}_f = 5 \times 10^{-5}$ and $\Gamma / \overline{E}_f h = 5 \times 10^{-5}$.

Figure 2.30a shows the evolution of the buckle amplitude (A_B) as a function of the nominal strain. The buckle amplitude is defined as the difference between the maximum out-of-plane displacement and the minimum out-of-place displacement, as illustrated in Fig. 2.29b. Before initiation of interfacial delamination, the buckle amplitude is twice the wrinkle amplitude by definition. Upon interfacial delamination, the buckle amplitude grows abruptly, while the wrinkle amplitude as measured far away from the location of delamination (Fig. 2.29b) drops significantly, as shown in Figs. 2.30a and 2.30b. The dashed line indicates the critical strain for initiation of wrinkle-induced delamination. In Fig. 2.30c, the delamination width is plotted as a function of the nominal strain. Similar to the previous examples (e.g., Figs. 2.26 and 2.28), the interfacial delamination propagates rapidly upon initiation, followed by stable growth with increasing strain. Interestingly, as the nominal strain reaches a certain level ($\varepsilon \sim 0.0095$), the interfacial delamination stops growing. Meanwhile, from the amplitude curves in Fig. 2.30a, the buckle amplitude stops growing as well, while the wrinkle amplitude starts to grow. The numerical simulation becomes highly unstable at this point and stops due to divergence. Nevertheless, with a sufficiently large length in the finite element model, the results in Fig. 2.29 and Fig. 2.30 show initiation and co-evolution of wrinkling and buckle-delamination progressively as the nominal strain of compression increases.

2.5 Comments on applications for thin film metrology

It has been suggested that the phenomena of wrinkling and buckle-delamination may offer a convenient approach to measuring elastic properties of thin film materials [15]

as well as adhesion energy of the interface [20, 23]. Based on the present study, we would make the following comments.

- The wrinkle wavelength is a reliable quantity for the measurement of elastic properties, as long as the nominal strain is within the limit of linear elasticity. Unless the substrate is nearly incompressible ($v_s \sim 0.5$), the effect of Poisson's ratio should be taken into account by using Eq. (2.12) instead of Eq. (2.2).
- The wrinkle amplitude is less reliable as it depends sensitively on pre-existing delamination (Fig. 2.16), which is often uncertain in experiments.
- To determine the interface toughness or adhesion energy from buckle-delamination, both the delamination width and the nominal strain are needed for the calculation of energy release rate, which equals the interface toughness when the delamination crack is arrested. Measurement of the buckle amplitude could help to infer one of the two quantities, but no explicit relationships are obtained for either the buckle amplitude or the energy release rate. In particular, we were not able to confirm the simple formula obtained by a scaling analysis [20].
- With concomitant wrinkling and buckle-delamination, it is possible to simultaneously determine the elastic property of the thin film and the interfacial properties. First, by measuring the wrinkle wavelength far away from the buckle-delamination, the elastic modulus of the thin film can be determined by Eq. (2.12), assuming that the elastic properties of the substrate are known. Second, if the critical strain for wrinkle-induced nucleation of buckle-delamination can be measured, the strength of the interface may be determined by Eq. (2.19). As

shown in Fig. 2.24, the buckle amplitude increases abruptly at the critical strain, which may be practically measurable. Third, once the delamination crack has arrested at a particular strain level, the interface toughness can be determined by calculating the energy release rate with the measured delamination width and the buckle amplitude.

2.6 Summary

In summary, this chapter presents a study on wrinkling and buckle-delamination for an elastic film on a highly compliant substrate under compression. First, without delamination, we present an analytical solution for wrinkling that takes into account the effect of Poisson's ratio of the substrate. In comparison with a nonlinear finite element analysis, an approximate formula is derived to estimate the normal traction at the interface and to predict initiation of wrinkle-induced delamination. Next, with a pre-existing delamination crack, the critical strain for the onset of buckling instability is predicted by a semi-analytical solution and by finite element eigenvalue analysis. It is found that, for an intermediate delamination size, the critical compressive strain for onset of buckling is lower than the previous solutions for both wrinkling and buckle-delamination. By comparing the critical strain, a diagram for the initial buckling modes is constructed with respect to the film/substrate stiffness ratio and the interfacial defect size. Nonlinear post-buckling analysis is then conducted to simulate concomitant wrinkling and buckle-delamination, with a long-range interaction between the two buckling modes through the compliant substrate. Finally, by using a layer of cohesive elements for the

interface, progressive co-evolution of wrinkling and delamination is simulated. In particular, the effects of interfacial properties (strength and toughness) on the initiation and propagation of wrinkling-induced interfacial delamination are examined. Relevant experimental observations and potential applications in thin-film metrology are discussed along with the theoretical and numerical analyses.

Chapter 3

Channel cracking of elastic thin films

Under tension, an elastic film may fracture. Constrained by the substrate, fracture of an elastic thin film results in channel cracks as shown in Fig. 1.4. Figure 3.1a shows a schematic illustration of a straight channel crack in a thin film. Such a channel crack typically nucleates from surface defects, grows down towards the substrate, and is arrested near the film/substrate interface [39]. Subsequently, the crack advances in the in-plane direction as a channeling crack. The driving force for growth of channel cracks depends on the constraint by the substrate, which has been studied previously [26, 27, 97]. Most of the previous studies assumed that the root of the channel crack lies on the interface (Fig. 3.1a). However, it is known that the stress field diverges at the root [98], which may cause delamination of the interface or cracking of the substrate, as illustrated in Fig. 3.1b and Fig. 3.1c, respectively. With interfacial delamination or substrate cracking, the effect of substrate constraint on the channel crack is reduced, thus increasing the driving force for growth of the channel crack. Such an effect becomes significant for a stiff elastic film on a compliant substrate. In this chapter, using a set of finite element models, the effects of interfacial delamination and substrate cracking on channel cracking of elastic thin films are analyzed. By both the linear elastic fracture mechanics and cohesive zone modeling, the competition between delamination and substrate cracking is discussed.

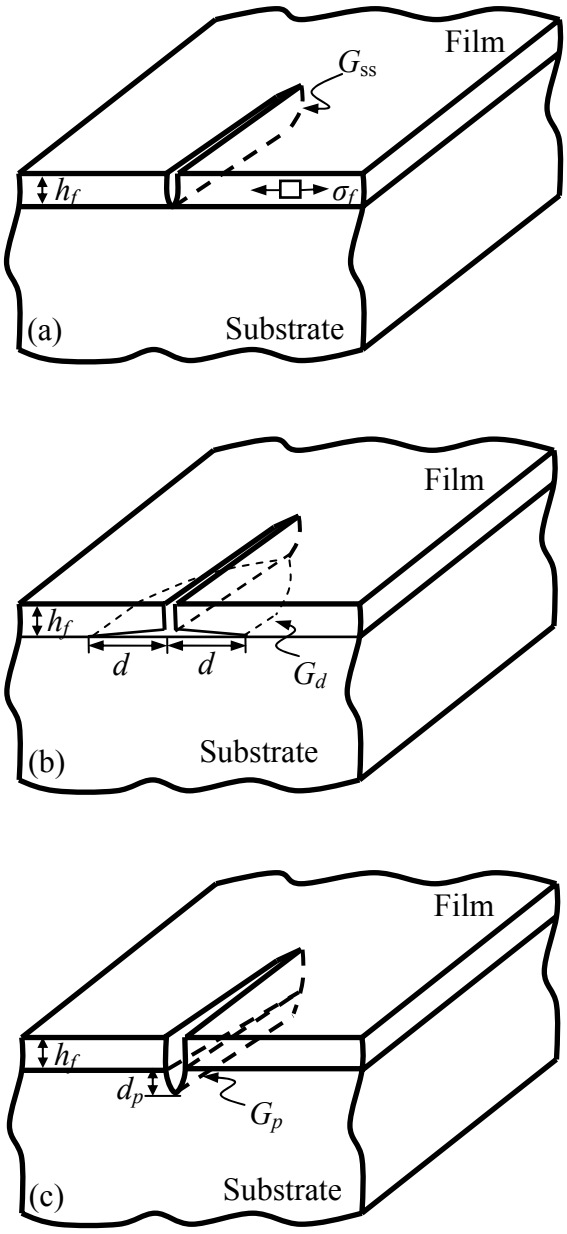

Figure 3.1: Schematic illustrations of (a) channel cracking, (b) concomitant channel cracking and interfacial delamination, and (c) concomitant channel cracking and substrate penetration.

3.1 An ideal channel crack

As illustrated in Fig. 3.1a, assuming no delamination or penetration, the energy release rate for steady state growth of an ideal channel crack in an elastic thin film bonded to an elastic substrate is [26, 39]:

$$G_{ss} = Z(\alpha, \beta)\frac{\sigma_f^2 h_f}{\overline{E}_f} \tag{3.1}$$

where σ_f is the tensile stress in the film, h_f is the film thickness, and $\overline{E}_f$ is the plane strain modulus. The dimensionless coefficient Z depends on Dundurs' parameters for elastic mismatch between the film and the substrate as defined in Eq. (1.3).

When the film and the substrate have identical elastic moduli, we have $\alpha = \beta = 0$ and $Z = 1.976$. The value of Z decreases slightly for a compliant film on a relatively stiff substrate ($\overline{E}_f < \overline{E}_s$ and $\alpha < 0$). A more compliant substrate ($\alpha > 0$), on the other hand, provides less constraint against film cracking. Thus, Z increases as α increases. For very compliant substrates (e.g., organic low-k dielectrics, polymers, etc.), Z increases rapidly, with $Z > 30$ for $\alpha > 0.99$ [26, 27]. The effect of β is secondary and often ignored.

Numerically, the steady-state energy release rate of channel cracking can be calculated from a two-dimensional (2D) plane strain model [26, 27], as shown in Fig. 3.2, with

$$G_{ss} = \frac{\sigma_f}{2h_f}\int_0^{h_f} \delta(z)dz \tag{3.2}$$

where $\delta(z)$ is the opening displacement of the crack surfaces far behind the channel front (see Fig. 3.1a). Due to the constraint by the substrate, the crack opening does not change

as the channel front advances and the energy release rate attains a steady state, independent of the channel length. Three-dimensional analyses have shown that the steady state is reached when the length of a channel crack exceeds two to three times the film thickness for a relatively stiff substrate [99], but the crack length to reach the steady state can be significantly longer for more compliant substrate materials [97]. The present study focuses on the steady state only.

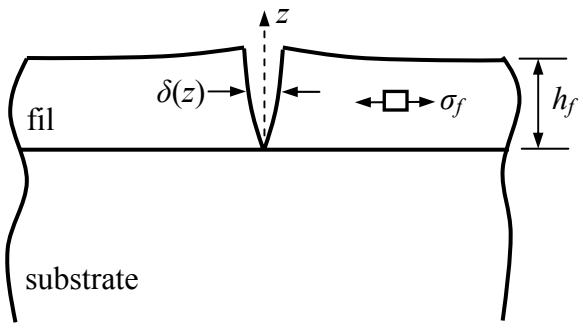

Figure 3.2: Schematics of the 2D plane strain model for an ideal channel crack.

3.2 Effect of interfacial delamination

3.2.1 Interfacial delamination from channel root

Now consider an interface crack emanating from the channel root at each side (Fig. 3.1b). For a long, straight channel crack, we assume a steady state far behind the channel front, where the interfacial crack has a finite width. The energy release rate for the interfacial crack can be written in a similar form as Eq. (3.1):

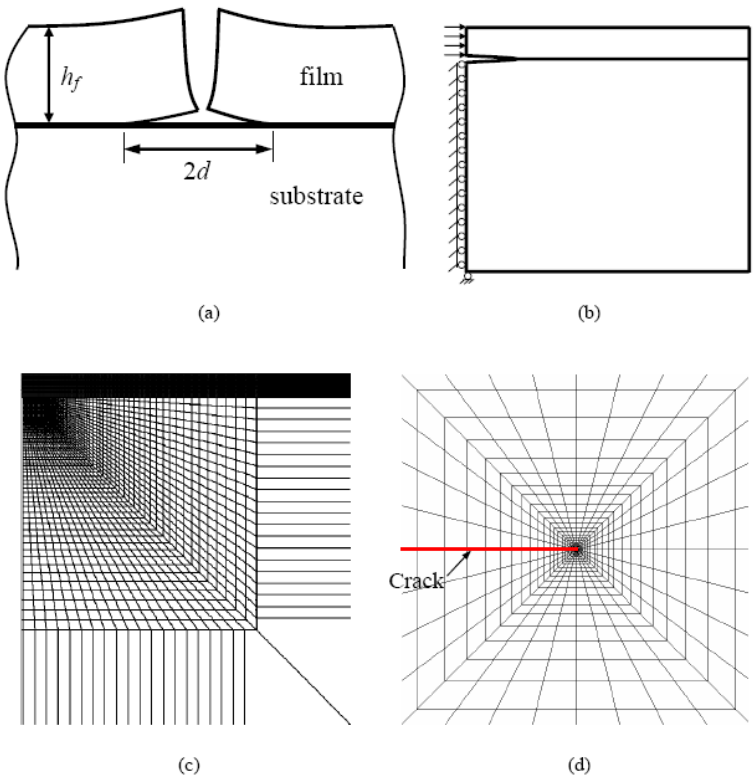

Figure 3.3: (a) Schematics of the 2D plane strain model of a steady-state channel crack with interfacial delamination; (b) geometry of the finite element model, with uniform normal traction (σ_f) acting onto the surface of the channel crack and a symmetry boundary condition for the substrate; (c) an example finite element mesh, with infinity elements along the bottom and right boundaries; (d) a detailed mesh around the tip of the interfacial crack.

$$G_d = Z_d\left(\frac{d}{h_f}, \alpha, \beta\right)\frac{\sigma_f^2 h_f}{\overline{E}_f} \tag{3.3}$$

where d is the width of delamination and Z_d is a dimensionless function that can be determined from a two-dimensional plane strain problem as illustrated in Fig. 3.3a. In the present study, a finite element model is constructed to calculate the interfacial energy release rate. By symmetry, only half of the film/substrate structure is modeled along with

proper boundary conditions (Fig. 3.3b). The finite element package ABAQUS[68] is employed and an example mesh near the interfacial crack is shown in Fig. 3.3c. Close to the tip of the interfacial crack, a very fine mesh is used (Fig. 3.3d), with a set of singular elements around the crack tip. Far away, infinite elements are used for both the film and substrate to eliminate possible size effects of the model. In all calculations, we set $v_f = v_s$ =1/3 such that $\beta = \alpha/4$, while the mismatch parameter α is varied.

The method of J-integral is adopted for the calculation of the interfacial energy release rate G_d. The dimensionless coefficient Z_d is then determined by normalization of the numerical results according to Eq. (3.3), which is plotted in Fig. 3.4 as a function of the normalized delamination width, d/h_f, for different elastic mismatch parameters. The Z_d function has two limits. First, when $d/h_f \to \infty$ (long crack limit), the interfacial crack reaches a steady state with the energy release rate:

$$G_{ss}^{d} = \frac{\sigma_f^2 h_f}{2\bar{E}_f} \tag{3.4}$$

and thus $Z_d \to 0.5$. The steady-state energy release rate for the interfacial crack is independent of the crack length as well as the elastic mismatch. On the other hand, when $d/h_f \to 0$ (short crack limit), the interfacial energy release rate follows a power law [100]:

$$Z_d \sim \left(\frac{d}{h_f}\right)^{1-2\lambda} \tag{3.5}$$

where λ depends on the elastic mismatch and can be determined by solving the equation [98]:

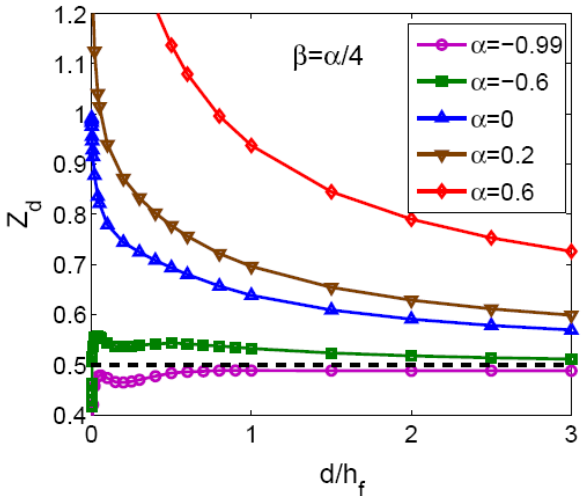

Figure 3.4: Normalized energy release rate of interfacial delamination from the root of a channel crack as a function of the normalized delamination width for different elastic mismatch parameters.

$$\cos\lambda\pi = \frac{2(\alpha-\beta)}{1-\beta}(1-\lambda)^2 - \frac{\alpha-\beta^2}{1-\beta^2} \tag{3.6}$$

More details about the solution at the short crack limit as well as comparisons with the finite element results are given in Appendix C. Here we discuss three scenarios at the short crack limit, which would eventually determine the condition for channel cracking with or without interfacial delamination. First, when $\alpha = \beta = 0$ (no elastic mismatch), we have $\lambda = 0.5$. In this case, Z_d approaches a constant as $d/h_f \rightarrow 0$. As shown in Appendix C, an analytical solution predicts that Z_d $(0,0,0) \rightarrow 0.9878$, which compares well with our numerical results (Fig. C.2). When $\alpha > 0$ ($\beta = \alpha/4$), we have $\lambda > 0.5$. Consequently, $Z_d \rightarrow \infty$ as $d/h_f \rightarrow 0$. As shown in Fig. 3.4, for both $\alpha = 0$ and $\alpha > 0$, the interfacial energy release rate monotonically decreases as the delamination width increases. On the other hand, when $\alpha < 0$, we have $0 < \lambda < 0.5$, and thus, $Z_d \rightarrow 0$ as $d/h_f \rightarrow 0$. Interestingly, the

numerical results in Fig. 3.4 show that, instead of a monotonic variation with respect to the crack length, the interfacial energy release rate oscillates between the short and long crack limits for the cases with $\alpha < 0$. Such an oscillation leads to local maxima of the interfacial energy release rate, which in some cases (e.g., $\alpha = -0.6$) can be greater than the steady state value at the long crack limit.

Previously, Ye et al. [101] gave an approximate formula for the Z_d function based on their finite element calculations. Although the formula has similar asymptotic limits for long and short cracks as the analytical solutions, it gives inaccurate results for at least two cases. First, in the case of no elastic mismatch, the formula predicts that $Z_d \rightarrow 0.748$ as $d/h_f \rightarrow 0$, about 25% lower than the analytical solution. Second, the interfacial energy release rates for intermediate crack lengths by the approximate formula in general do not compare closely with numerical results, especially for cases with $\alpha < 0$, where the oscillation and the maxima are not well captured by the approximation. As will be discussed later, the maximum interfacial energy release rate for $\alpha \leq 0$ is critical for determining the condition of interfacial delamination alongside the channel crack. Another previous study by Yu et al. [102] investigated interfacial delamination under two different edge conditions. While the steady-state interfacial energy release rate is the same for all edge conditions, the short crack limit strongly depends on the edge effect.

A necessary condition for steady-state channel cracking with concomitant interfacial delamination is that the interfacial crack arrests at a finite width. The delamination width can be determined by comparing the interfacial energy release rate in Eq. (3.3) to the interface toughness. As discussed in Chapter 1, the interface toughness

depends on the phase angel of mode mix [39], which in turn depends on the delamination width, as shown in Fig. 3.5. Due to the oscillatory nature of the stress singularity at the interfacial crack tip [45], a length scale has to be used for the definition of phase angle as in Eq. (1.4). Here we take the film thickness as the length scale, with $l = h_f$. The real and imaginary parts of the complex stress intensity factor in Eq. (1.4) are calculated by the interaction integral method in ABAQUS[68]. Figure 3.5 shows that the phase angle quickly approaches a steady state

$$\psi_{ss} = \omega(\alpha, \beta) \tag{3.7}$$

as given by Suo and Hutchinson [103]. When the film and the substrate have identical elastic moduli ($\alpha = \beta = 0$), we have $\psi_{ss} = \omega(0,0) = 52.1^\circ$. Considering the fact that the variation of the phase angle with respect to the delamination width is relatively small and confined within a small range of short cracks ($d < h_f$), we take the constant steady-state phase angle, Eq. (3.7), in the subsequent discussions and assume that the interface toughness is independent of the delamination width, i.e., $\Gamma_i = \Gamma_i(\psi_{ss})$. Then, the width of the interfacial delamination can be determined by requiring that

$$Z_d\left(\frac{d_s}{h_f}, \alpha, \beta\right) = \overline{\Gamma}_i = \frac{\overline{E}_f \Gamma_i(\psi_{ss})}{\sigma_f^2 h_f} \tag{3.8}$$

The right-hand side of Eq. (3.8) is the normalized interface toughness, independent of the interfacial crack length. In the following, we discuss possible solutions to Eq. (3.8) for different elastic mismatches.

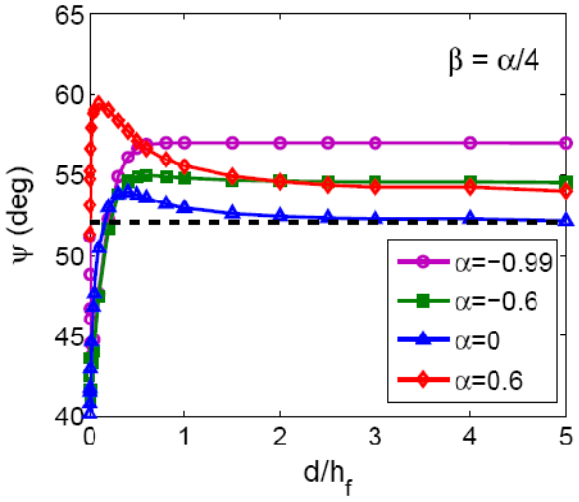

Figure 3.5: Phase angle of the mode mix for interfacial delamination as a function of the normalized delamination width for different elastic mismatch parameters. The dashed line indicates the steady-state phase angle (52.1°) for the case of zero elastic mismatch ($\alpha = \beta = 0$).

First, when $\alpha = \beta = 0$ (i.e., no elastic mismatch), the Z_d function has a maximum, $Z_d \rightarrow 0.9878$ as $d/h_f \rightarrow 0$, and it approaches the steady state, $Z_d \rightarrow 0.5$, for long cracks. Consequently, when $\overline{\Gamma}_i \geq 0.9878$ (tough interface), the interfacial energy release rate is always lower than the interface toughness, and thus no delamination would occur (i.e., $d_s = 0$). On the other hand, when $\overline{\Gamma}_i \leq 0.5$ (weak interface), the interfacial energy release rate is always higher than the interface toughness. In this case, the interfacial crack would grow unstably to infinity (i.e., $d_s \rightarrow \infty$), causing spalling of the film from the substrate, unless the interfacial crack is arrested by other features such as geometric edges or material junctions. Only for an intermediate interface toughness with $0.9878 > \overline{\Gamma}_i > 0.5$, Eq. (3.8) has a finite solution, $0 < d_s < \infty$, in which case the channel crack grows with

concomitant interfacial delamination of the width d_s. The stable delamination width is plotted as a function of the normalized interface toughness $\overline{\Gamma}_i$ in Fig. 3.6.

Next, when $\alpha > 0$ (i.e., a stiff film on a relatively compliant substrate), the function is unbounded as $d/h_f \rightarrow 0$. Thus, for all interfaces with $\overline{\Gamma}_i > 0.5$, a stable delamination width d_s can be obtained from Eq. (3.8). This indicates that interfacial delamination would always occur concomitantly with the channel crack when the substrate is more compliant than the film. As shown in Fig. 3.6, the delamination width increases as the normalized interface toughness decreases. When $\overline{\Gamma}_i \leq 0.5$, the interfacial crack grows unstably and the delamination width approaches infinity.

When $\alpha < 0$ (i.e., a compliant film on a relatively stiff substrate), the function necessarily starts from zero at $d/h_f = 0$, but has a local maximum (Z_{dm}) before it approaches the steady state value. The value Z_{dm} decreases as α decreases, which is greater than 0.5 when $0 > \alpha > -0.89$ and lower than 0.5 when $\alpha \leq -0.89$. Consequently, when $0 > \alpha > -0.89$, no interfacial delamination occurs if $\overline{\Gamma}_i \geq Z_{dm}$, and stable delamination if $0.5 < \overline{\Gamma}_i < Z_{dm}$. On the other hand, when $\alpha \leq -0.89$, stable delamination cannot occur; the channel crack either has no delamination for $\overline{\Gamma}_i \geq 0.5$ or causes unstable delamination for $\overline{\Gamma}_i < 0.5$. The stability of the interfacial delamination is dictated by the trend of the interfacial energy release rate with respect to the delamination width (Fig. 3.4). Although Eq. (3.8) has a finite solution for $\alpha < 0$ and $\overline{\Gamma}_i < 0.5$, the interfacial crack is unstable because $\partial Z_d / \partial d > 0$ (the minor oscillation of the Z_d function has been ignored here). Moreover, for both the stable and unstable delamination, a critical defect size is

required for the initiation of the interfacial delamination, since the energy release rate approaches zero for very short cracks ($d/h_f \to 0$). This sets a barrier for the initiation of interfacial delamination from the channel crack when the substrate is mechanically stiffer than the film.

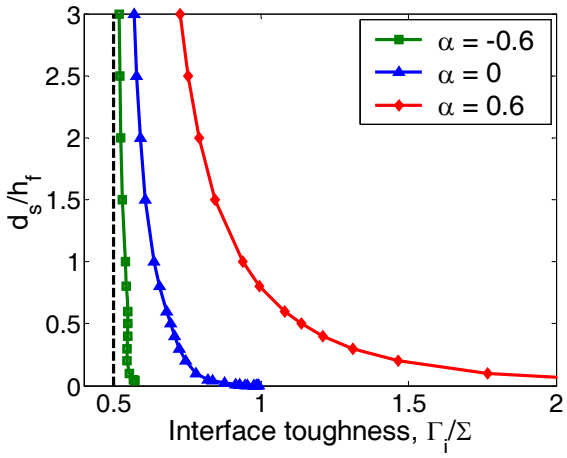

Figure 3.6: The normalized stable delamination width as a function of the normalized interface toughness $\overline{\Gamma}_i = \Gamma_i / \Sigma$, where $\Sigma = \sigma_f^2 h_f / \overline{E}_f$.

The above discussion is summarized in Fig. 3.7 as an interfacial delamination map for different combinations of film/substrate elastic mismatch and interface toughness. Three regions are identified for (I) no delamination, (II) stable delamination, and (III) unstable delamination. In regions II and III, sub-regions for delamination without and with an initiation barrier are denoted by A and B, respectively. The boundary between Region I and Region II-B is determined from the present finite element calculations, corresponding to the maximum interfacial energy release rate for $0 > \alpha > -0.89$. In an experimental study by Tsui et al. [25], no interfacial delamination was observed for

channel cracking of a low-k film directly deposited on a Si substrate, while a finite delamination was observed when a polymer buffer layer was sandwiched between the film and the substrate. These observations are consistent with the delamination map. In the former case, the elastic mismatch between the film and the substrate, $\alpha = -0.91$, thus

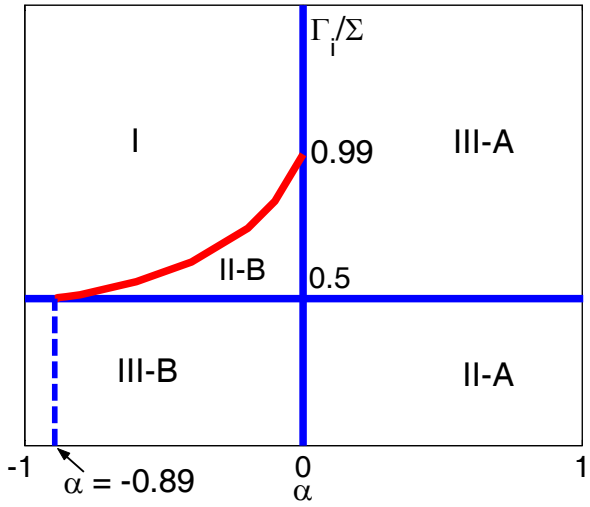

Figure 3.7: A map for interfacial delamination from the root of a channel crack ($\beta = \alpha/4$): (I) no delamination, (II) stable delamination, and (III) unstable delamination, where A and B denote delamination without and with an initiation barrier, respectively.

no delamination when the normalized interface toughness $\overline{\Gamma}_i \geq 0.5$ (i.e., Region I in Fig. 3.7). With a polymer buffer layer, however, the elastic mismatch between the low-k material and the polymer is, α = 0.4. Although the polymer layer is relatively thin, it qualitatively changes the interfacial behavior from that for $\alpha < 0$ (Region I) to that for $\alpha > 0$ (Region II-A). More experimental evidence with different combinations of elastic

mismatch, interface toughness, and film stress would be needed for further validation of the predicted delamination map.

3.2.2 Growth of channel crack with stable delamination

As the question regarding the occurrence of interfacial delamination from the root of a channel crack is addressed in the previous section, the next question is: how would the interfacial delamination influence the driving force for the growth of a channel crack? Again, we consider the steady-state growth. With a stable delamination along each side of the channel crack (Fig. 3a), the substrate constraint on the opening of the channel crack is relaxed. Consequently, the steady-state energy release rate calculated from Eq. (3.2) becomes greater than Eq. (3.1). A dimensional consideration leads to:

$$G_{ss}^{*} = Z^{*}\left(\frac{d_s}{h_f}, \alpha, \beta\right)\frac{\sigma_f^2 h_f}{\overline{E}_f} \tag{3.9}$$

where Z^{*} is a new dimensionless coefficient that depends on the width of interfacial delamination (d/h_f) in addition to the elastic mismatch parameters. From an energetic consideration, we obtain that:

$$G_{ss}^{*} = G_{ss} + \frac{2}{h_f}\int_0^{d_s} G_d(a)da \tag{3.10}$$

where G_{ss} is the steady-state energy release rate of the channel crack with no delamination as given in Eq. (3.1), and $G_d(a)$ is the energy release rate of the interfacial crack of width a as given in Eq. (3.3). When $d/h_f \to 0$, $G_{ss}^{*} \to G_{ss}$ or $Z^{*} \to Z$, recovering Eq. (3.1); when $d/h_f \to \infty$, $Z^{*} \to \infty$. Furthermore, as $d_s/h_f \to \infty$, since the

interfacial crack approaches the steady state ($G_d \to G_{ss}^d$ and $Z_d \to 0.5$), the increase of the energy release rate is simply

$$\Delta G_{ss}^* = \frac{2}{h_f} G_{ss}^d \Delta d \text{ , or } \Delta Z^* = \frac{\Delta d}{h_f} \tag{3.11}$$

which dictates that the coefficient Z^* increases with the normalized delamination width d/h_f linearly with a slope of 1 at the limit of long delamination.

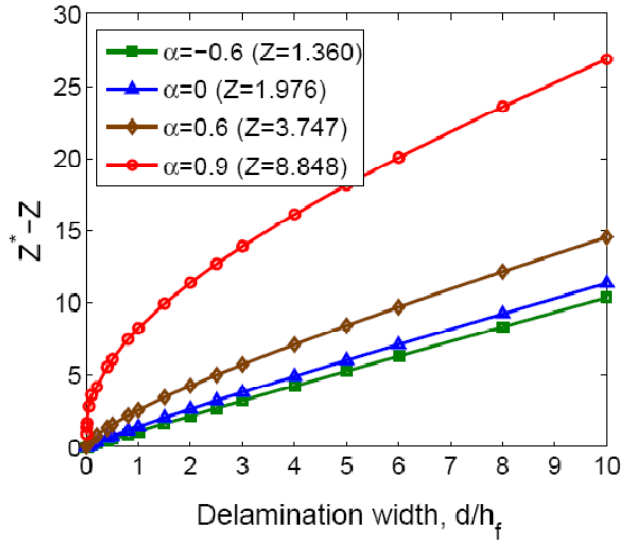

Figure 3.8: Increase of the driving force for steady-state channel cracking due to concomitant interfacial delamination.

The same finite element model as illustrated in Fig. 3.3 is employed to calculate Z^*, by integrating the opening displacement along the surface of the channel crack as Eq. (3.2). Fig. 3.8 plots the difference, $Z^* - Z$, as a function of d/h_f for different elastic mismatch parameters. For a compliant film on a relative stiff substrate ($\alpha < 0$), the

increase due to interfacial delamination is almost linear for the entire range of delamination width. For a stiff film on a relatively compliant substrate ($\alpha > 0$), however, the increase is nonlinear for short interfacial delamination and then approaches a straight line of slope 1 as predicted by Eq. (3.11). Apparently, with interfacial delamination, the driving force for channel cracking can be significantly higher than that assuming no delamination.

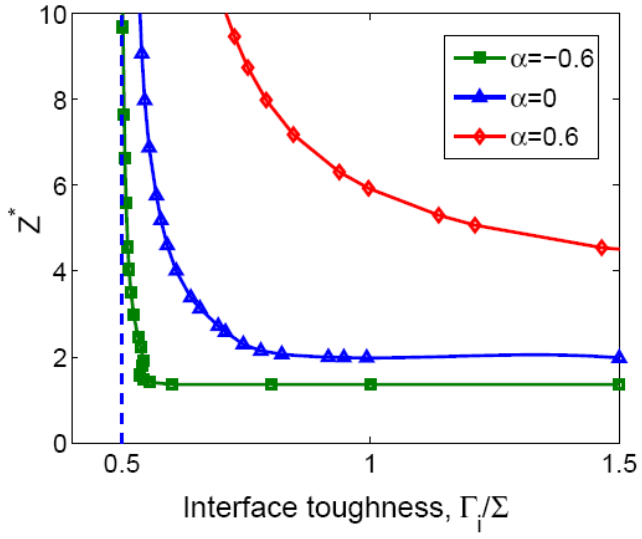

Figure 3.9: Influence of the normalized interface toughness ($\Sigma = \sigma_f^2 h_f / \overline{E}_f$) on the steady-state driving force for channel crackling.

As discussed in the previous section, the stable delamination width, d_s/h_f, can be obtained as a function of the normalized interface toughness, $\overline{\Gamma}_i$, by Eq. (3.8), as shown in Fig. 3.6. Thus, the coefficient Z^* in Eq. (3.9) may also be plotted as a function of $\overline{\Gamma}_i$, as shown in Fig. 3.9. When $\alpha > 0$, $Z^* \to Z$ as $\overline{\Gamma}_i \to \infty$, and $Z^* \to \infty$ as $\overline{\Gamma}_i \to 0.5$;

in between, Z^* increases as $\overline{\Gamma}_i$ decreases, because the interfacial delamination width increases. When $\alpha = 0$, $Z^* = Z$ as $\overline{\Gamma}_i \geq 0.9878$ (i.e., no delamination). When $0 > \alpha > -0.89$, Z^* increases from Z to infinity within a narrow window of $\overline{\Gamma}_i$, where stable delamination is predicted (Region II-B in Fig. 3.7). For $\alpha < -0.89$, either $Z^* = Z$ for no delamination or $Z^* \to \infty$ for unstable delamination. Therefore, Fig. 3.9 explicitly illustrates the influence of the interface toughness on the driving force of channel cracking in the film.

While the interfacial delamination, if occurring, relaxes the constraint on crack opening and thus enhances the fracture driving force, it also requires additional energy to fracture the interface as the channel crack advances. An energetic condition can thus be stated: if the increase in the energy release exceeds the fracture energy needed for delamination, growth of the channel crack with interfacial delamination is energetically favored; otherwise, the channel crack grows with no delamination. It can be shown that this condition is consistent with the delamination map in Fig. 3.7. Considering the interfacial fracture energy, a fracture condition for steady-state growth of a channel crack can be written as

$$G_{ss}^* \geq \Gamma_f + W_d \tag{3.12}$$

where Γ_f is the cohesive fracture toughness of the film, and W_d is the energy required to delaminate the interface accompanying per unit area growth of the channel crack. For stable delamination of width $d = d_\mathrm{s}$ at both sides of a channel crack, the delamination energy is

$$W_d = \frac{2}{h_f}\int_0^{d_s} \Gamma_i(\psi(a))da \approx 2\Gamma_i(\psi_{ss})\frac{d_s}{h_f} \tag{3.13}$$

Again, the phase angle of the interfacial crack is approximately taken as a constant independent of the crack length. When $d_s = 0$, Eq. (3.12) recovers the condition for cohesive fracture of the film, i.e., $G_{ss} \geq \Gamma_f$.

Eq. (3.12) may not be convenient to apply directly, since both sides of the equation (driving force and resistance, respectively) increase with the interfacial delamination. By moving W_d to the left hand side and noting that the stable delamination width is a function of the interface toughness, we define an effective driving force for the steady-state channel cracking:

$$G_{eff}^* = G_{ss}^* - W_d = Z_{eff}^*(\overline{\Gamma}_i, \alpha, \beta)\frac{\sigma_f^2 h_f}{\overline{E}_f} \tag{3.14}$$

with

$$Z_{eff}^* = Z^*\left(\frac{d_s}{h_f}, \alpha, \beta\right) - 2\overline{\Gamma}_i \frac{d_s}{h_f} \tag{3.15}$$

Using the effective energy release rate, the condition for the steady-state channel cracking is simply a comparison between G_{eff}^* and Γ_f, the latter being a constant independent of the interface. Fig. 3.10 plots the ratio, $Z_{eff}^*/Z(\alpha,\beta)$, as a function of $\overline{\Gamma}_i$ for different elastic mismatch parameters. At the limit of high interface toughness ($\overline{\Gamma}_i \to \infty$), $d_s \to 0$ and $Z_{eff}^* \to Z$, which recovers the case of channel cracking with no delamination. The effective driving force increases as the normalized interface toughness

deceases. Compared to Fig. 3.9, the influence of interfacial delamination on the effective driving force is reduced after considering the interfacial fracture energy.

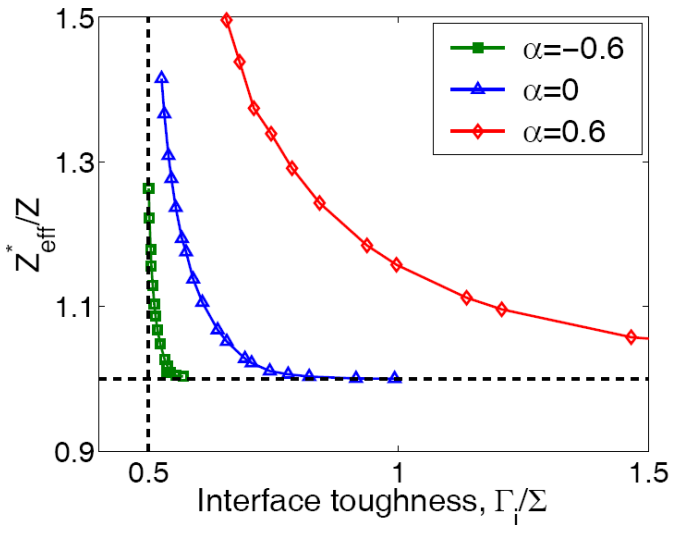

Figure 3.10: Effective driving force for steady-state channel cracking as a function of the normalized interface toughness ($\Sigma=\sigma_f^2 h_f / \bar{E}_f$).

3.2.3 Cohesive zone modeling of interfacial delaminaion

In this section, the approach of cohesive zone model is adopted to study initiation and growth of interfacial delamination from the root of a channel crack. The critical condition and the stable delamination length are determined and compared to the predictions by the LEFM approach in Section 3.2.1.

By symmetry, only half of the film/substrate structure is modeled, subject to the same boundary condition as the finite element model in Fig. 3.3. Figure 3.11 shows an example mesh near the root of a channel crack. Both the film and the substrate are

modeled by 2D quadrilateral elements (CPE8R). The interface between the film and the substrate is modeled by a layer of cohesive elements (COD2D4), defined by the bilinear traction-separation relation as illustrated in Fig. 1.9. Similar to section 2.4, the effect of mode mix is ignored. In all simulations, the initial stiffness K_0 is taken to be a constant ($K_0 h_f / \bar{E}_f = 1$), while the strength (σ_{0i}) and toughness (Γ_i) are varied.

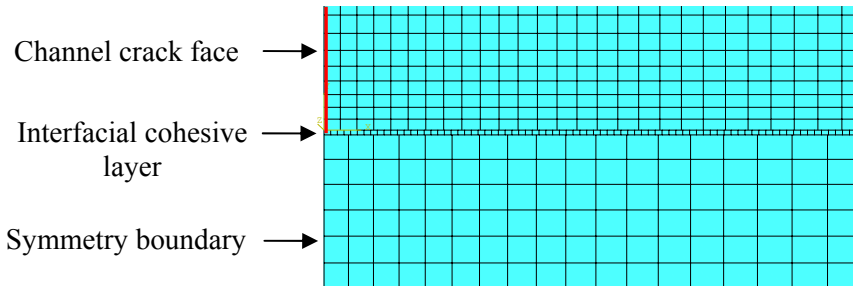

Figure 3.11: An example finite element mesh near the root of the channel crack, with a layer of cohesive elements along the interface between the film and the substrate.

First, the critical stress for initiation of interfacial delamination from the root of a channel crack is determined. As discussed in Section 3.2.1, the energy release rate for interfacial delamination has three different asymptotic behaviors at the short crack limit ($d/h_f \to 0$), depending on the elastic mismatch between the film and the substrate. When $\alpha < 0$, the energy release rate (G_d) as given in Eq. (3.3) approaches zero as $d/h_f \to 0$, regardless of the stress σ_f. By the fracture criterion in LEFM, this would predict no interfacial delamination is possible in the case of $\alpha < 0$; however, such a prediction must be taken with caution because the fracture criterion in LEFM typically

does not apply for crack initiation. When $\alpha = 0$, G_d approaches a finite value (G_{d0}) as $d/h_f \to 0$. In this case, a critical stress for initiation of interfacial delamination may be predicted by equalizing the energy release rate with the interfacial fracture toughness, namely, $G_{d0} = \Gamma_i$. As a result, the critical stress for initiation of delamination is

$$\sigma_c = \sqrt{\frac{\overline{E}_f \Gamma_i}{Z_{d0} h_f}} \tag{3.16}$$

where $Z_{d0} = Z_d(0,0,0) = 0.9878$ as determined in Section 3.2.1. For $\alpha > 0$, the energy release rate for delamination approaches infinity as $d/h_f \to 0$. Thus, the LEFM criterion would predict a zero critical stress for $\alpha > 0$; in other words, interfacial delamination always occurs as long as the stress in the film is tensile ($\sigma_f > 0$).

By the cohesive zone model as illustrated in Fig. 3.11, as the stress in the film increases, the cohesive elements at the interface deform according to the bilinear traction-separation relation. The critical stress for initiation of delamination is determined when the first cohesive element reaches the final failure (i.e., $D = 1$). Apparently, this may lead to a critical stress that depends on the size of the cohesive elements. By using a sufficiently fine mesh, it is found that the numerical result is insensitive to the element size as long as the size of the cohesive element is less than $0.01h_f$. Figure 3.12 plots the calculated critical stress, normalized by the interfacial strength σ_{0i}, as a function of a dimensionless group, $\overline{E}_f \Gamma_i / \sigma_{0i}^2 h_f$. As suggested by Parmigiani and Thouless [57], such a dimensionless group represents the ratio between the intrinsic length scale ($l = \overline{E}_f \Gamma_i / \sigma_{0i}^2$) for the cohesive zone model and the film thickness. Two different systems are considered

with $\alpha = 0$ and $\alpha = 0.6$. For each system, three different values of the interface toughness (Γ_i) are used in the numerical model, while the interfacial strength varies. It is found that the calculated critical stresses as plotted in Fig. 3.12 collapse onto a single curve for both cases, which suggests that the critical stress for initiation of interfacial delamination may be written in the form

$$\frac{\sigma_c}{\sigma_{0i}} = f\left(\frac{l}{h_f}, \alpha, \beta\right) \tag{3.17}$$

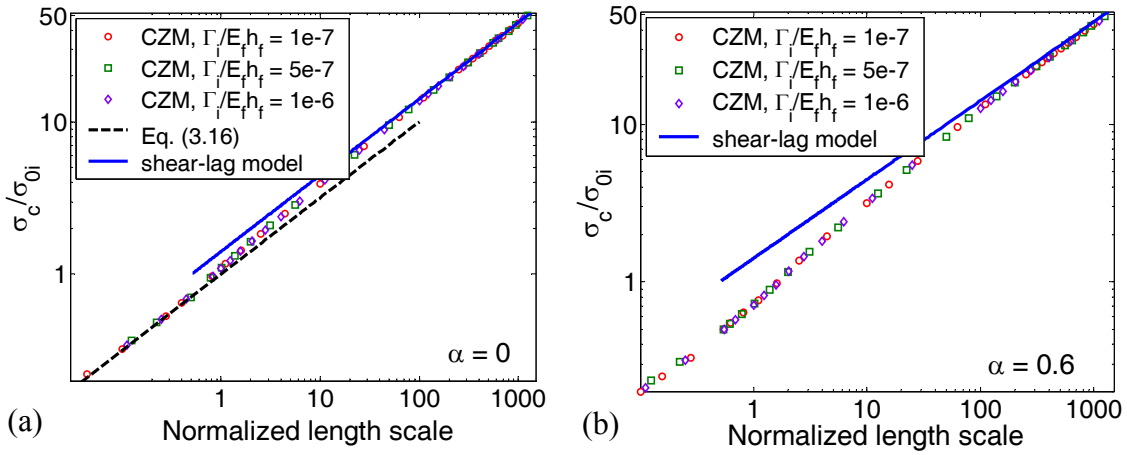

Figure 3.12: The critical stress, normalized by the interfacial strength, for initiation of delamination as a function of the normalized length scale, $l/h_f = \bar{E}_f \Gamma_i / \sigma_{0i}^2 h_f$, for different values of interface toughness: (a) $\alpha = 0$; (b) $\alpha = 0.6$.

In Fig. 3.12a, the critical stress predicted by Eq. (3.16) is plotted as a dashed line, which is a straight line in the log-log plot with slope 0.5. Evidently, the calculated critical stress by the cohesive zone model in this case ($\alpha = 0$) agrees well with the prediction by LEFM when the normalized length scale is relatively small ($l/h_f < 1$). This may be

justified as the small-scale bridging condition, for which the fracture criterion of LEFM is applicable. As l/h_f increases (large-scale bridging), however, the calculated critical stress deviates from the LEFM prediction. The cohesive zone model predicts a higher critical stress in general, and the discrepancy increases with l/h_f.

For large-scale bridging, a shear-lag model is developed to predict the critical condition for initiation of interfacial delamination from the root of a channel crack. The detailed description of the shear-lag model is given in Appendix D, where the critical stress is determined as a function of interface strength and toughness. For both $\alpha = 0$ and 0.6, the critical stress predicted by the shear-lag model is plotted as the solid blue line. Note that the substrate compliance is not considered in the shear-lag model. In the regime of large normalized length scale, $l/h_f > 100$, the excellent agreement between the results by cohesive zone modeling and shear-lag model indicates that the nucleation of delamination is predominantly dependent on the interfacial strength. Previous studies [57] on beam-like geometries showed similar results that the strength of a cracked body is only determined by the cohesive strength of the interface for very large fracture length scales. A conclusion can be drawn from Fig. 3.12 is that, cohesive zone modeling bridges the gap of fracture resistance between small-scale bridging and large-scale bridging, and provides a smooth transition between them.

Next, growth of interfacial delamination with increasing film stress is studied. As discussed in Section 3.2.1, depending on elastic mismatch, interface toughness and film stress, there may be no delamination, stable delamination and unstable delamination. The width of interfacial delamination can be predicted by Eq. (3.8), which can be rewritten as

$$\frac{d}{h_f} = f\left(\frac{\overline{E}_f \Gamma_i}{\sigma_f^2 h_f}, \alpha, \beta\right) \tag{3.18}$$

By the same cohesive zone model in Fig. 3.11, the delamination width can be determined based on the damage parameters of the cohesive elements. Fiure 3.13 plots the normalized delamination width, d/h_f, as a function of the film stress in the dimensionless form (Σ/Γ_i) for two different systems with $\alpha = 0$ and $\alpha = 0.6$. For each system, the interface toughness is taken to be a constant ($\Gamma_i/\overline{E}_f h_f = 10^{-7}$), while the interfacial strength ($\sigma_{0i}/\overline{E}_f$) varies, giving various normalized length scale (l/h_f). Superimposed on Fig. 3.13 (for both $\alpha = 0$ and 0.6) is the cohesive zone modeling result for an interface with different toughness, $\Gamma_i/\overline{E}_f h_f = 10^{-6}$, represented by the open symbols. The strength is taken to be $\sigma_{0i}/\overline{E}_f = 1.58\times10^{-4}$ so that l/h_f = 40. The collapse of the results corresponding to two different interfaces with l/h_f = 40 indicates that the effects of interfacial properties on the growth of delamination may be lumped into one parameter, l/h_f. As a result, the delamination width can be written as:

$$\frac{d}{h_f} = g\left(\frac{\overline{E}_f \Gamma_i}{\sigma_f^2 h_f}, \frac{l}{h_f}, \alpha, \beta\right) \tag{3.19}$$

which differs from Eq. (3.18) due to the additional parameter by the cohesive zone model. In Fig. 3.13, for both $\alpha = 0$ and $\alpha = 0.6$, the delamination width predicted by LEFM in Eq. (3.18) is plotted as a dashed line. The comparison shows that the interfacial delamination width by CZM approaches the prediction by LEFM as l/h_f decreases, which confirms that LEFM is applicable at small-scale bridging condition. Note that the

difference between the results by the cohesive zone model and LEFM prediction becomes smaller as the delamination width increases. This may be attributed to the fact that the relative length scale decreases as delamination width increases.

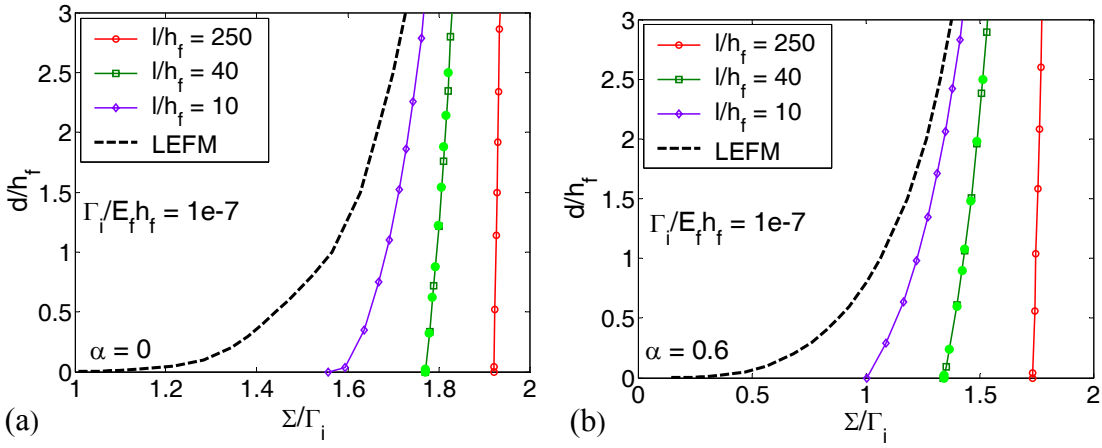

Figure 3.13: Normalized delamination width as a function of the normalized film stress Σ/Γ_i ($\Sigma=\sigma_f^2 h_f/\overline{E}_f$) for (a) $\alpha=0$; (b) $\alpha=0.6$. The open symbols are the results for the interface with $\Gamma_i/\overline{E}_f h_f=10^{-6}$ and $\sigma_{0i}/\overline{E}_f=1.58\times10^{-4}$.

3.3 Effect of substrate penetration

3.3.1 Crack penetration

In this section, crack penetrating into the substrate from the channel root (Fig. 3.1c) is analyzed. For an arbitrary penetration depth d_p, the energy release rate for substrate penetration is

$$G_p=Z_p\left(\frac{d_p}{h_f},\alpha,\beta\right)\frac{\sigma_f^2 h_f}{\overline{E}_f} \tag{3.20}$$

where Z_p is a dimensionless coefficient. A finite element model is employed to calculate Z_p as a function of the penetration depth for different elastic mismatch parameters. Fig. 3.14a is the schematic of the two-dimensional plane strain model of a steady-state channel crack with substrate penetration. By symmetry, only half of the film/substrate structure is modeled along with proper boundary conditions. Fig. 3.14b is an example mesh around the tip of the penetration crack, with a set of singular elements for the crack tip singularity. The method of J-integral is adopted to calculate the energy release rate. Similarly, we set $v_f = v_s = 1/3$ such that $\beta = \alpha/4$ for all the calculations.

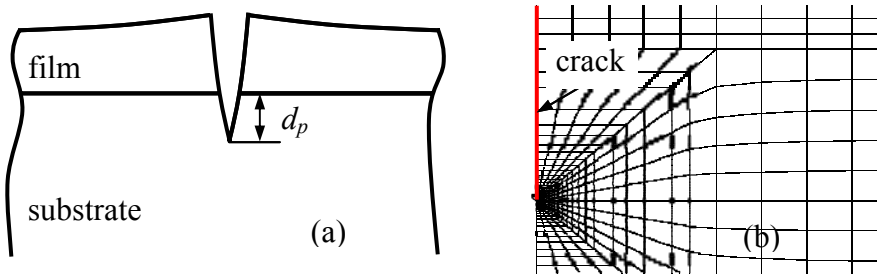

Figure 3.14: (a) Schematic of the 2D plane strain model of a steady-state channel crack with substrate penetration; (b) an example mesh around the penetration crack tip.

Fig. 3.15 is the dimensionless coefficient Z_p, determined by normalization of the numerical results according to Eq. (3.20), as a function of the normalized penetration depth, d_p/h_f, for different elastic mismatch parameters. At the limit of short penetration cracks ($d_p/h_f \to 0$), Z_p follows the same power law as Eq. (3.5) [101]. Therefore, the energy release rate for substrate penetration approaches infinity for $\alpha > 0$ but remains bounded for $\alpha \leq 0$. Together with Fig. 3.4, it is predicted that for a stiff film on a

compliant substrate ($\alpha > 0$), channel cracking of the film should inevitably be accompanied by either interfacial delamination or substrate penetration. The competition between delamination and penetration will be further discussed in the next section. With the calculated energy release rate, the penetration depth can then be obtained by equalizing the energy release rate G_p in Eq. (3.20) to the substrate toughness Γ_s, as given in Eq. (3.20), which leads to

$$\frac{d_s}{h_f} = f\left(\frac{\overline{E}_f \Gamma_s}{\sigma_f^2 h_f}, \alpha, \beta\right) \tag{3.21}$$

For different elastic mismatches, Eq. (3.21) may have different solutions, which is discussed in the following.

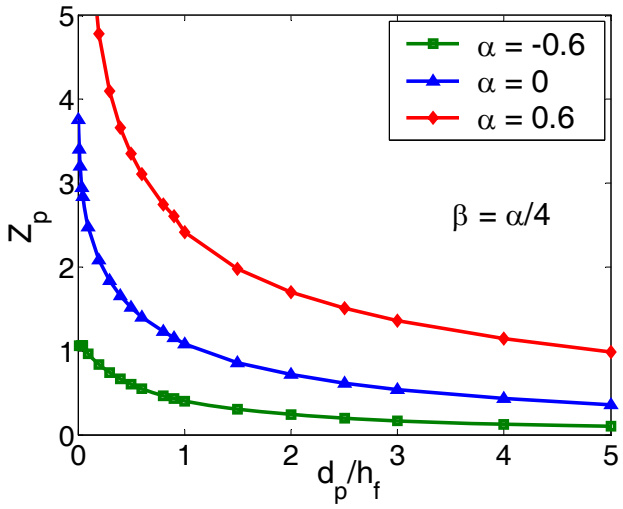

Figure 3.15: Normalized energy release rate of substrate penetration from the root of a channel crack as a function of the normalized penetration depth for different elastic mismatch parameters.

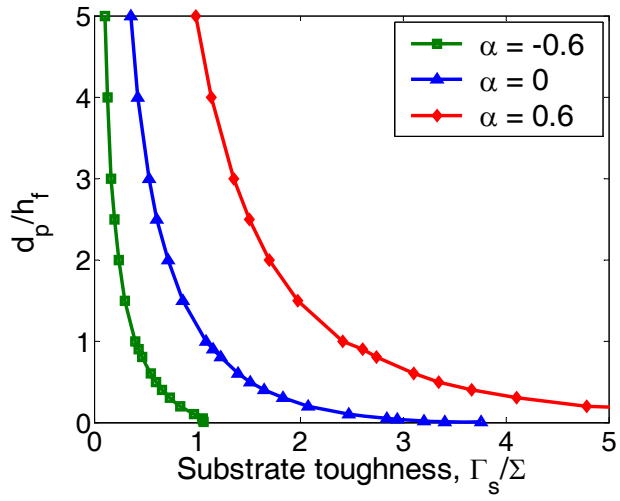

Figure 3.16: The normalized stable penetration depth as a function of the normalized substrate toughness $\overline{\Gamma}_s = \Gamma_s / \Sigma$, where $\Sigma = \sigma_f^2 h_f / \overline{E}_f$.

When $\alpha = \beta = 0$ (i.e., no elastic mismatch), the Z_p function has a maximum, $Z_p \rightarrow 3.952$ as $d_p/h_f \rightarrow 0$, and approaches zero for long cracks. Consequently, when $\overline{\Gamma}_s \geq 3.952$ (strong interface), the energy release rate for substrate penetration is always lower than the substrate toughness, and thus no penetration would occur (i.e., $d_p = 0$). For substrate toughness $\overline{\Gamma}_s < 3.952$, Eq. (3.21) has a finite solution, in which case the channel crack grows with concomitant substrate penetration of depth d_p. The normalized penetration depth is plotted as a function of the normalized substrate toughness in Fig. 3.16. When $\alpha > 0$ (i.e., a stiff film on a relatively compliant substrate), the Z_p function is unbounded as $d_p / h_f \rightarrow 0$, decreases monotonically with the depth and approaches zero as $d_p / h_f \rightarrow \infty$. This suggests that a stable substrate penetration depth can be obtained from Eq. (3.21), as presented in Fig. 3.16. When $\alpha < 0$ (i.e., a compliant film on a

relatively stiff substrate), similar to the case of interfacial delamination, the Z_p function necessary starts from zero at $d_p/h_f = 0$, and has a local maximum $Z_{p\max}$. No substrate penetration would occur if $\overline{\Gamma}_s \geq Z_{p\max}$, and stable penetration occurs if $\overline{\Gamma}_s < Z_{p\max}$. However, a critical defect size is required for the initiation of the substrate penetration, since the energy release rate approaches zero for very short cracks ($d_p/h_f \to 0$). It should be noted that the penetration crack growth may become unstable for substrates of finite thickness. The present study considers only substrates of infinite thickness.

3.3.2 Channel crack growth with substrate penetration

With a stable penetration crack into the substrate (Fig. 3.1c), the constraint on the opening of the channel crack by the substrate is relaxed. The steady-state energy release rate for channel cracking becomes:

$$G_{ss}^{**} = Z^{**}\left(\frac{d_p}{h_f}, \alpha, \beta\right)\frac{\sigma_f^2 h_f}{\overline{E}_f} \tag{3.22}$$

where the dimensionless coefficient Z^{**} depends on the depth of the substrate penetration and the elastic mismatch. Similar to the case of interfacial delamination, to account for the additional energy required to fracture the substrate, we define an effective driving force for the steady-state channel cracking with concomitant substrate penetration as

$$G_{eff}^{**} = Z_{eff}^{**}\left(\overline{\Gamma}_s, \alpha, \beta\right)\frac{\sigma_f^2 h_f}{\overline{E}_f} \tag{3.23}$$

where

$$Z_{eff}^{**} = Z^{**}\left(\frac{d_p}{h_f}, \alpha, \beta\right) - \overline{\Gamma}_s \frac{d_p}{h_f} \tag{3.24}$$

Figure 3.17 plots the ratio, $Z_{eff}^{**}/Z(\alpha,\beta)$, as a function of $\overline{\Gamma}_s$ for different elastic mismatch parameters. The effective driving force increases as the normalized substrate toughness decreases. At the limit of high substrate toughness ($\overline{\Gamma}_s \to \infty$), $d_p \to 0$ and $Z_{eff}^{**} \to Z$, which recovers the case of channel cracking with no substrate penetration.

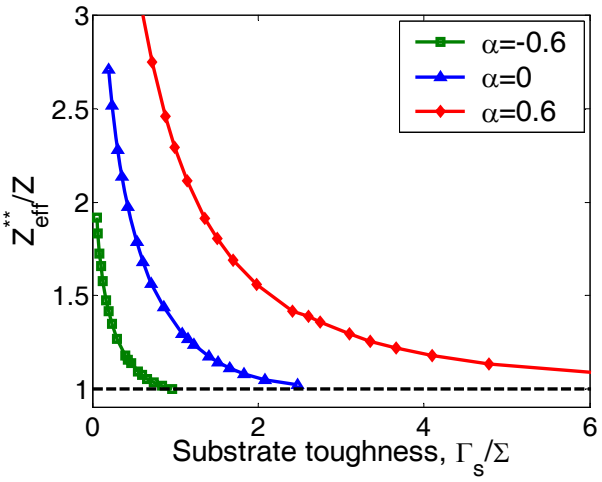

Figure 3.17: Effective driving force for steady-state channel cracking as a function of the normalized substrate toughness.

3.3.3 Cohesive zone modeling

By assuming a pre-existing penetration crack, the occurrence of substrate penetration from the channel root is discussed in Section 3.3.1. In this section, similar to the case of interfacial delamination, by the approach of cohesive zone model, both the

initiation and growth of substrate penetration are determined and compared to the predictions by the approach of LEFM. Figure 3.18 shows an example mesh near the root of a channel crack. Both the film and the substrate are modeled by 2D quadrilateral elements (CPE8R). A layer of cohesive elements (COH2D4), defined by the bilinear traction-separation relation as illustrate in Fig. 1.9, is placed straight ahead in the substrate. In all simulations, the initial stiffness K_0 is taken to be a constant ($K_0 h_f / \overline{E}_f = 1$) while the strength ($\sigma_{0s}$) and toughness ($\Gamma_s$) are varied.

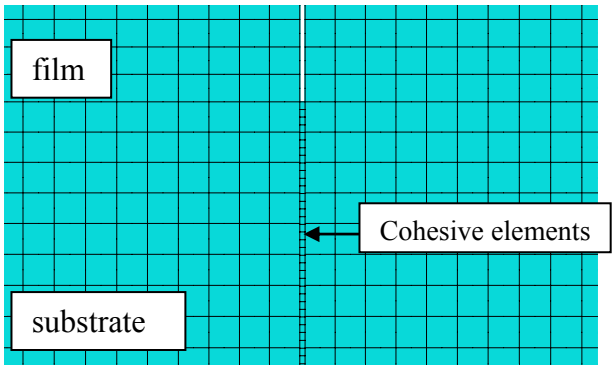

Figure 3.18: An example mesh near the root of a channel crack, with a layer of cohesive elements straight ahead in the substrate.

First, the critical stress for initiation of substrate penetration is determined. As discussed in Section 3.3.1, at the limit of short crack ($d_p / h_f \to 0$), the energy release rate for substrate penetration has three different asymptotic behaviors depending on the elastic mismatch. When $\alpha < 0$, $G_p \to 0$ as $d_p/h_f \to 0$, indicating that no substrate penetration is predicted by the fracture criterion in LEFM. When $\alpha > 0$, $G_p \to \infty$ as $d_p/h_f \to 0$, and the

LEFM criterion predicts that the channel root always penetrates into the substrate. When $\alpha = 0$, G_p approaches a finite value (G_{p0}) as $d_p/h_f \to 0$. In this case, the critical stress for initiation of substrate penetration can be predicted based on the LEFM criterion, namely, $G_{p0} = \Gamma_s$, which gives

$$\sigma_c = \sqrt{\frac{\overline{E}_f \Gamma_s}{Z_{p0} h_f}} \tag{3.25}$$

where $Z_{p0} = Z_p(0,0,0) = 3.952$ as determined in Section 3.3.1.

By the cohesive zone model as illustrated in Fig. 3.18, the critical stress for substrate penetration can be determined. Figure 3.19 plots the critical stress, normalized by substrate strength σ_{0s}, as a function of the dimensionless length scale, $\overline{E}_f \Gamma_s / \sigma_{0s}^2 h_f$. Both $\alpha = 0$ and $\alpha = 0.6$ are considered. For each elastic mismatch, three different values of substrate toughness are used in the finite element model, while the substrate strength varies. For both $\alpha = 0$ and $\alpha = 0.6$, the calculated critical stresses in Fig. 3.19 collapse onto a single curve, which indicates that the normalized critical stress for initiation of substrate penetration may be written in a similar from as Eq. (3.17),

$$\frac{\sigma_c}{\sigma_{0s}} = f\left(\frac{l}{h_f}, \alpha, \beta\right) \tag{3.26}$$

In Fig. 3.19a, the critical stress predicted by Eq. (3.25) is plotted as a dashed line, which is a straight line with slope 0.5 in the log-log plot. For $\alpha = 0$, the comparison shows that the critical stress by the cohesive zone model agrees well with the prediction by LEFM when the normalized length scale is relatively small ($l/h_f < 1$). As the ratio l/h_f increases, the calculated critical stress deviates from the LEFM prediction. The same conclusion can

be drawn for $\alpha = 0.6$ as shown in Fig 3.19b, where the result by LEFM predicts a zero critical stress.

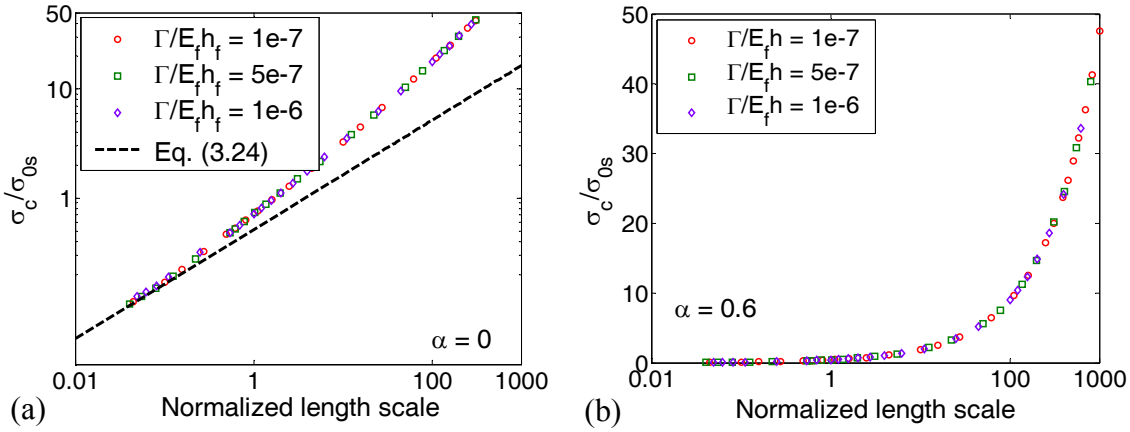

Figure 3.19: The critical stress, normalized by the substrate strength, for initiation of substrate penetration as a function of the normalized length scale, l/h_f, for three different values of substrate toughness: (a) $\alpha = 0$; (b) $\alpha = 0.6$.

Using the same cohesive zone model in Fig. 3.18, the growth of substrate penetration is studied in the following part. Figure 3.20 plots the normalized penetration depth, d_p/h_f, as a function of the normalized film stress, Σ/Γ_s, for both elastic mismatches of $\alpha = 0$ and $\alpha = 0.6$. For each elastic mismatch, similar to the case of interfacial delamination, the cohesive zone modeling results for three different normalized length scales (l/h_f) are presented, with fixed interface toughness ($\Gamma_s/\overline{E}_f h_f = 10^{-7}$). Again, the collapse of results corresponding to different cohesive parameters but same length scale indicates that the penetration depth can be expressed as

$$\frac{d_p}{h_f} = g\left(\frac{\bar{E}_f \Gamma_s}{\sigma_f^2 h_f}, \frac{l}{h_f}, \alpha, \beta\right) \tag{3.27}$$

The penetration depth by LEFM as given in Eq. (3.21) is plotted as a dashed line in Fig. 3.20. The comparison shows that the result by CZM approaches that by LEFM as the length scale decreases.

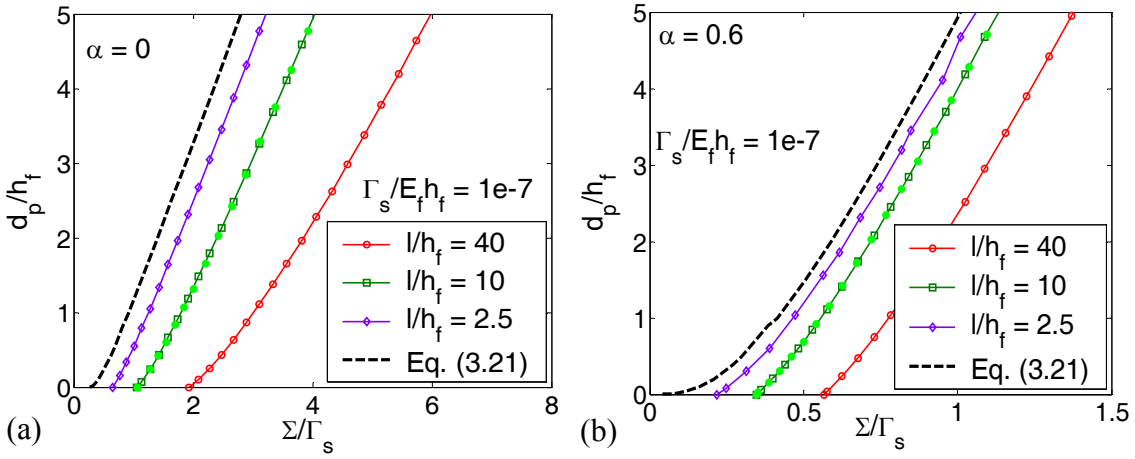

Figure 3.20: Normalized penetration depth as a function of the normalized film stress Σ/Γ_s ($\Sigma = \sigma_f^2 h_f / \bar{E}_f$) for (a) $\alpha = 0$; (b) $\alpha = 0.6$. The open symbols are the results for the interface with $\Gamma_s / \bar{E}_f h_f = 10^{-6}$ and $\sigma_{0s} / \bar{E}_f = 3.16 \times 10^{-4}$.

3.4 Competition between delamination and penetration

As discussed above, both interfacial delamination and substrate penetration can take place at the root of a channel crack, depending on the material properties of the film, the interface and the substrate. Both interfacial delamination and substrate penetration increase the driving force for channel cracking of brittle films, and both require additional

energy to fracture either the interface or the substrate. In this section, the competition between delamination and penetration is first examined based on a LEFM approach and then investigated by a cohesive zone model.

3.4.1 An energy criterion

Based on the discussions in sections 3.2.2 and 3.3.2, the competition between delamination and penetration is examined with respect to the toughness ratio between the interface and the substrate as well as the elastic mismatch. First, for $\alpha = \beta = 0$, no interfacial delamination is predicted when $\overline{\Gamma}_i \geq 0.9878$, and no substrate penetration is possible when $\overline{\Gamma}_s \geq 3.952$. The two conditions correspond to two straight lines in Fig. 3.21a (normalized driving force, Σ/Γ_s, versus the toughness ratio, Γ_i/Γ_s), dividing the plane into four regions: (I) no delamination and no penetration; (II) delamination only; (III) penetration only; (IV) both delamination and penetration are possible. In Region IV, interfacial delamination is favored when $Z_{eff}^{*} > Z_{eff}^{**}$ (Region IV-a) and substrate penetration is favored otherwise (IV-b). In Regions II and IV-a, the dashed line represents the condition $\overline{\Gamma}_i = 0.5$, beyond which interfacial delamination becomes unstable.

For a compliant substrate ($\alpha > 0$), both interfacial delamination and substrate penetration are possible over the entire plane as shown in Fig. 3.21b. By comparing the effective driving forces, interfacial delamination is favored when $Z_{eff}^{*} > Z_{eff}^{**}$ and substrate penetration is favored otherwise. The critical boundary is shown by the red line. It was found that stable interfacial delamination occurs only when $\Gamma_i/\Gamma_s < 0.5$, which is

represented by the dashed line.

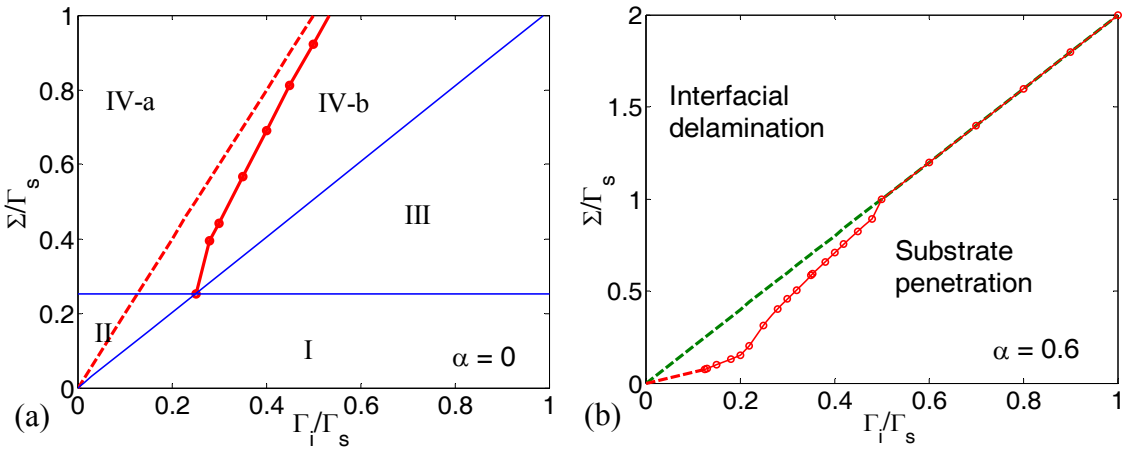

Figure 3.21: Competition between interfacial delamination and substrate penetration at the root of a channel crack: (a) $\alpha = 0$, and (b) $\alpha = 0.6$.

3.4.2 Cohesive zone modeling

To further understand the competition between interfacial delamination and substrate penetration, we developed a cohesive zone model to simulate the initiation of delamination or penetration cracks from the channel root without setting a pre-existing crack along the interface or into the substrate. Fig. 3.22 shows an example mesh near the root of a channel crack. With cohesive elements placed both along the interface and straight ahead in the substrate, a channel crack can chose to deflect into the interface or penetrate into the substrate.

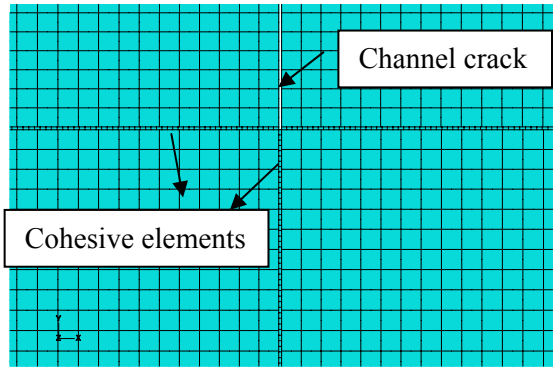

Figure 3.22: An example mesh near the root of a channel crack, with cohesive elements placed both along the interface and straight ahead in the substrate.

In this section, the system of a stiff film on a relatively compliant substrate is considered, with $\alpha = 0.6$. In all simulations, the effect of mode mix on interfacial delamination is ignored. The competition between delamination and penetration depends on the cohesive properties of the interface and the substrate, including strength and toughness: σ_{0i}, Γ_i, σ_{0s}, Γ_s. In our calculations, the initiation of either fracture mode is defined as occurring when the first cohesive element along the interface or in the substrate reaches the final failure (i.e., D=1). For constant substrate strength and toughness, $\sigma_{0s}/\bar{E}_f = 5\times10^{-4}$ and $\Gamma_s/\bar{E}_f h_f = 10^{-6}$, the competition between delamination and penetration is presented in Fig. 3.23 in the form of strength ratio, σ_{0i}/σ_{0s}, versus toughness ratio, Γ_i/Γ_s between the interface and the substrate. The dash-dot line represents the result by LEFM, which predicts that stable interfacial delamination occurs only when $\Gamma_i/\Gamma_s < 0.5$. Figure 3.23 shows that interfacial delamination is promoted by low values of both σ_{0i}/σ_{0s} and Γ_i/Γ_s, and substrate penetration is favored otherwise. On

one hand, for given interface toughness, delamination is predicted when the interfacial strength is lower than a critical value. Examples are shown as the open circles. When the interfacial strength is beyond the critical value, substrate penetration is predicted, shown as the open squres. On the other hand, for given interfacial strength, delamination is favored at lower interface toughness, and penetration is favored otherwise. Two examples of stress contour are shown in Fig. 3.24, one with interfacial delamination and the other with substrate penetration. Further studies are needed to systematically examine the effects of the cohesive parameters on the competition between fracture modes, as well as the comparison between numerical results by CZM and the predictions by LEFM.

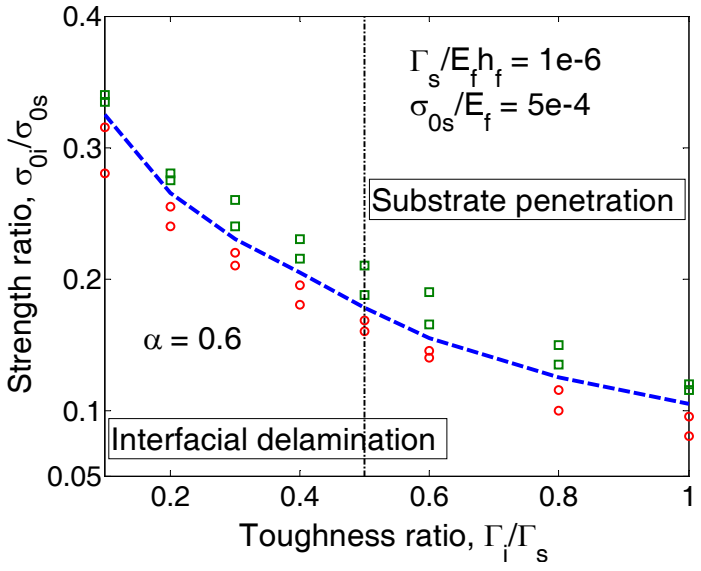

Figure 3.23: Competition between delamination and penetration for constant substrate strength and toughness, with $\sigma_{0s}/\overline{E}_f = 5\times10^{-4}$ and $\Gamma_s/\overline{E}_f h_f = 10^{-6}$.

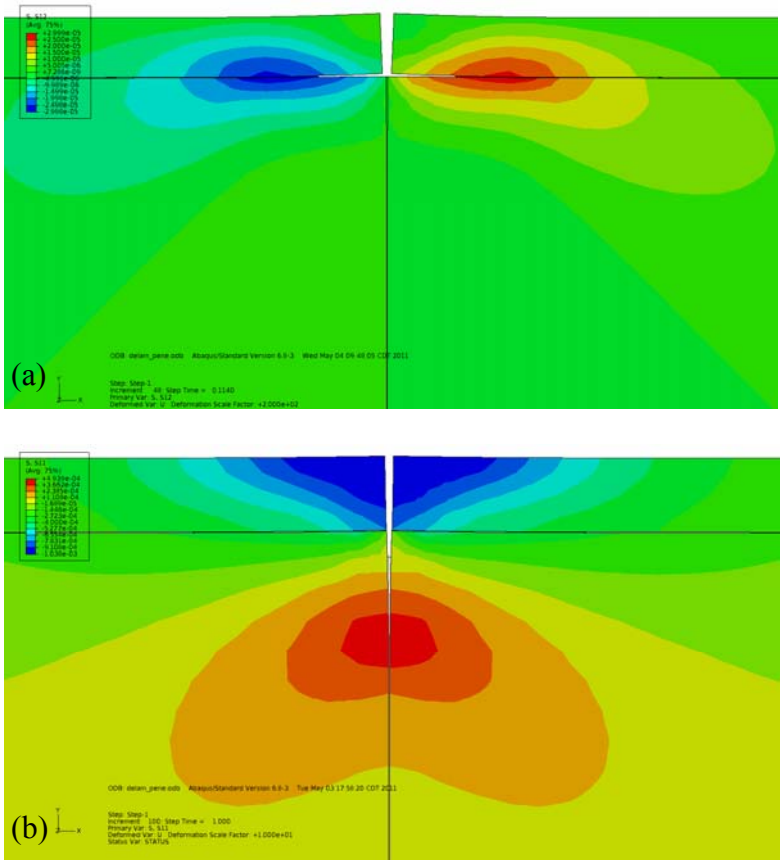

Figure 3.24: Numerical simulations by the cohesive zone modeling, showing (a) interfacial delamination, and (b) substrate penetration from the root of a channel crack.

3.5 Implications for reliability of integrated structures

The present study predicts that channel cracking in an elastic thin film on a relatively compliant substrate is always accompanied by interfacial delamination or substrate penetration. This differs from the case for an elastic film on a relatively stiff substrate, in which channel cracks may grow without interfacial delamination and substrate penetration. This difference may have important implications for reliability of

integrated structures. As an example, for interconnect structures in microelectronics, the low-k dielectrics is usually more compliant compared to the surrounding materials. Therefore the fracture of low-k dielectrics by channel cracking is typically not accompanied by interfacial delamination. However, when a more compliant buffer layer is added adjacent to the low-k film, interfacial delamination can occur concomitantly with channel cracking of the low-k film [25]. Moreover, a relatively stiff cap layer (e.g., SiN) is often deposited on top of the low-k film [104]. Channel cracking of the cap layer on low-k could be significantly enhanced by interfacial delamination. Flexible electronics is another area of applications where compliant substrates have to be used extensively along with mechanically stiffer films for the functional devices and interconnects [3, 4]. Here, interfacial delamination could play a critical role in the reliability assessment. As shown in a previous study by Li and Suo [105], the stretchability of metal thin-film interconnects on a compliant substrate can be dramatically reduced by interfacial delamination. For brittle thin films on compliant substrates, as considered in the present study, interfacial delamination has a similar effect on the fracture and thus deformability of the devices.

3.6 Summary

In summary, this chapter considers concomitant interfacial delamination/substrate cracking and channel cracking in elastic thin films. Using a set of finite element models, the effects of interfacial delamination and substrate penetration on channel cracking of brittle thin films are analyzed. It is found that, depending on the elastic mismatch and the

toughness of interface and substrate, a channel crack may grow with interfacial delamination and/or substrate cracking. An effective energy release rate for the steady-state growth of a channel crack is defined to account for the influence of interfacial delamination/substrate cracking on both the driving force and the resistance, which can be significantly higher than the energy release rate assuming no interfacial delamination or substrate penetration. By comparing the effective energy release rate, the competition between the two fracture modes is discussed. Cohesive zone modeling is then employed to simulate the nucleation and growth of delamination and penetration from the root of a channel. By comparing the results from the approaches of LEFM and CZM, the characteristic fracture resistance from small-scale bridging to large-scale bridging is identified.

Chapter 4

Extraction of interfacial traction-separation relations

In Chapters 2 and 3, by using cohesive zone models, both nucleation and growth of interfacial delamination have been simulated, without assuming a pre-existing crack. The competition between crack paths has also been examined. Compared to other modeling approaches, the cohesive zone model has its unique advantages. In particular, this approach is capable of modeling interface fracture over a wide range of length scales, which is important for the mechanical reliability analysis of integrated systems [1, 2]. However, the interfacial traction-separation relations are required as input for cohesive zone models. Thus, the major obstacle to the application of the cohesive zone modeling approach lies in the difficulty of obtaining interfacial parameters associated with traction-separation relations (including both strength and toughness) from experiments. In addition to the global measurements that are commonly used for determination of the interface toughness (e.g., four-point bend tests), more detailed local measurements are required to determine the nonlinear traction-separation relation for a cohesive interface. By combing finite element modeling with experimental measurements, the objective of this chapter is to develop a unified approach to characterize interfacial properties over a wide range of length scales.

4.1 Iterative and direct methods

Experimental measurements of traction-separation relations are generally based

on either indirect or direct method. The indirect method uses an iterative procedure based on finite element simulations [65, 106-108]. For this method, various cohesive parameters are presumed in finite element models, and the traction-separation relation that gives the best matches between numerical predictions and experimental measurements is selected as the true one. For example, fracture characteristics of an Al_2O_3/Al composite are obtained by comparing the measurements of resistance curves and work of rupture with the predictions by a micromechanical model considering the effects of crack bridging by the Al reinforcements [106]. By means of compact-tension specimens [108], the traction-separation law is extracted by fitting the numerical load-displacement curve to the experimental data. The interfacial traction-separation relations are determined by comparing the finite element predictions of normal crack opening displacements with those measured by experiments [65, 107, 109].

For direct method, the traction-separation relation is determined directly from experiments instead of performing iterative finite element simulations and comparisons. One approach is proposed [110-112] to perform tensile tests on circumferentially notched specimens, from which the tractions as a function of the locally measured separations can be determined. However, the traction across the width of the specimen must be uniform, which is usually difficult to achieve. Another direct method is based on J-integral, which is originally proposed [113] to determine the traction-separation relation for concrete. By simultaneously recording the J-integral and the crack tip opening displacement, the traction-separation relation can be derived. The J-integral technique has been applied to different materials including concrete [114], fiber reinforced concrete [115-117] and

rocks [114, 118], and for cementitious composites [119]. More recently, this approach has been successfully employed in extraction of the traction-separation relations for adhesive bonds [120], fiber-reinforced composites [66] and polyurea/steel sandwich interface [121]. Based on the J-integral technique, a hybrid approach combining numerical simulations with experimental measurements is developed in this chapter to determine the nonlinear traction-separation relation for cohesive zone modeling of a bimaterial interface.

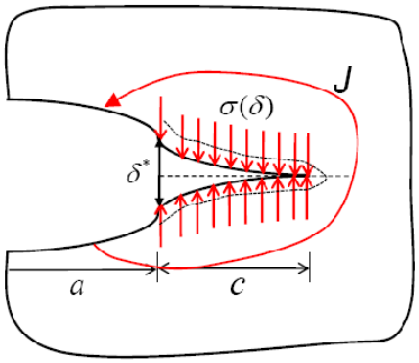

Figure 4.1: Determination of traction-separation relation from J-integral.

As discussed in Chapter 1, evaluating the J-integral locally over a contour around the crack tip and enclosing the entire cohesive zone, as shown in Fig. 4.1, gives [63]

$$J = J_{tip} + \int_0^{\delta^*} \sigma(\delta) d\delta \tag{4.1}$$

where J_{tip} is the J-integral calculated over a contour close to the crack tip, δ^* is the crack tip opening displacement, δ is the crack opening displacement in the cohesive zone, and $\sigma(\delta)$ is the associated traction along the crack faces within the cohesive zone.

Consequently, if both δ^* and the J-integral can be measured accurately, the interfacial traction-separation relation can be determined by the following equation[66, 122]

$$\sigma\left(\delta^*\right) = \frac{dJ}{d\delta^*} \tag{4.2}$$

It should be noted that although Eq. (4.2) is simple, there could be some uncertainties in implementing it experimentally. The effects of J-integral calculation and the accuracy of the crack tip location on the success of such measurements are examined in sections 4.3 and 4.4 by both analytical and finite element models. The examination provides a guide to improve key measurements for experiments to successfully extract the traction-separation relation of an interface. In collaboration with Dr. Liechti's group, a mode-I fracture experiment of wedge-loaded double cantilever beam (DCB) test is conducted and simulated.

4.2 Wedge-loaded double cantilever beam (DCB) tests

4.2.1 Experimental setup

The mode-I experiment is conducted on the DCB specimens, using a screw-driven loading device, which could be used for both inserting and withdrawing a wedge. Figure 4.2 is the schematic of the wedge-loaded DCB test. The preparation of the sandwich Si/epoxy/Si specimens is introduced in details in [123]. For the DCB test, the J-integral is determined through measurements of the crack length *a*, and the crack tip opening displacement is measured by the technique of infrared crack opening interferometry (IR-COI) [124].

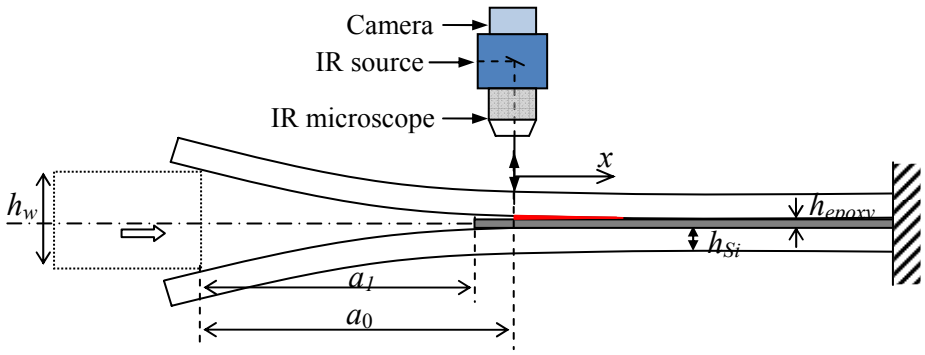

Figure 4.2: Schematic of a wedge-loaded double cantilever beam test.

For the specimen in Fig. 4.2, two Si beams are bonded using epoxy. The thickness of each Si beam is h_{Si}, the thickness of the wedge is h_{w}, and the thickness of the epoxy is h_{epoxy}. The crack length, denoted by a, is defined as the distance between the leading edge of the wedge and the crack tip. An initial crack a_0 is introduced, with length a_1 along the interface between the two Si beams and length $a_0 - a_1$ along the interface between the epoxy layer and the top Si beam. The wedge is inserted between the Si beams to open the initial interfacial crack. During the test, the distance that the wedge is inserted (u_w) is controlled by a micrometer screw, and a microscope is used to determine the positions of the crack front and the leading edge of the wedge. This allows the new crack length at each increment to be determined as $a = a_0 + \Delta a - u_w$, where Δa is the length of crack growth. With the measured crack length, the J-integral can be obtained by calculating the energy release rate using the simple beam model, i.e.,

$$J = G = \frac{3E_{Si}h_{Si}^3\left(h_w - h_{epoxy}\right)^2}{16a^4} \tag{4.3}$$

where E_{Si} is the Young's modulus of Si. Eq. (4.3) suggests that the interface toughness can be determined by measuring the steady-state crack length (a_{ss}). Eq. (4.3), however, may not be accurate for four reasons: (1) it does not account for the end rotation at the crack tip; (2) it neglects shear deformation in the beams; (3) it assumes the small-scale bridging at the interface; (4) it neglects the deformation of the epoxy layer. The accuracy of the J-integral calculations by Eq. (4.3) is further discussed in Sections 4.3 and 4.4.

In addition to the J-integral, local crack opening displacements are required to experimentally determine the traction-separation relation. For mode-I tests, only normal crack opening displacements (NCOD), δ_{n}, are needed. As the displacement of the wedge is controlled, the NCODs near the crack tip is measured by infrared crack-opening interferometry (IC-COI) [124], which is an extremely useful technique for measuring NCOD, tracking changes in crack front geometry and observing crack closures. IR-COI uses an infrared beam and its interaction with the crack faces to measure NOCD [124]: the infrared beams that are reflected from the two crack faces interact with each other and form interference fringes due to their optical path difference, and the NCOD can then be obtained by reading the fringes. A detailed description of determination of NCOD using interference fringes can be found in [123], together with the validity of this technique through two experiments. For the wedge-loaded DCB tests, the determination of NCODs through IR-COI is performed using an infrared microscope, thereby making use of the transparency of silicon to IR. The microscope is fitted with an internal beam splitter and

an IR filter to provide the normal incident beam, since the COI configuration used here requires the input IR beam to be normal to the crack faces. During the loading procedure, the digital camera focused upon the crack front captures the movement of fringes, and the images captured are then processed by image processing software. The resolution of IR-COI is 260nm, and it can be improved by interpolation between the dark and bright fringes.

4.2.2 Experimental results

A series of wedge-loaded DCB tests are performed, and the results presented in the present study are for one sample, for which the geometric parameters of the specimen are h_{Si} = 0.28mm, h_w = 0.085mm, h_{epoxy} = 0.025mm, a_0 = 13mm, a_1 = 10mm. The elastic properties for Si and epoxy are E_{Si} = 168GPa, ν_{Si} = 0.22, E_{epoxy} = 2.03GPa, ν_{epoxy} = 0.33. Figure 4.3 is the measured crack length as a function of the wedge displacement. First the crack front does not move and thus the crack length decreases linearly with the wedge displacement ($a = a_0 - u_w$). At a critical wedge displacement, the crack front suddenly jumped forward, giving a set of crack length data for the same wedge displacement. Further increasing the wedge displacement, the crack front moves almost simultaneously, giving a constant crack length and indicating a steady state. The steady-state crack length a_{ss} is thus measured as a critical quantity for determining the interfacial properties. Figure 4.4 shows the measured NCODs at different crack lengths, which are to be compared with modeling and simulations.

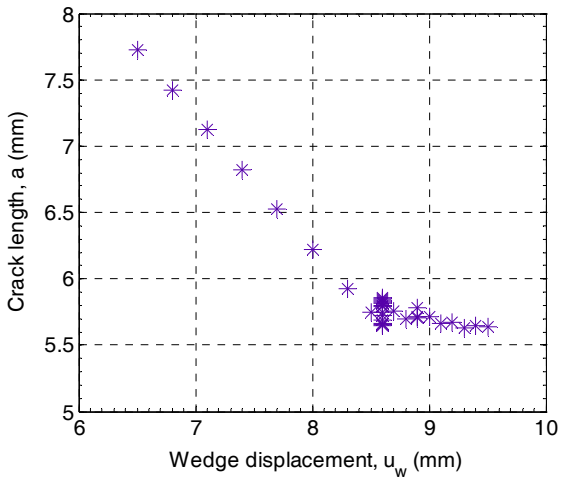

Figure 4.3: Measured crack length as a function of the wedge displacement.

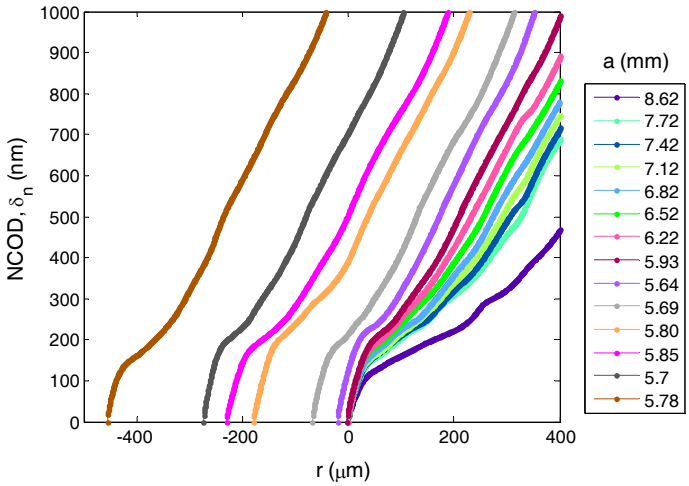

Figure 4.4: Measured normal crack opening displacements (NCODs) for different crack lengths.

4.3 An analytical model

To study the effects of experimental measurements on the accuracy of extraction of traction-separation relations, in this section, we develop an analytical solution based on

an approximate model for the wedge-loaded DCB specimen. The epoxy layer is neglected in the analytical model considering that it is much thinner than the Si beam. By symmetry, only the top beam is considered (Fig. 4.5). The deflection of the beam is governed by the simple beam equation, namely

$$EI\,\frac{d^4v}{dx^4} = -q \tag{4.4}$$

where EI is the flexural rigidity of the beam with $I = bh^3/12$ for a beam of thickness h and width b, E is Young's modulus of the material, v as a function of x is the deflection, and q is the intensity of the distributed load (force per unit length) acting on the beam. As shown in Fig. 4.5, for a DCB specimen with a crack of length a (measured from the loading point to the crack tip), the interfacial load intensity can be specified in two regions. First, for $x < 0$, where the interface has been fully fractured, we have zero load intensity (q = 0). Ahead of the crack tip ($x > 0$), a cohesive zone develops as the crack opens up. At each point along the interface, the opening displacement (δ) is related to the opening stress (σ) by the specified traction-separation relation, and consequently the load intensity depends on the traction-separation relation of the interface, i.e., $q = b\sigma(\delta)$, noting that $\delta = 2v$ for the symmetric DCB. In this section, we solve this problem analytically using the bilinear traction-separation relation as shown in Fig. 1.9. Since the DCB specimen is symmetrically loaded, only the mode-I parameters are needed in this analytical model.

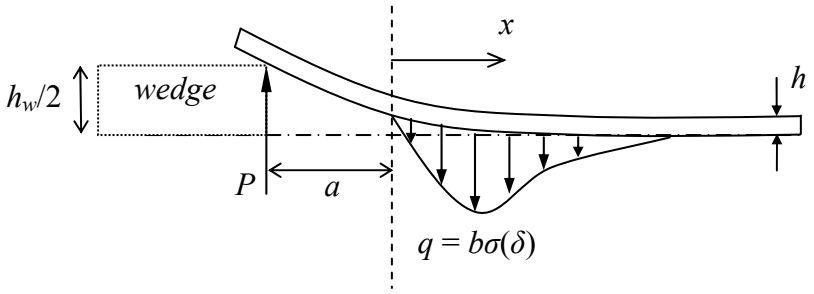

Figure 4.5: Schematic of the upper beam in a wedge-loaded DCB specimen.

For the bilinear traction-separation relation, the problem can be solved in two steps. First, starting from a virgin DCB specimen with an initially closed crack, as the crack opens up, the interface opens elastically until the crack tip opening displacement (CTOD) reaches the critical value (δ_0) for damage initiation. The CTOD is simply the deflection at $x = 0$, i.e., $\delta^* = 2v(0)$. Next, when $\delta^* > \delta_0$, a damage zone develops ahead of the crack tip, until the CTOD reaches the critical value (δ_c) for fracture. For the wedge-loaded DCB specimen, the crack length a first decreases as the wedge is pushed towards the crack tip, until the CTOD reaches δ_c. Subsequently, pushing the wedge further, the crack advances in a steady state with a constant crack length (a_{ss}).

Solving Eq. (4.4) for $-a < x < 0$ along with the boundary conditions, we obtain the profile for the NCOD:

$$\delta(x) = \delta^* - \theta^* x + \frac{Pa^3}{3EI}\left[3\left(\frac{x}{a}\right)^2 + \left(\frac{x}{a}\right)^3\right] \tag{4.5}$$

where δ^* is the CTOD and θ^* the crack-tip opening angle (CTOA). The opening displacement at the loading point ($x = -a$) is thus

$$\Delta = \frac{2Pa^3}{3EI} + \theta^* a + \delta^* \tag{4.6}$$

We note that, while Eqs. (4.5) and (4.6) are independent of any specific traction-separation law for the interface, the CTOD (δ^*) and CTOA (θ^*), both varying with the load (P) and the crack length (a), depend on the interfacial properties.

4.3.1 Elastic opening of the interface

When $\delta^* < \delta_0$, the load intensity ahead of the crack tip (x >0) is simply, $q = 2bK_0v$, by the bilinear traction-separation law. The beam equation in Eq. (4.4) becomes

$$\frac{d^4v}{dx^4} + \frac{2K_0b}{EI}v = 0 \tag{4.7}$$

Assume that the DCB specimen is infinitely long, with zero deflection and rotation at infinity ($x \to \infty$). Along with the boundary conditions at the crack tip (x = 0), we solve Eq. (4.7) and obtain that, for x >0, the NCOD is

$$\delta(x) = \delta^* e^{-\lambda x}\left(\cos(\lambda x) + \left(1 - \frac{\theta^*}{\lambda\delta^*}\right)\sin(\lambda x)\right) \tag{4.8}$$

where $\lambda = \left(\frac{K_0 b}{2EI}\right)^{\frac{1}{4}}$.

To find the CTOD and CTOA, we apply the continuity conditions for the bending moment and shear force at x =0, which leads to

$$-\lambda^2\delta^*\left(1 - \frac{\theta^*}{\lambda\delta^*}\right) = \frac{Pa}{EI} \tag{4.9}$$

$$\lambda^3\delta^*\left(2-\frac{\theta^*}{\lambda\delta^*}\right)=\frac{P}{EI} \tag{4.10}$$

Solving Eqs. (4.9) and (4.10) simultaneously, we obtain that

$$\delta^*=\frac{P}{\lambda^3 EI}(\lambda a+1) \tag{4.11}$$

$$\theta^*=\frac{P}{\lambda^2 EI}(2\lambda a+1) \tag{4.12}$$

Inserting Eqs. (4.11) and (4.12) into Eq. (4.6), we obtain the opening displacement at the loading point as

$$\Delta=\frac{2Pa^3}{3EI}\left(1+\frac{3}{\lambda a}+\frac{3}{(\lambda a)^2}+\frac{3}{2(\lambda a)^3}\right) \tag{4.13}$$

The corresponding energy release rate is then obtained as follows. First, the elastic strain energy equals the work done by the load P, namely

$$W(a)=\frac{1}{2}P\Delta=\frac{P^2a^3}{3EI}\left(1+\frac{3}{\lambda a}+\frac{3}{(\lambda a)^2}+\frac{3}{2(\lambda a)^3}\right) \tag{4.14}$$

The energy release rate is thus

$$G=\frac{1}{b}\frac{dW}{da}=\frac{12P^2a^2}{Eb^2h^3}\left(1+\frac{1}{\lambda a}\right)^2 \tag{4.15}$$

In terms of the loading displacement (or the wedge thickness), the energy release is

$$G=\frac{3Eh^3\Delta^2}{16a^4}\left(\frac{1+\frac{1}{\lambda a}}{1+\frac{3}{\lambda a}+\frac{3}{(\lambda a)^2}+\frac{3}{2(\lambda a)^3}}\right)^2 \tag{4.16}$$

Thus, only when $\lambda a = \frac{a}{h}\left(\frac{6K_0 h}{E}\right)^{\frac{1}{4}} >> 1$, we have approximately

$$G \approx \frac{12P^2a^2}{Eb^2h^3} \approx \frac{3Eh^3\Delta^2}{16a^4} \tag{4.17}$$

which recovers the simple result for DCB assuming perfectly bonded interface (i.e., $\delta^* = 0$ and $\theta^* = 0$). Similar solutions for the energy release rate in Eqs. (4.15) and (4.16) were obtained previously using elastic foundation models [125-128].

It can be shown that

$$\frac{dG}{d\delta^*} = \frac{dG}{dP}\frac{dP}{d\delta^*} = K_0\delta^* \tag{4.18}$$

which recovers the elastic part of the bilinear traction-separation law ($\delta^* < \delta_0$). It is thus possible to determine the initial stiffness of the interface by measuring the CTOD.

The critical load for damage initiation at the crack tip is obtained by setting $\delta^* = \delta_0$, which gives that

$$P_0(a) = \frac{\lambda^3 EI\delta_0}{\lambda a + 1} \tag{4.19a}$$

$$\Delta_0(a) = \frac{2\lambda^3 a^3\delta_0}{3(\lambda a+1)}\left(1 + \frac{3}{\lambda a} + \frac{3}{(\lambda a)^2} + \frac{3}{2(\lambda a)^3}\right) \tag{4.19b}$$

Correspondingly, the critical energy release rate is

$$G_0 = \frac{\lambda^4 Eh^3\delta_0^2}{12} = \frac{1}{2}K_0\delta_0^2 = \frac{1}{2}\sigma_0\delta_0 \tag{4.20}$$

which depends on the interfacial strength and stiffness, independent of the interfacial toughness or the initial crack length. On the other hand, the critical load (P_0 or Δ_0)

depends on the crack length.

4.3.2 Crack opening with a damage zone

Next, when $\delta^* > \delta_0$, the traction along the interface can be specified in two parts. Assume a damage zone of length c ahead of the crack tip. Within the damage zone ($0 < x < c$), where the damage variable D as defined in Eq. (1.10) varies between 0 and 1, the load intensity varies accordingly, i.e., $q = 2bK_0(1-D)$. Beyond the damage zone ($x >$ c), the interface is undamaged ($D = 0$) and thus $q = 2bK_0v$. For the first part ($0 < x <$ c), the beam equation becomes

$$\frac{d^4v}{dx^4} + \frac{K_0 b}{EI}\frac{\delta_0}{\delta_c - \delta_0}\left(\delta_c - 2v\right) = 0 \tag{4.21}$$

Solving Eq. (4.21), we obtain that, for $0 < x <$ c,

$$v(x) = B_1\cosh(\mu x) + B_2\sinh(\mu x) + B_3\cos(\mu x) + B_4\sin(\mu x) + \frac{\delta_c}{2} \tag{4.22}$$

where $\mu = \left(\frac{2K_0 b\delta_0}{EI(\delta_c - \delta_0)}\right)^{\frac{1}{4}}$.

The NCOD for $x < 0$ is given in Eq. (4.5). At the crack tip ($x = 0$), we have the continuity conditions:

$$v(x = 0^-) = v(x = 0^+),\ \left.\frac{dv}{dx}\right|_{x=0^-} = \left.\frac{dv}{dx}\right|_{x=0^+},\ \left.\frac{d^2v}{dx^2}\right|_{x=0^-} = \left.\frac{d^2v}{dx^2}\right|_{x=0^+},\ \text{and}\ \left.\frac{d^3v}{dx^3}\right|_{x=0^-} = \left.\frac{d^3v}{dx^3}\right|_{x=0^+} \tag{4.23}$$

With Eqs. (4.22) and (4.5), we obtain that

$$B_1 + B_3 + \frac{\delta_c}{2} = \frac{\delta^*}{2} \tag{4.24a}$$

$$\mu B_2 + \mu B_4 = -\frac{\theta^*}{2} \tag{4.24b}$$

$$B_1 - B_3 = \frac{1}{\mu^2 a^2}\frac{Pa^3}{EI} \tag{4.24c}$$

$$B_2 - B_4 = \frac{1}{\mu^3 a^3}\frac{Pa^3}{EI} \tag{4.24d}$$

Solving the above equations, we obtain that

$$\begin{pmatrix} B_1 \\ B_2 \\ B_3 \\ B_4 \end{pmatrix} = \frac{1}{2}\begin{bmatrix} 1 & 0 & 1 & 0 \\ 0 & 1 & 0 & 1 \\ 1 & 0 & -1 & 0 \\ 0 & 1 & 0 & -1 \end{bmatrix}\begin{pmatrix} \frac{\delta^* - \delta_c}{2} \\ -\frac{\theta^*}{2\mu} \\ \frac{1}{\mu^2 a^2}\frac{Pa^3}{EI} \\ \frac{1}{\mu^3 a^3}\frac{Pa^3}{EI} \end{pmatrix} \tag{4.25}$$

The deflection in Eq. (4.22) is thus fully determined once the CTOD and CTOA are determined.

For $x > c$, where the interface opens elastically, we solve Eq. (4.7) and obtain that,

$$v(x) = \frac{\delta_0}{2} e^{-\lambda(x-c)}\left(\cos\lambda(x-c) + \left(1 - \frac{\theta_0}{\lambda\delta_0}\right)\sin\lambda(x-c)\right) \tag{4.26}$$

where θ_0 is the opening angle of the interface at $x = c$ and the NCOD at $x = c$ has been set to be δ_0 according to the bilinear traction-separation law.

The continuity conditions at $x = c$ requires that

$$v(x = c^-) = v(x = c^+),\ \left.\frac{dv}{dx}\right|_{x=c^-} = \left.\frac{dv}{dx}\right|_{x=c^+},\ \left.\frac{d^2v}{dx^2}\right|_{x=c^-} = \left.\frac{d^2v}{dx^2}\right|_{x=c^+},\ \text{and}\ \left.\frac{d^3v}{dx^3}\right|_{x=c^-} = \left.\frac{d^3v}{dx^3}\right|_{x=c^+} \tag{4.27}$$

With Eqs. (4.22) and (4.26), the continuity conditions become

$$B_1\cosh(\mu c)+B_2\sinh(\mu c)+B_3\cos(\mu c)+B_4\sin(\mu c)+\frac{\delta_c}{2}=\frac{\delta_0}{2} \tag{4.28a}$$

$$\mu B_1\sinh(\mu c)+\mu B_2\cosh(\mu c)-\mu B_3\sin(\mu c)+\mu B_4\cos(\mu c)=-\frac{\theta_0}{2} \tag{4.28b}$$

$$\mu^2 B_1\cosh(\mu c)+\mu^2 B_2\sinh(\mu c)-\mu^2 B_3\cos(\mu c)-\mu^2 B_4\sin(\mu c)=-\lambda^2\delta_0\left(1-\frac{\theta_0}{\lambda\delta_0}\right) \tag{4.28c}$$

$$\mu^3 B_1\sinh(\mu c)+\mu^3 B_2\cosh(\mu c)+\mu^3 B_3\sin(\mu c)-\mu^3 B_4\cos(\mu c)=\lambda^3\delta_0\left(2-\frac{\theta_0}{\lambda\delta_0}\right) \tag{4.28d}$$

Inserting Eq. (4.25) into Eq. (4.28), we obtain that

$$\begin{bmatrix}\Phi_{11} & \Phi_{12} & \Phi_{13} & 0\\ \Phi_{21} & \Phi_{22} & \Phi_{23} & 1/2\\ \Phi_{31} & \Phi_{32} & \Phi_{33} & -\lambda/\mu\\ \Phi_{41} & \Phi_{42} & \Phi_{43} & \lambda^2/\mu^2\end{bmatrix}\begin{pmatrix}\frac{Pa^3}{EI}\\ \delta^*-\delta_c\\ \theta^*/\mu\\ \theta_0/\mu\end{pmatrix}=\begin{pmatrix}\frac{\delta_0-\delta_c}{2}\\ 0\\ -\lambda^2\delta_0/\mu^2\\ 2\lambda^3\delta_0/\mu^3\end{pmatrix} \tag{4.29}$$

where

$$\begin{bmatrix}\Phi_{11} & \Phi_{12} & \Phi_{13} & \Phi_{14}\\ \Phi_{21} & \Phi_{22} & \Phi_{23} & \Phi_{24}\\ \Phi_{31} & \Phi_{32} & \Phi_{33} & \Phi_{34}\\ \Phi_{41} & \Phi_{42} & \Phi_{43} & \Phi_{44}\end{bmatrix}=\frac{1}{2}\begin{bmatrix}\cosh(\mu c) & \sinh(\mu c) & \cos(\mu c) & \sin(\mu c)\\ \sinh(\mu c) & \cosh(\mu c) & -\sin(\mu c) & \cos(\mu c)\\ \cosh(\mu c) & \sinh(\mu c) & -\cos(\mu c) & -\sin(\mu c)\\ \sinh(\mu c) & \cosh(\mu c) & \sin(\mu c) & -\cos(\mu c)\end{bmatrix}\begin{bmatrix}1 & 0 & 1 & 0\\ 0 & 1 & 0 & 1\\ 1 & 0 & -1 & 0\\ 0 & 1 & 0 & -1\end{bmatrix}\begin{bmatrix}0 & \frac{1}{2} & 0\\ 0 & 0 & -\frac{1}{2}\\ \frac{1}{\mu^2 a^2} & 0 & 0\\ \frac{1}{\mu^3 a^3} & 0 & 0\end{bmatrix} \tag{4.30}$$

Given the material properties of the elastic beam and the interface, we can solve Eq. (4.29) by linear algebra to obtain four unknown quantities: $\frac{Pa^3}{EI}$, $\delta^*-\delta_c$, θ^*/μ, and θ_0/μ for a specific crack length a and damage zone size c. For a particular wedge thickness (h_w), the damage zone size is determined iteratively by setting

$\Delta(a,c)=\frac{2Pa^3}{3EI}+\theta^* a+\delta^*=h_w$. Since the epoxy is neglected in the analytical model, h_w should be taken as the effective thickness, defined as the net difference between the thickness of the wedge and the epoxy layer, i.e. $h_w = h_{Si} - h_{epoxy} = 0.06$mm. For the present study, we have used $K_0 = 10^{15}$N/m^3, $\sigma_0 = 1.8\times10^{17}$N/m^2, and $\Gamma = 1.8$J/m^2.

Fig. 4.6a plots the opening displacement (Δ) for different crack lengths, with dashed line corresponding to h_w, and Fig. 4.6b plots the damage zone size (c) as a function of the crack length (a). The results show that the interface opens elastically before the wedge is pushed in when the initial crack $a_0 > 13$mm, the interface is partially damaged for relatively small a_0, and fully damaged for $a_0 < 5.75$mm. The damage zone size increases nonlinearly with the decrease of crack length until crack growth, and then remains a constant as the crack grows in a steady state.

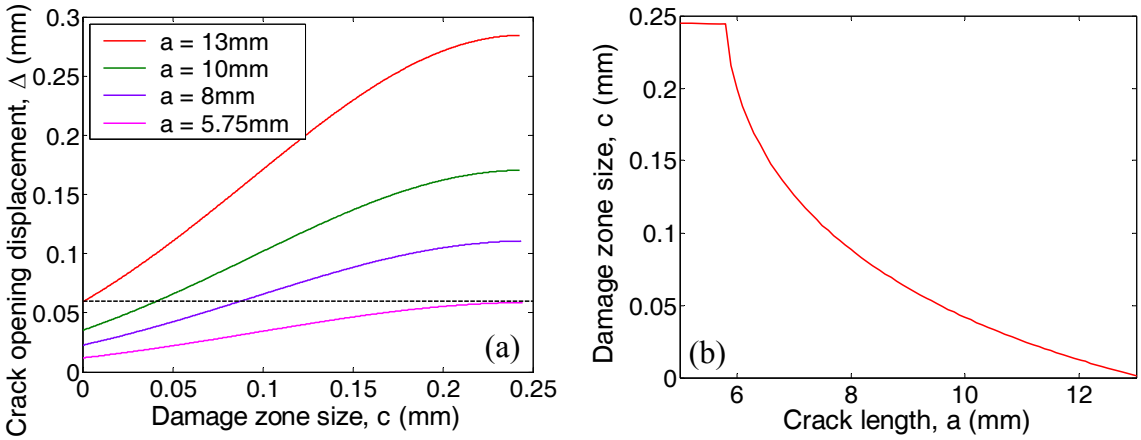

Figure 4.6: (a) Opening displacements at the loading point as a function of the damage zone size for different crack lengths, calculated based on the analytical model; (b) the damage zone size as a function of the crack length for effective $h_w = 0.06$mm.

Fig. 4.7a plots the crack opening displacements at different crack lengths. The vertical dashed line indicates the location of the initial crack tip (x = 0), and the horizontal dashed line indicates the critical opening displacement ($\delta_c = 2\Gamma/\sigma_0 = 200$nm). The interfacial crack tip starts advancing when the crack length reaches a critical value a = 5.75 mm, where the crack tip opening displacement (CTOD) reaches the critical separation, $\delta^* = \delta_c$. Fig. 4.7b shows the traction along the interface, which is zero for $x < 0$. For $x > 0$, the traction increases until it reaches the interfacial strength (σ_0 =18MPa), beyond which point the traction decreases and becomes negative. The first part corresponds to a damage zone, and the second part is due to elastic bridging. The negative traction is a result of contact between the two surfaces.

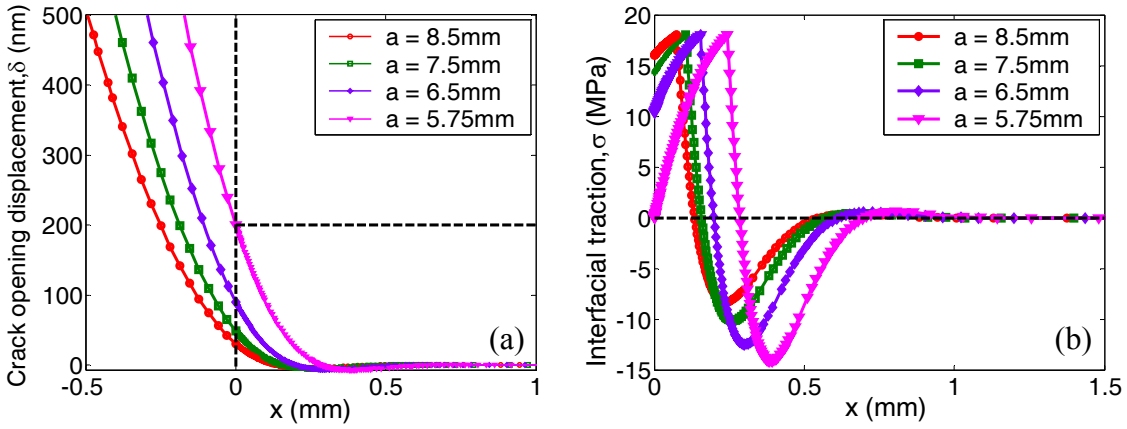

Figure 4.7: Results from the analytical model: (a) crack opening profiles; (b) distributions of the interfacial traction.

The energy release rate for the wedge-loaded DCB specimen can be calculated by the J-integral over a contour around the crack tip enclosing the entire cohesive zone:

$$G = J = -2\int_0^\infty \left(\sigma(x)\frac{dv}{dx} \right) dx \tag{4.31}$$

With the bilinear traction-separation relation of the interface, we obtain that

$$J = \frac{2\Gamma\left(\delta^* - \delta_0\right)}{\delta_c - \delta_0} - \frac{\sigma_0\left(\delta^{*2} - \delta_0^2\right)}{2(\delta_c - \delta_0)} + G_0 \tag{4.32}$$

where G_0 is the critical energy release rate for damage initiation as given in Eq. (4.20). It can be shown that

$$\frac{dJ}{d\delta^*} = \frac{2\Gamma - \sigma_0\delta^*}{\delta_c - \delta_0} = \sigma_0 \frac{\delta_c - \delta^*}{\delta_c - \delta_0} = \sigma(\delta^*) \tag{4.33}$$

which recovers the traction-separation relation.

As introduced in the previous section, the accuracy of experimentally determined traction-separation relation relies on the accuracy of J-integral calculations and the crack tip location. The effects of the two essential factors, J and δ^*, on the extraction of interfacial traction-separation relation are examined in the following. Using the analytical model with interfacial interaction, we plot in Fig. 4.8a the energy release rate as a function of the crack length. For comparison, the energy release rate predicted by the simple DCB in Eq. (4.3) is also plotted, together with that by Eq. (4.16). Using Eq. (4.16), the interaction across the interface is purely elastic, and it predicts an energy release rate slightly lower than that from Eq. (4.3) but higher than Eq. (4.32), for which the interfacial interaction includes a damage zone. When the crack length is large, consequently small damage zone, the energy release rates predicted by the three formulas are nearly identical. The discrepancy increases between Eq. (4.3) and Eq. (4.32) with the decrease of the crack

length (i.e. increase of damage zone). Fig. 4.8b is the crack opening displacement as a function of the crack length for the crack tip and two nearby points.

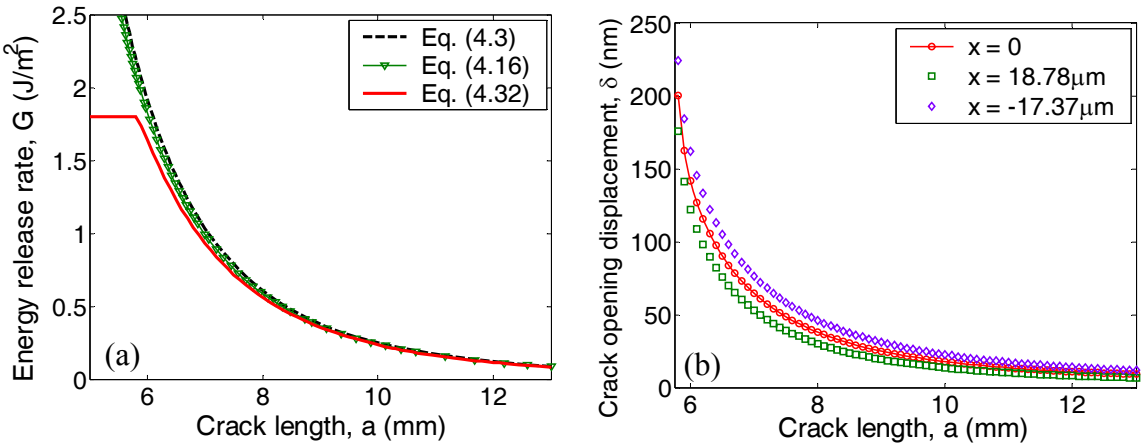

Figure 4.8: (a) The energy release rate as a function of the crack length; (b) the crack opening displacements as a function of the crack length for the crack tip and two nearby points.

Based on Fig 4.8, Fig 4.9a plots the calculated J-integral as a function of crack opening displacement for the crack tip and two nearby points. From Eq. (4.2), the traction-separation relation for an interface can then be determined, as shown in Fig. 4.9b. It can be seen that using CTOD recovers the bilinear traction-separation relation in the analytical model, and using the opening displacement not at the crack tip leads to errors in the traction-separation relation. Therefore the success of such measurements relies on the accuracy of J-integral calculations and the crack tip location.

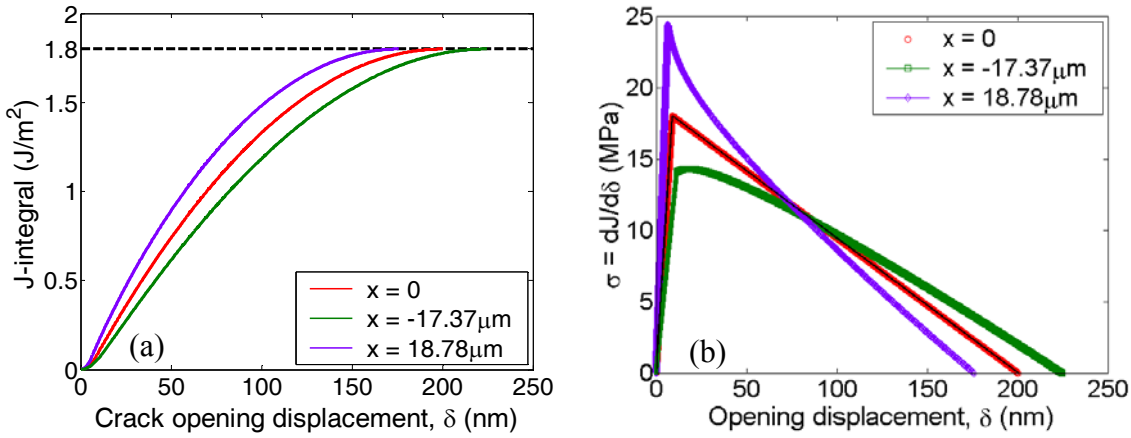

Figure 4.9: (a) Calculated J-integral versus the crack opening displacements by Eq. (4.32); (b) calculated traction-separation relation using the crack-tip opening displacement in comparison with two nearby opening displacements by Eq. (4.2).

4.4 Finite element analysis

In this section, two-dimensional finite element models are developed in ABAQUS [68] to simulate the interfacial delamination of the wedge-loaded DCB test. First, to better understand the results from the analytical solution, the numerical results by a bilayer finite element model are presented. A trilayer model including the epoxy is then constructed, and the effects of the epoxy layer on the measurable quantities (the crack length and NCOD) are studied. In comparison with the experimental data, the traction-separation relation for the Si/epoxy interface is determined.

4.4.1 A bilayer model

Figure 4.10 is an example mesh around the crack tip. The Si beams are modeled using 8-node quadrilateral plane-strain elements (CPE8R). The wedge is modeled as a

rigid body with frictionless hard contact with the surface of each Si beam. The interface between the Si beams is modeled by a layer of cohesive elements (COH2D4), using the bilinear traction-separation relation in ABAQUS as shown in Fig. 1.9. The geometries and material properties have been presented in Section 4.2.2, and the interfacial cohesive parameters are the same as those used in the analytical model (K_0 =2×10^{15}N/m^3, σ_0 =18MPa, and Γ =1.8J/m^2)

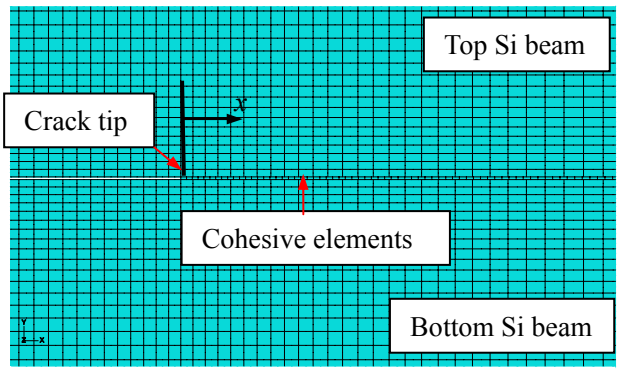

Figure 4.10: An example mesh around the crack tip of the bilayer numerical model.

Figure 4.11 shows the numerical results of the bilayer model, in which the wedge displacement (u_w) increases gradually as the loading parameter. Figures 4.11a and 4.11b plot the crack opening profiles and the distributions of the interfacial tractions at different loading displacements, corresponding to different crack lengths. The interfacial crack tip starts advancing when u_w =7.275mm. Both of the plots agree qualitatively with Fig. 4.7 by the analytical solution. Fig. 4.11c shows the interfacial damage variable D, which varies between 1 and 0 within the damage zone. As the crack tip advances, it leaves behind a pair of new crack surfaces with D = 1 and σ = 0.

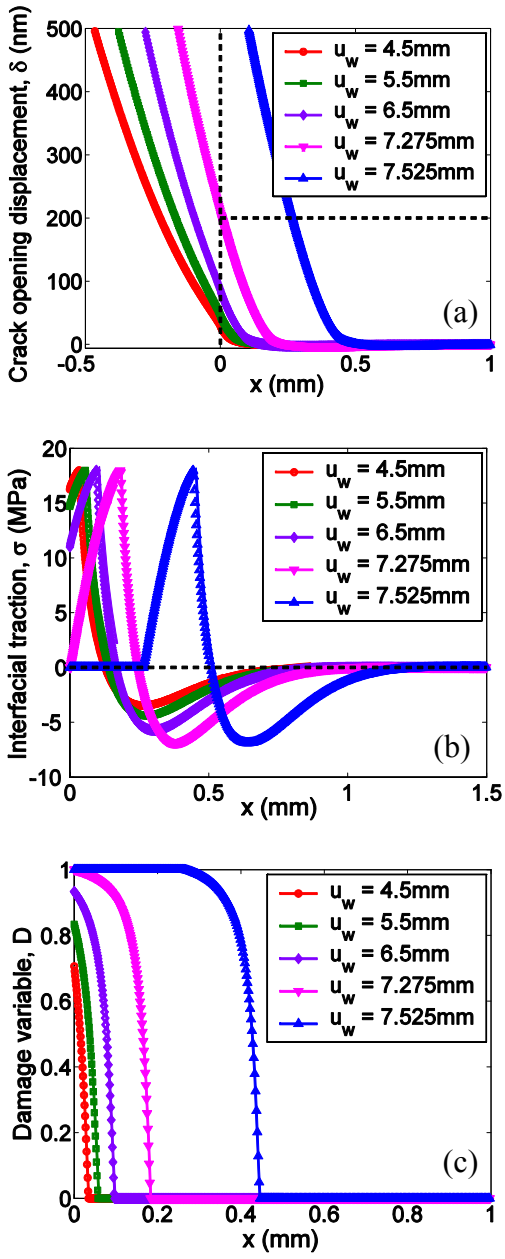

Figure 4.11: Numerical simulation of a wedge-loaded DCB specimen: (a) the crack opening displacement; (b) the interfacial traction; (c) the interfacial damage variable.

Figure 4.12a plots the crack length as a function of the wedge displacement, starting from an initial crack length (a_0 = 13 mm). The crack length decreases linearly as

$a = a_0 - u_w$ until the crack starts to grow when u_w =7.275mm. Figure 4.12b shows the damage zone size as a function of the wedge displacement. The analytical model result is also plotted. The comparison shows that the analytical solution overestimates the damage zone size, which may be attributed to the simple beam approximation in the analytical model.

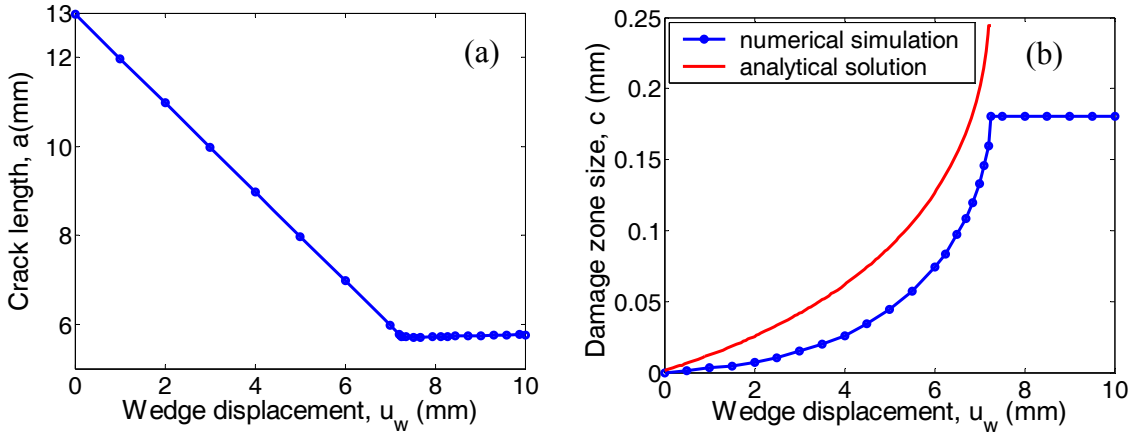

Figure 4.12: (a) The crack length and (b) the damage zone size versus the wedge displacement for a wedge-loaded DCB specimen.

Figure 4.13a is the CTOD as a function of the crack length, in comparison with the analytical solution. The numerical simulation agrees well with the analytical model for long cracks, and slight discrepancy occurs as the crack length decreases, with the analytical model overestimating the CTOD. Figure 4.13b is the numerical result of the energy release rate as a function of the crack length, with the analytical solutions by Eqs. (4.3) and (4.32) also plotted. The comparison shows that the analytical model improves the agreement with the numerical simulations compared to the simple beam equation in

Eq. (4.3). There is still discrepancy between the analytical model and finite element simulation, which may be attributed to the shear effect [126, 127].

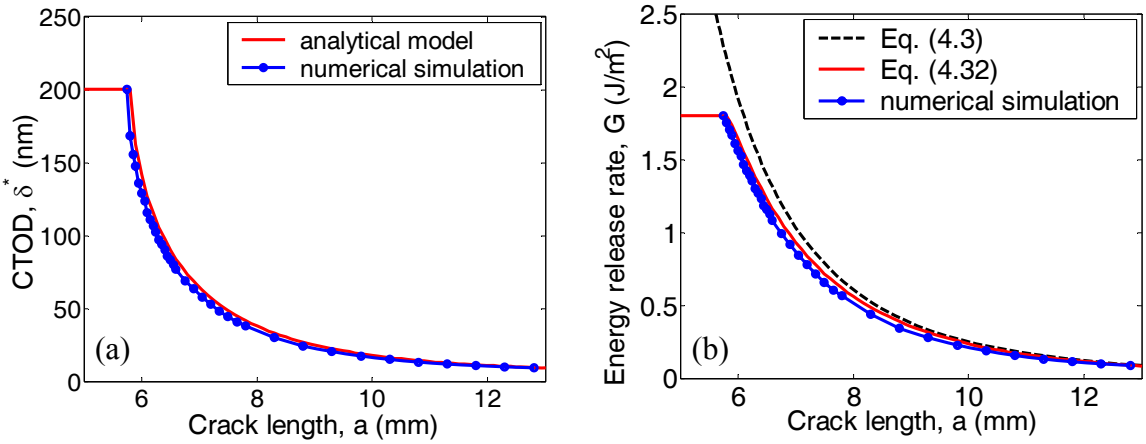

Figure 4.13: (a) The crack tip opening displacement and (b) the energy release rate as a function of the crack length.

4.4.2 A trilayer model

In previous sections, we have developed both analytical and numerical bilayer models for wedge-loaded DCB specimens using a bilinear traction-separation relation for the interface. The modeling results provide insightful details for crack opening and interfacial delamiantion. In particular, it is emphasized that both the J-integral and the crack tip must be accurately measured to obtain the correct traction-separation relation. In this section, a trilayer model is constructed, consisting of two Si beams with an epoxy layer in between as in Fig. 4.2. The effects of both epoxy layer and interfacial parameters (toughness and strength) on the crack length and NCOD are examined.

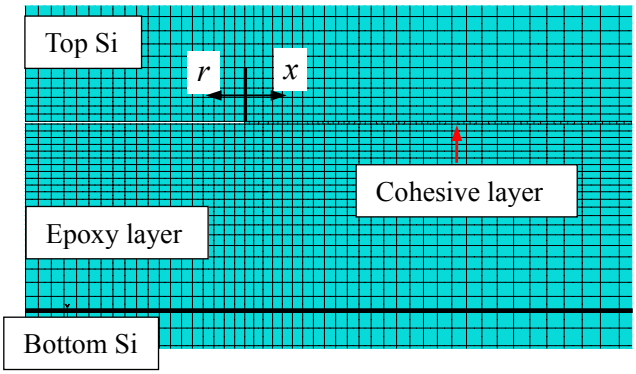

Figure 4.14: An example mesh around the crack tip of the trilayer finite element model.

Figure 4.14 is an example mesh around the crack tip. Both the Si beams and the epoxy layer are modeled using 8-node quadrilateral plane-strain elements (CPE8R). The interface between the epoxy and the top Si beam is modeled by a layer of cohesive elements (COD2D4), while the epoxy and the bottom Si beam are perfectly bonded. The effect of mode mix is ignored in the present model as the DCB test is predominantly mode-I, and the same interfacial cohesive parameters are used, with $K_0 = 2\times10^{15}\text{N/m}^3$, σ_0 = 18MPa, and Γ =1.8J/m^2. The elastic properties are E_{epoxy} = 2.03GPa, ν_{epoxy} = 0.33.

Figure 4.15a plots the crack length as a function of the wedge displacement. For comparison, the result by the bilayer numerical model is also plotted. The effect of the epoxy layer on the crack length is negligible, with difference around 0.4% for the steady-state crack length (a_{ss} = 5.7mm for the trilayer model and a_{ss} = 5.725 for the bilayer model). Figure 4.15b is the NCODs around the crack tip for different wedge displacements before crack growth. The dashed lines represent the numerical results by the bilayer model for the same wedge displacements. The comparison shows that the NCODs by the trilayer model (asymptotic behavior) are drastically different from those

by the bilayer model, especially for the opening profile in the region near the crack tip. The effect of the epoxy layer on the NCODs is attributed to the fact that epoxy is much more compliant than Si. As a result, the local deformation of the epoxy layer needs to be considered in the analysis of the local NCOD data.

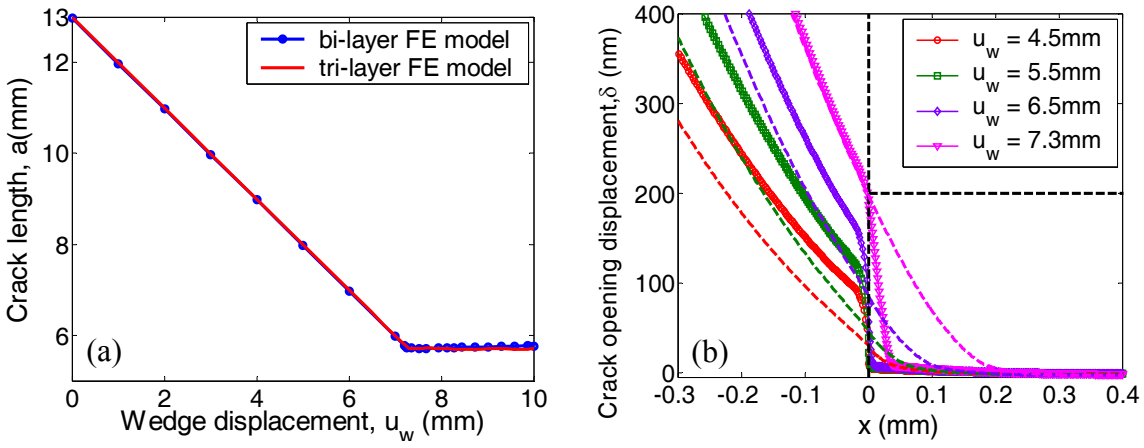

Figure 4.15: Comparison between the bilayer and trilayer finite element models. (a) the crack length as a function of the wedge displacement, and (b) crack opening profiles for different wedge loading displacements.

As discussed in Chapter 1, the key parameters for cohesive interface modeling are the cohesive strength σ_0 and toughness Γ, while the initial elastic stiffness (K_0) plays a secondary role. In the following study, we fix the initial stiffness as $K_0 = 2\times10^{15}\text{N/m}^3$, and vary the strength and toughness to examine their effects on the measured quantities (a_{ss} and NCOD).

Figure 4.16a shows the steady-state crack length a_{ss} as a function of the interface toughness for two different interfacial strengths, in comparison with Eq. (4.3). Clearly Eq.

(4.3) overestimates the interface toughness for a particular crack length. On the other hand, a_{ss} depends weakly on the interfacial strength, as shown in Fig. 4.16b, suggesting that the interface toughness can be determined by matching the steady-state crack length calculated by the numerical model to that measured by experiments.

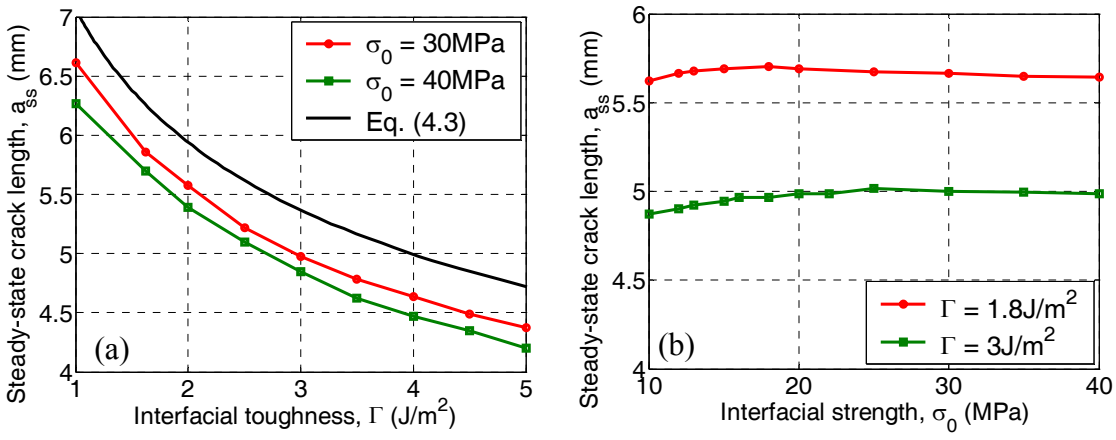

Figure 4.16: Steady-state crack length (a_{ss}) calculated by the trilayer finite element model: (a) effect of the interface toughness; (b) effect of the interfacial strength.

Figure 4.17 shows the steady-state NCOD near the crack tip for different interfacial strength with a constant interface toughness $\Gamma = 1.8\text{J/m}^2$. To compare with the measurements, $r = 0$ is set at the point with the opening displacement $\delta_n = 10\text{nm}$, which is the minimum NCOD that can be measured by the IR-COI technique. The results indicate that the local NCOD depends sensitively on the interfacial strength, which allows us to determine the strength by such a comparison. It is found that the shape of the NCOD curve varies with the damage zone size at the crack tip. By the cohesive zone model, a damage zone with the opening displacement between δ_0 and δ_c develops as the crack

grows. As shown in Fig. 1.9 for the bilinear traction-separation relation, the opening displacement for damage initiation depends on the interfacial strength $\delta_0 = \sigma_0/K_0$. For a fixed interface toughness (Γ = 1.8J/m^2), the critical opening displacement also depends on the interfacial strength, $\delta_c = 2\Gamma/\sigma_0$. As the strength increases, the window between the two opening displacements becomes narrower and the damage zone size decreases. At the limit of small-scale bridging, we approach the prediction by linear elastic fracture mechanics, with square-root dependence of the crack opening displacement, i.e., $\delta_n \sim \sqrt{r}$. On the other hand, when the strength decreases, the damage zone size increases. In the regime of large-scale bridging, the crack opening displacement scales with r differently. Figure 4.18 shows the calculated damage zone size as a function of the interfacial strength. Figure 4.19 shows the deformation and stress contours near the crack tip for two examples, with small-scale and large-scale bridging, respectively.

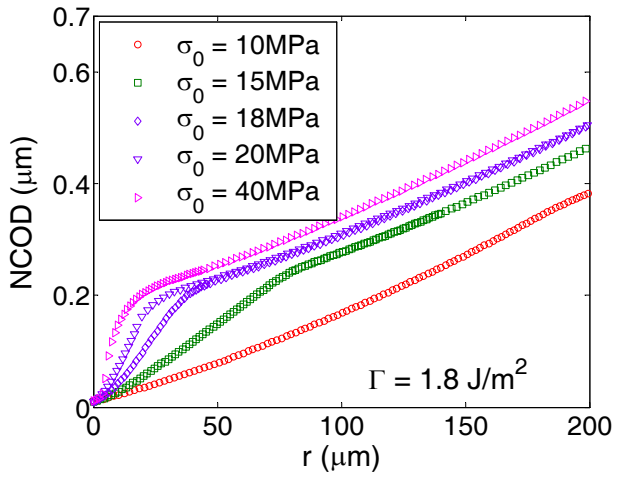

Figure 4.17: Effect of interfacial strength on the NCOD corresponding to steady state for constant interface toughness Γ = 1.8J/m^2.

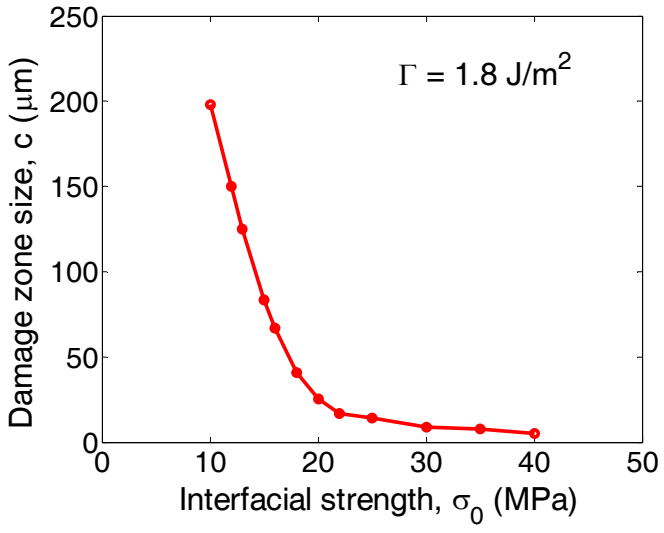

Figure 4.18: Calculated damage zone size as a function of the interfacial strength.

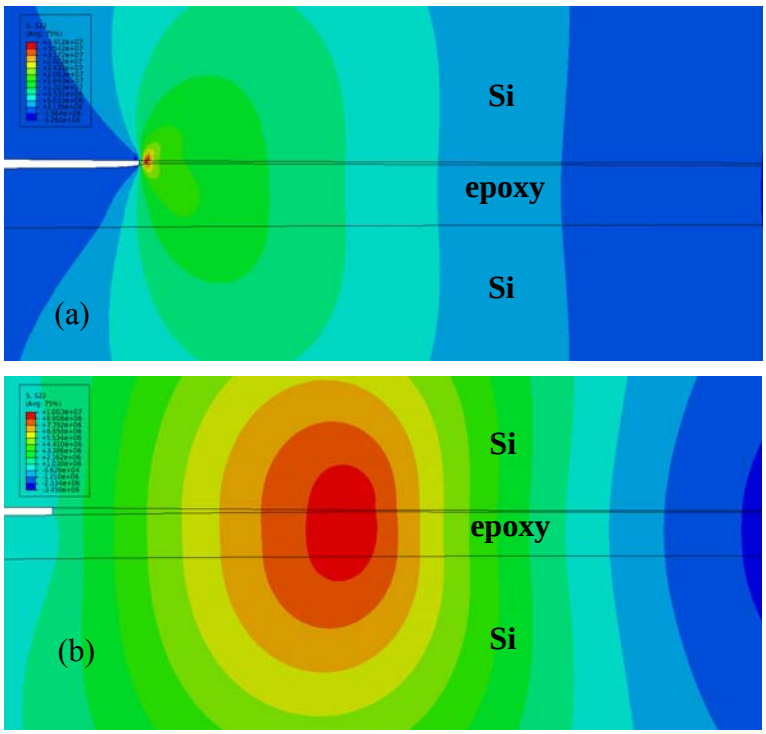

Figure 4.19: Two examples for: (a) small-scale bridging, with σ_0 = 40MPa; (b) large-scale bridging with σ_0 = 10MPa. The interface toughness is 1.8 J/m^2 for both cases.

4.5 Determination of toughness and strength

By examining the effects of interface toughness and strength on both the crack length and NCOD, we suggest a two-step procedure to determine the toughness and strength for the Si/epoxy interface as follows. First, the interface toughness is determined by comparing the steady-state crack length (a_{ss}): we can use a roughly estimated strength and vary the interface toughness to match the steady-state crack length measured by experiments. As shown in Fig. 4.20, the interface toughness is determined to be 1.8 J/m^2.

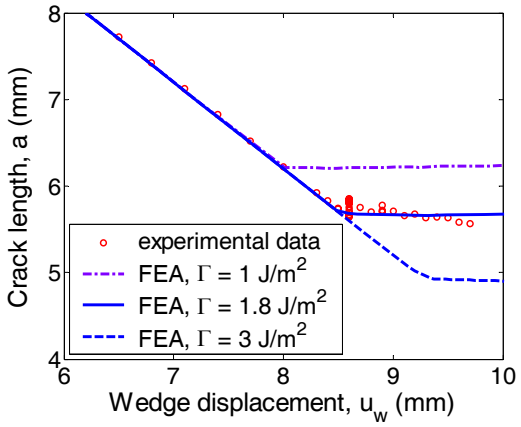

Figure 4.20: Comparison between FEA and experiment, for the steady-state crack length.

Next, with the determined interface toughness, the interfacial strength is more precisely determined by comparing the local NCOD curves between the numerical simulation and the experimental measurements. A reasonable agreement is obtained by using σ_0 =18MPa as shown in Fig. 4.21, where the error bars indicate the range of experimental errors. With the determined interfacial properties, Γ =1.8J/m^2 and σ_0 = 18MPa, Fig. 4.22 shows comparison of the other NCOD curves between the numerical

model and the experimental measurements during the wedge loading process. The comparison shows that the NCOD curves by the numerical simulation match reasonably well with those by experimental measurements.

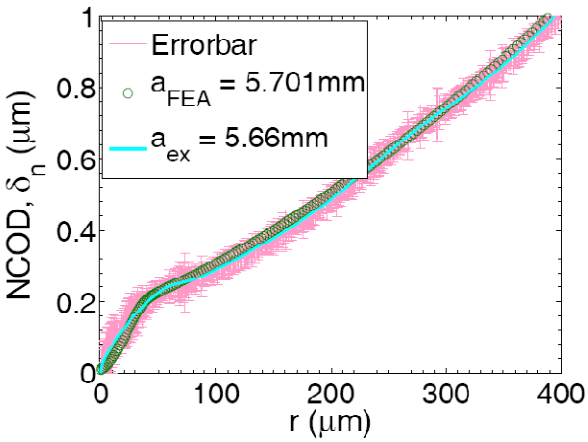

Figure 4.21: Comparison between FEA and experiment for the steady-state NCOD, with interfacial strength σ_0 =18MPa and the determined interface toughness.

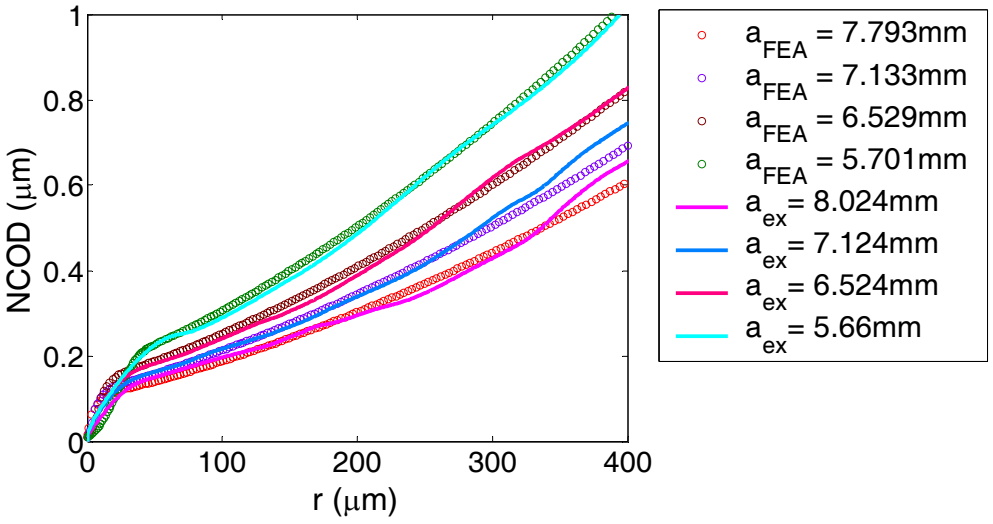

Figure 4.22: Near tip comparison of NCODs between FEA and experiments, with determined interfacial properties Γ =1.8J/m^2 and σ_0 =18MPa.

4.6 Summary

In summary, by combining experimental measurements with finite element modeling, a hybrid approach is developed in this chapter to determine the traction-separation relation for a bimaterial interface. First, both analytical and finite element models are developed for wedge-loaded double cantilever beam specimens. The modeling results provide insightful details for crack opening and interfacial delamination. It is found that both the J-integral and the location of crack tip must be accurately measured to obtain the correct traction-separation relation. A trilayer finite element model is then constructed to account for the effect of the epoxy layer. By examining the effects of interfacial properties (toughness and strength) on the quantities measured in experiments (steady-state crack length and NCOD), a two-step fitting procedure is proposed to determine the interface toughness and strength by comparing the simulation results with experimental measurements.

Chapter 5

Conclusions

In this dissertation, the approaches of LEFM and CZM are employed to study fracture and delamination of elastic thin films on compliant substrates under various loading conditions, with a focus on the effects of interfacial delamination. Furthermore, a hybrid approach combining numerical simulations with experimental measurements is developed to determine traction-separation relations for cohesive zone modeling of interfacial delamination.

In Chapter 2, compression-induced buckling of elastic thin films on elastic compliant substrates is studied by analytical and numerical methods. First, without delamination, we present an analytical solution for wrinkling that takes into account the effects of Poisson's ratio of the substrate. In comparison with a nonlinear finite element analysis, an approximate formula is derived to estimate the normal traction at the interface and to predict initiation of wrinkle-induced delamination. With a pre-existing delamination crack, the critical strain for the onset of buckling instability is predicted by a semi-analytical solution and by finite element eigenvalue analysis. It is found that, for an intermediate delamination size, the critical compressive strain for onset of buckling is lower than the previous solutions for both wrinkling and buckle-delamination. Nonlinear post-buckling analysis is then conducted to simulate concomitant wrinkling and buckle-delamination, showing a long-range interaction between the two buckling modes through the compliant substrate. Finally, by using a layer of cohesive elements for the interface,

progressive co-evolution of wrinkling and delamination is simulated. In particular, the effects of interfacial properties (strength and toughness) on the initiation and propagation of wrinkling-induced interfacial delamination is examined. Relevant experimental observations and potential applications in thin-film metrology are discussed along with the theoretical and numerical results.

Chapter 3 considers effects of interfacial delamination/substrate cracking on channel cracking in elastic thin films under tension. It is found that, depending on the elastic mismatch and the toughness of interface and substrate, a channel crack may grow with interfacial delamination and/or substrate cracking. An effective energy release rate for the steady-state growth of a channel crack is defined to account for the influence of interfacial delamination/substrate cracking on both the driving force and the fracture resistance, which can be significantly higher than the energy release rate assuming no interfacial delamination or substrate penetration. By comparing the effective energy release rate, the competition between the two fracture modes is discussed. Cohesive zone modeling is then employed to simulate the nucleation and growth of delamination and penetration cracks from the root of a channel crack. By comparing the results from the approaches of LEFM and CZM, the characteristic fracture resistance from small-scale bridging to large-scale bridging is identified.

To determine the nonlinear traction-separation relation for cohesive zone modeling of a bimaterial interface, a hybrid approach is developed in Chapter 4. Both analytical and numerical models for wedge-loaded double cantilever beam specimens are developed. First, the results from a bilayer model show that both the J-integral and the

location of crack tip must be accurately measured to obtain the correct traction-separation relation. A trilayer finite element model is then constructed to account for the effect of the epoxy layer. By examining the effects of interface toughness and strength on the quantities measured in experiments, a two-step fitting procedure is proposed to determine the interface toughness and strength based on the measurements of the steady-state crack length and the local crack opening displacements.

Extensions of foregoing studies are needed for future work. With respect to cohesive zone modeling of interfacial delamination, mode mix should be taken into account to explore the mixed-mode interfacial fracture behavior. The competition between delamination and penetration at the root of a channel crack could also be further investigated systematically. In addition, the discrepancy in the NCODs near the crack tip between finite element simulations and experimental measurements is yet to be resolved from both experimental and modeling sides.

Appendix A: An alternative finite element method for post-buckling analysis

One of the methods to analyze the post-buckling behavior of wrinkling and buckle-delamination is based upon coupling a linear elastic semi-infinite substrate to a nonlinear beam described by the von Karman theory. Due to the nonlinearity and the coupling between the normal and transverse displacements, we must resort to numerical methods to investigate the post-buckling behavior. Since the substrate is linear elastic and the beam is represented as 1D line elements, it is possible to generate solutions to this system with a 1D mesh without a 2D finite element mesh for the substrate. To accomplish this we draw upon the work of Carka and Landis [129] to develop the finite element equations, summarized here as follows.

The principle of virtual work for the film/substrate system is written as

$$\int \left(N\delta\varepsilon_{xx} + M\delta\kappa \right) dx + \int \left(\tau\delta u + q\,\delta w \right) dx = 0 \tag{A.1}$$

Here, N is the axial force in the film, M is the bending moment, u and w are the tangential and normal displacements at the film/substrate interface, $\varepsilon_{xx} = u' + \left(w'\right)^2/2 - w''h/2$ is the axial strain at the mid-plane of the film, $\kappa = w''$ is the curvature, τ and q are the tangential and normal tractions at the interface. The constitutive response of the film is taken as, $N = E_f h\varepsilon_{xx}/(1-\nu_f^2)$ and $M = E_f h^3\kappa/12(1-\nu_f^2)$. The novelty of the present method is in the treatment of the second term on the left-hand side of this equation. The method is based upon the realization that the solution in the substrate can be obtained analytically as an infinite series. Specifically, the displacement

and the traction at the film/substrate interface can be written in the form

$$2\mu_s u^s = \sum_{n=0}^{\infty} \left\{ \left[A_n + B_n(2-2\nu_s) \right] \sin(n\pi x) - \left[C_n + D_n(2-2\nu_s) \right] \cos(n\pi x) \right\} + 2\mu_s \varepsilon x \tag{A.2a}$$

$$2\mu_s w^s = \sum_{n=0}^{\infty} \left\{ -\left[A_n - B_n(1-2\nu_s) \right] \cos(n\pi x) - \left[C_n - D_n(1-2\nu_s) \right] \cos(n\pi x) \right\} \tag{A.2b}$$

$$\tau = \sum_{n=0}^{\infty} \left\{ -n\pi \left[A_n + B_n \right] \sin(n\pi x) + n\pi \left[C_n + D_n \right] \cos(n\pi x) \right\} \tag{A.2c}$$

$$q = \sum_{n=0}^{\infty} \left\{ n\pi A_n \cos(n\pi x) + n\pi C_n \sin(n\pi x) \right\} \tag{A.2d}$$

where μ_s is the substrate shear modulus, ν_s is the substrate Poisson's ratio, ε is the nominal strain, and A_n, B_n, C_n and D_n are unknown coefficients that must be determined by linking to the finite element solution. This link is established by enforcing the weak form of displacement continuity at the interface as,

$$\int \left[\left(u^{FE} - u^s \right) \delta\tau + \left(w^{FE} - w^s \right) \delta q \right] dx = 0 \tag{A.3}$$

Equation (A.3) is used to relate the unknown coefficients A_n, B_n, C_n and D_n to the nodal displacements, u^J and w^J, from the finite-element solution. Note that u^{FE} and w^{FE} are interpolated from u^J and w^J through the shape functions N^J as $u^{FE} = \sum_J N^J u^J$ and $w^{FE} = \sum_J N^J w^J$. The procedure required to execute this step is detailed in Carka and Landis (2011). Ultimately the process leads to the result,

$$\int \left(\tau \delta u + q \delta w \right) dx = \left\{ \delta \mathbf{u}^N \right\}^T \left[\mathbf{K} \right] \left\{ \mathbf{u}^N \right\} + \left\{ \delta \mathbf{u}^N \right\}^T \left\{ \mathbf{F}^s \right\} \tag{A.4}$$

where $[\mathbf{K}^s]$ is the stiffness of the semi-infinite substrate, $\{\mathbf{F}^s\}$ is a set of nodal forces

associated with the nominal strain ε, and $\{\mathbf{u}^N\}$ is the array of nodal displacements. Note that the stiffness contribution relates the nodal displacements on the interface to the conjugate forces supplied by the substrate. This stiffness matrix is fully dense and symmetric.

For the buckling analysis, a standard eigenvalue analysis procedure is implemented first. A standard Newton-Raphson method is implemented to deal with the nonlinearity associated with the first term of Equation (A.1) for post-buckling analyses. Perturbations in the initial displacement fields are introduced using the eigenmodes. Unlike the geometric imperfections used in the 2D finite element model, the initial displacement perturbations do not affect the equilibrium solution. The 1D finite element method is computationally more efficient than the 2D model. In addition, it eliminates the dependence on the substrate thickness in the 2D model. On the other hand, the use of the analytical solution in (A.2) is restricted to linear kinematics for the substrate.

Appendix B: A semi-analytical solution for buckle-delamination

Following the approach by Yu and Hutchinson [95], the plane-strain buckle-delamination problem is solved by considering two parts as illustrated in Fig. B.1. The delaminated film is modeled by the nonlinear von Karman plate theory, and the remaining film/substrate system is treated as a linear elasticity problem. The two parts are coupled by requiring continuity of displacements and rotation at the delamination edge.

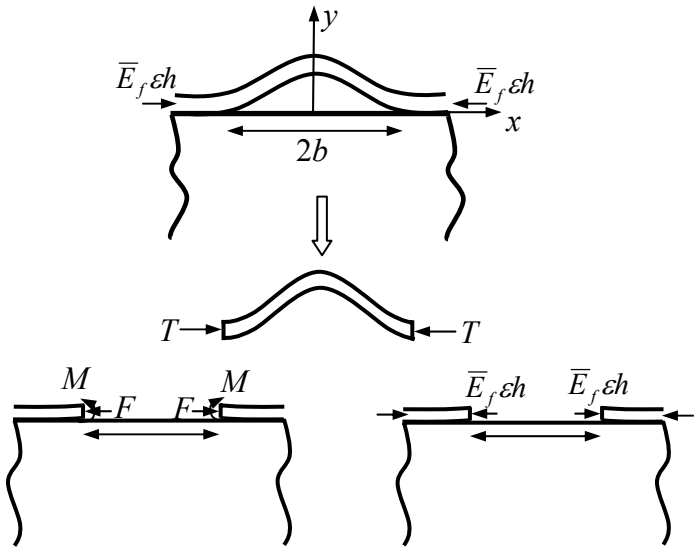

Figure B.1: Schematic illustration of the plane-strain problem for buckle-delamination.

The governing equations for the delaminated part of the film are:

$$\frac{\overline{E}_f h^3}{12}\frac{d^4 w}{dx^4} + T\frac{d^2 w}{dx^2} = 0 \tag{B.1}$$

$$\frac{du}{dx} + \frac{1}{2}\left(\frac{dw}{dx}\right)^2 + \left(\frac{T}{\overline{E}_f h} - \varepsilon\right) = 0 \tag{B.2}$$

where u and w are the in-plane and out-of-plane displacements of the film, ε is the nominal strain at the unbuckled state ($\varepsilon > 0$ for compression), and T is the in-plane membrane force.

The boundary conditions are:

$$\left.\frac{dw}{dx}\right|_{x=0} = \left.\frac{d^3w}{dx^3}\right|_{x=0} = 0 \text{ and } \left.\frac{d^2w}{dx^2}\right|_{x=b} = \frac{M}{D} \tag{B.3}$$

where M is the bending moment at the edge of delamination and $D = \overline{\overline{E}}_f h^3/12$.

Solving Eqs. (B.1) and (B.2) with the boundary conditions, we obtain that

$$u(x) = \left(\varepsilon - \frac{T}{\overline{\overline{E}}_f h}\right)x - \left(\frac{Mb}{2D\lambda\cos\lambda}\right)^2\left[x - \frac{b}{2\lambda}\sin(\frac{2\lambda x}{b})\right] \tag{B.4}$$

$$w(x) = A_1 - \frac{Mb^2}{D\lambda^2\cos\lambda}\cos\left(\frac{\lambda x}{b}\right) \tag{B.5}$$

where $\lambda = b\sqrt{T/D}$, and A_1 is a constant to be determined. The rotation at the edge of delamination is then

$$\theta = \left.\frac{dw}{dx}\right|_{x=b} = \frac{Mb}{D\lambda}\tan(\lambda) \tag{B.6}$$

For the remaining part of the film/substrate system, by dimensional considerations, the in-plane displacement, rotation and out-of plane displacement of the film at the edge of delamination can be written in form of

$$u(x=b) = a_{11}\frac{F}{\overline{\overline{E}}_f} + a_{12}\frac{M}{\overline{\overline{E}}_f h} \tag{B.7}$$

$$\theta(x=b) = a_{21}\frac{F}{\overline{\overline{E}}_f h} + a_{22}\frac{M}{\overline{\overline{E}}_f h^2} \tag{B.8}$$

$$w(x=b)=a_{31}\frac{F}{\overline{E}_f}+a_{32}\frac{M}{\overline{E}_f h} \tag{B.9}$$

where $F=T-h\overline{E}_f\varepsilon$, and the coefficients a_{ij} are to be determined numerically. By the reciprocal theorem, $a_{21}\equiv a_{12}$.

Assuming continuity of the displacements and rotation at the edge of delamination, we combine Eqs. (B.4-B.9) and obtain that

$$\left(\frac{b}{h}+a_{11}\right)\frac{F}{\overline{E}_f h}+a_{12}\frac{M}{\overline{E}_f h^2}+\frac{b}{h}\left(1-\frac{\sin 2\lambda}{2\lambda}\right)\left(\frac{Mb}{2D\lambda\cos\lambda}\right)^2=0 \tag{B.10}$$

$$a_{21}\frac{F}{\overline{E}_f h}+\left(a_{22}+\frac{12b}{\lambda h}\tan\lambda\right)\frac{M}{\overline{E}_f h^2}=0 \tag{B.11}$$

$$a_{31}\frac{F}{\overline{E}_f}+\left(a_{32}+\frac{12b^2}{\lambda^2 h^2}\right)\frac{M}{\overline{E}_f h}=A_1 \tag{B.12}$$

B.1 Critical strain

Neglecting the nonlinear term, Eqs. (B.10) and (B.11) form a linear eigenvalue problem, which predicts the critical condition for onset of buckling:

$$\frac{12b}{\lambda h}\tan(\lambda)=\frac{a_{12}^2}{a_{11}+b/h}-a_{22} \tag{B.13}$$

Recall that $\lambda=b\sqrt{T/D}$. The critical membrane force T_c is determined by the critical value of λ obtained from Eq. (B.13). The critical nominal strain (ε_B^*) for onset of buckling is then predicted by the relation $T_c=\overline{E}_f h\varepsilon_B^*$. Rewriting Eq. (B.13) in terms of the critical strain, we obtain Eq. (2.21).

B.2 Post-buckling analysis

From Eq. (B.11), we have

$$\frac{M}{\overline{E}_f h^2} = -\frac{F}{\overline{E}_f h}\left(\frac{a_{12}}{\frac{12b}{\lambda h}\tan\lambda + a_{22}}\right) \tag{B.14}$$

Inserting Eq. (B.14) into (B.10) results in a nonlinear equation,

$$\left(\frac{b}{h} + a_{11} - \frac{a_{12}^2}{\frac{12b}{\lambda h}\tan\lambda + a_{22}}\right) + \frac{b}{h}\left(1 - \frac{\sin 2\lambda}{2\lambda}\right)\left(\frac{6b}{h\lambda\cos\lambda}\right)^2\left(\frac{a_{12}}{\frac{12b}{\lambda h}\tan\lambda + a_{22}}\right)^2\left(\frac{\lambda^2 h^2}{12b^2} - \varepsilon\right) = 0 \tag{B.15}$$

from which λ can be solved as a function of ε. The membrane force T is then obtained as $\lambda = b\sqrt{T/D}$.

When $\varepsilon > \varepsilon_B^*$, it can be shown that $T < \overline{E}_f h\varepsilon$. In other words, the membrane force is partly relaxed by buckling. With $F = T - h\overline{E}_f\varepsilon$, the bending moment M is obtained from Eq. (B.14). Next, inserting Eq. (B.12) into (B.5), we obtain the buckle amplitude as

$$A = w(x=0) = ha_{31}\left(\frac{T}{\overline{E}_f h} - \varepsilon\right) + a_{32}\frac{M}{\overline{E}_f h} + \frac{M}{T}\left(1 - \frac{1}{\cos\lambda}\right) \tag{B.16}$$

B.3 Calculating the coefficients a_{ij}

To calculate the coefficients a_{ij} in Eqs. (B.7)-(B.9), Yu and Hutchinson [95] used an integral equation method. In the present study, they are calculated by a finite element

method. As illustrated in Fig. B.2, a 2D plane-strain finite element model is constructed using ABAQUS. To simulate a semi-infinite substrate, the thickness and length of the substrate in the finite element model must be sufficiently large. In our calculations, we set $L = H = 1000h$. The crack length d is zero for this calculation. The edge of the film at $x = b$ is subjected to an axial force F and a bending moment M. The average displacements and rotation at the edge are calculated from the nodal displacements as

$$u(x=b) = \frac{1}{h}\int u(y)dy \tag{B.17}$$

$$\theta(x=b) = \frac{12}{h^3}\int u(y)ydy \tag{B.18}$$

$$w(x=b) = \frac{1}{h}\int w(y)dy \tag{B.19}$$

By applying an arbitrary force F with $M = 0$, the coefficients a_{i1} ($i = 1, 2, 3$) can be determined. Similarly, by applying an arbitrary moment M with $F = 0$, the coefficients a_{i2} can be determined.

B.4 Energy release rate

The energy release rate for growth of the interfacial crack may be calculated from the stress intensity factors [95]. However, the approach works only when the stress field at the crack tip exhibits the square-root singularity without oscillation [39]. For the present study, with $\nu_s = \nu_f = 1/3$, we calculate the energy release rate directly by the method of J-integral. For this purpose, a short crack ($d = h/2$) is introduced at the interface in the finite element model (Fig. B.2). Quarter-point singular elements are used at the

crack tip. The axial force F and the bending moment M, obtained from the post-buckling analysis in Eqs. (B.15) and (B.14), are applied at the edge of the film.

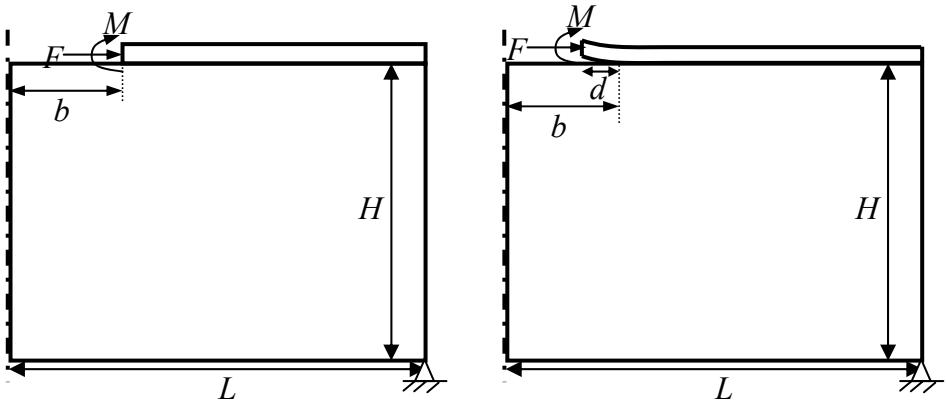

Figure B.2: Schematic of the finite element model used to calculate the coefficients a_{ij} and the energy release rate. The crack length d is zero for calculating a_{ij}. A symmetric boundary condition is assumed at the center of the delamination ($x = 0$), while the remote boundary at the right end is traction free. A mixed boundary condition is assumed at the bottom of the substrate with zero vertical displacement and zero shear traction.

Appendix C: Asymptotic solutions for short delamination crack from a channel root.

This Appendix summarizes asymptotic solutions from previous studies [39, 100, 130] for short delamination cracks emanating from the root of a channel crack (i.e., $d/h_f \to 0$ in Fig. 3.3a), and presents comparisons with numerical results from the finite element model shown in Fig. 3.3.

C.1 Zero elastic mismatch ($\alpha = \beta = 0$)

This is a case of crack kinking in a homogeneous solid. Without the interfacial delamination, the channel crack in the film is equivalent to a two-dimensional edge crack, with the stress intensity factor at the root

$$K_I = 1.1215\sigma_f\sqrt{\pi h_f} \tag{C.1}$$

For a small crack segment ($d << h_f$) kinking out of the plane of the edge crack, the stress intensity factors at the new crack tip are linearly related to the stress intensity factors at the tip of the parent crack [39], namely

$$\begin{aligned} K_I^d &= c_{11}K_I + c_{12}K_{II} \\ K_{II}^d &= c_{21}K_I + c_{22}K_{II} \end{aligned} \tag{C.2}$$

where the coefficients, c_{ij}, depend on the kink angle, as given by Hayashi and Nemat-Nasser [131]. Following He and Hutchinson [130], the coefficients can be written as

$$c_{11} = C_R + D_R\,,\; c_{21} = C_I - D_I \tag{C.3}$$

where $C = C_R + iC_I$ and $D = D_R + iD_I$ are two complex valued functions, with the

subscript *R* and *I* denoting their real and imaginary parts, respectively. An approximation by Cotterell [132] gives that

$$C = \frac{1}{2}\left(e^{-i\omega/2} + e^{-i3\omega/2}\right)$$
$$D = \frac{1}{4}\left(e^{-i\omega/2} - e^{-i3\omega/2}\right) \tag{C.4}$$

where ω is the kink angle. Cotterell and Rice [133] have shown that this approximation is asymptotically correct for small kink angles and is reasonably accurate for kink angles as large as 45° or even 90°, depending on the mode mix.

For the present problem with a channel crack kinking into the interface, the kink angle is 90° and $K_{II} = 0$. Under the plane strain condition, the energy release rate of the interfacial crack is

$$G_d\left(d \to 0\right) = \frac{\left(K_I^d\right)^2 + \left(K_{II}^d\right)^2}{\overline{E}} = \left(1.1215\right)^2 \pi\left(c_{11}^2 + c_{12}^2\right)\frac{\sigma_f^2 h_f}{\overline{E}} \tag{C.5}$$

A comparison between Eq. (C.5) and Eq. (3.3) gives the dimensionless coefficient

$$Z_d\left(d \to 0\right) = 1.258\pi\left(c_{11}^2 + c_{21}^2\right) \tag{C.6}$$

Using the approximation in Eq. (C.4) with $\omega = \pi/2$, we obtain that

$$c_{11} = \frac{\sqrt{2}}{4}, \quad c_{11} = -\frac{\sqrt{2}}{4} \tag{C.7}$$

Inserting (C.7) into (C.6) gives that

$$Z_d\left(d \to 0\right) = 0.9878 \tag{C.8}$$

This approximation agrees well with the numerical result shown in Fig. 3.4, where $Z_d = 0.9923$ for $d/h_f = 10^{-3}$.

For a channel crack penetrating into the substrate, the kink angle is 0^o and $K_{II} = 0$. Similar to the case of interfacial crack, the dimensionless coefficient is

$$Z_p\left(d_p \to 0\right) = 1.258\pi\left(c_{11}^2 + c_{21}^2\right) \tag{C.9}$$

Using the approximation in Eq. (C.4) with $\omega = 0$, we obtain that

$$c_{11} = 1,\ c_{21} = 0 \tag{C.10}$$

Inserting (C.10) into (C.9) gives that

$$Z_p\left(d_p \to 0\right) = 3.9521 \tag{C.11}$$

This approximation agrees very well with the numerical result shown in Fig. 3.15, where $Z_p = 3.952$ for $d_p/h_f = 10^{-3}$.

C.2 Crack deflection at a bimaterial interface

For an interface between two elastic materials with general elastic mismatch, an asymptotic solution by He and Hutchinson [100] gives the energy release rate of the delamination crack emanating from a perpendicular channel crack (Fig. 3.3a, $d << h_f$):

$$G_d = \left(\frac{1}{\overline{E}_f} + \frac{1}{\overline{E}_s}\right)\frac{K_1^2 + K_2^2}{2\cosh^2 \pi\varepsilon} = \left(\frac{1}{\overline{E}_f} + \frac{1}{\overline{E}_s}\right)\frac{k_1^2\left|C\right|^2 + \left|D\right|^2 + 2\mathrm{Re}\left(CD\right)\right|}{2\cosh^2 \pi\varepsilon} d^{1-2\lambda} \tag{C.12}$$

where C and D are dimensionless, complex valued functions of α and β, k_1 is a real valued constant representing the stress intensity at the root of the channel crack, and λ is determined by Eq. (3.6). This asymptotic solution leads to a power-law dependence of the Z_d function on the interfacial crack length as $d \to 0$, namely

$$Z_d = \frac{G_d}{\sigma_f^2 h_f/\overline{E}_f} \sim \left(\frac{d}{h_f}\right)^{1-2\lambda} \tag{C.13}$$

The normalized Z_p function follows the same power law as Eq. (C.13) as $d_p \rightarrow 0$.

Figures C.1 and C.2 plot the numerical solutions of Z_d from the finite element model (Fig. 3.3), in comparison with the asymptotic solution. When $\alpha < 0$ ($\beta = \alpha/4$), $0 < \lambda < 0.5$ and the log-log plot of Z_d vs. d/h_f (Fig. C.1) approaches a straight line of positive slope ($1-2\lambda > 0$) as $d/h_f \rightarrow 0$. When $\alpha > 0$, $\lambda > 0.5$, and the log-log plot (Fig. C.2) approaches a straight line of negative slope ($1-2\lambda < 0$). When $\alpha = \beta = 0$ (no elastic mismatch), $\lambda = 0.5$ and Z_d approaches a constant with zero slope in the log-log plot (Fig. C.2). The comparisons show good agreement between the numerical results and the asymptotic power law for short delamination cracks.

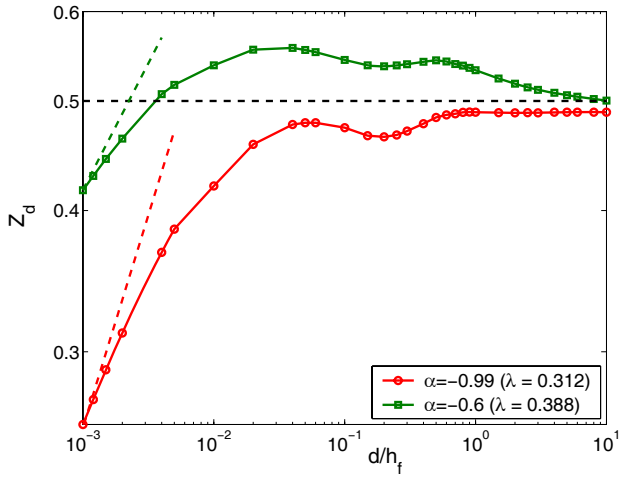

Figure C.1: Normalized energy release rate of interfacial delamination emanating from the root of a channel crack, for $\alpha = -0.99$ and $\alpha = -0.6$. The asymptotic power law, Eq. (C.13), is represented by the straight lines at the short crack limit with slopes, $1-2\lambda = 0.376$ and 0.224, respectively.

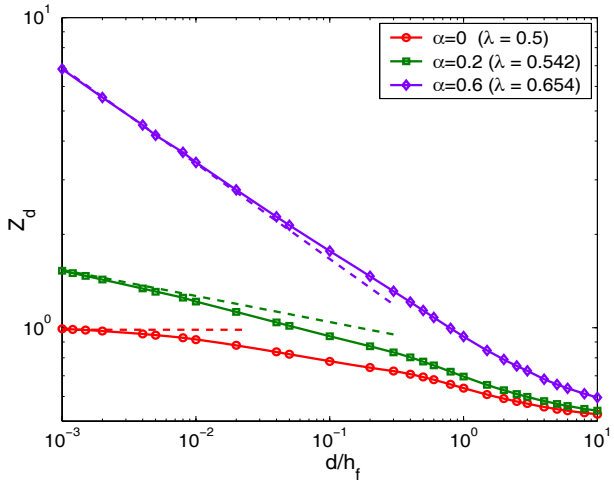

Figure C.2: Normalized energy release rate of interfacial delamination emanating from the root of a channel crack, for $\alpha = 0$, $\alpha = 0.2$, and $\alpha = 0.6$. The asymptotic power law, Eq. (C.13), is represented by the straight lines at the short crack limit with slopes, $1\text{-}2\lambda = 0$, -0.084, and -0.308, respectively.

Appendix D: A shear-lag model for initiation of interfacial delamination

A shear-lag model is developed to predict the critical condition for initiation of interfacial delamination from the root of a channel crack for large-scale bridging. Figure D.1a shows a schematic diagram of the plane strain problem, with uniform normal traction σ_f acting onto the surface of the channel crack. The interfacial properties are represented by the bilinear traction-separation relation as illustrated in Fig. D.1b, with K_0 for the elastic stiffness, $\hat{\tau}$ for the interfacial strength, and Γ_i for the interface toughness. The two characteristic displacements are: $\delta_c = 2\Gamma_i/\hat{\tau}$ and $\delta_0 = \hat{\tau}/K_0$.

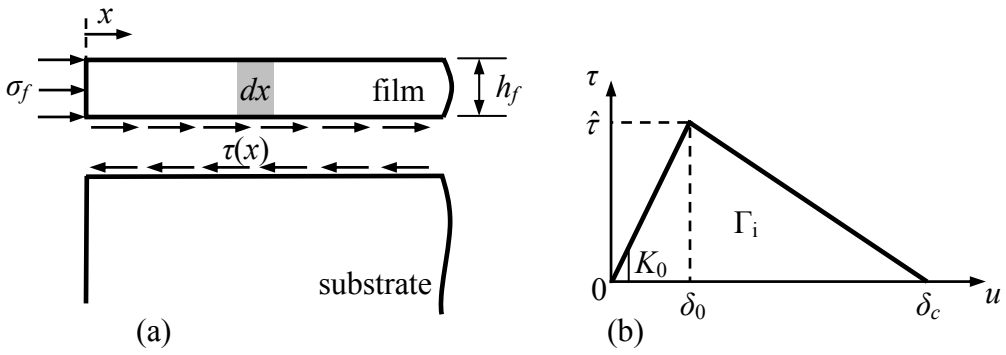

Figure D.1: (a) A schematic diagram of a film bonded to a rigid substrate, with uniform compression at one edge; (b) a bilinear relationship between the shear traction and displacement.

Consider an infinitesimal segment of the film of length dx, the force balance requires that

$$\frac{d\sigma}{dx} = \frac{\tau(x)}{h_f} \tag{D.1}$$

where $\sigma(x)$ is the normal stress in the film, assumed to be uniform across the film thickness, and $\tau(x)$ denotes the interfacial shear stress.

By the linear strain-displacement relation and the linear elastic constitutive relation for the film, the stress is related to the displacement (u) as

$$\sigma(x) = \overline{E}_f \frac{du}{dx} \tag{D.2}$$

The shear displacement at the root of the channel crack is denoted as $\delta^* = u\big|_{x=0}$. For the bilinear interfacial properties illustrated in Fig. D.1b, the problem can be solved in two steps: (1) the interface is in the elastic regime when $\delta^* < \delta_0$; (2) when $\delta^* > \delta_0$, a damage zone of size c is formed along the interface ($0 < x < c$), and beyond the damage zone ($x > c$), the interface remains elastic. Initiation of a delamination crack is then predicted when $\delta^* = \delta_c$.

In this analysis, the substrate is assumed to be rigid so that the deformation of the substrate is neglected.

D.1 Elastic regime of the interface

With a relatively small stress σ_f, the entire interface is in the elastic regime, and the shear traction along the interface is related to the shear displacement by

$$\tau(x) = K_0 u(x) \tag{D.3}$$

Combing Eqs. (D.1)-(D.3), we obtain a displacement equation

$$\frac{d^2u}{dx^2} = \frac{K_0}{\overline{E}_f h_f} u \tag{D.4}$$

The film is taken to be infinitely long with zero displacement at infinity ($x \to \infty$). Along with the traction condition at $x = 0$, Eq. (D.4) can be solved to obtain the shear displacement:

$$u(x) = \frac{\sigma_f h_f}{\overline{E}_f \lambda} \exp\left(-\frac{\lambda x}{h_f}\right) \tag{D.5}$$

where $\lambda = \sqrt{\frac{K_0 h_f}{\overline{E}_f}}$. At $x = 0$, the shear displacement is $\delta^* = \frac{\sigma_f h_f}{\overline{E}_f \lambda}$. Thus, the entire interface is in the elastic regime if $\delta^* < \delta_0$ or $\sigma_f < \hat{\tau}\sqrt{\frac{\overline{E}_f}{K_0 h_f}}$.

D.2 Damage along the interface

When $\delta^* > \delta_c$, a damage zone forms along the interface. Within the damage zone ($0 < x < c$), the interfacial shear stress $\tau(x)$ is related to the shear displacement $u(x)$ by:

$$\tau(x) = \hat{\tau}\frac{\delta_c - u}{\delta_c - \delta_0} \tag{D.6}$$

Together with Eqs. (D.1) and (D.2), the displacement equation becomes

$$\frac{d^2 u}{dx^2} = \frac{\hat{\tau}}{\overline{E}_f h_f}\frac{\delta_c - u}{\delta_c - \delta_0} \tag{D.7}$$

Solving Eq. (D.7), the shear displacement in the damage zone of the interface is obtained in the form:

$$u_1(x) = B_1 \cos(kx) + B_2 \sin(kx) + \delta_c \tag{D.8}$$

where $k = \sqrt{\frac{\hat{\tau}}{\bar{E}_f h_f}\frac{1}{\delta_c - \delta_0}} = \frac{\lambda}{h_f\sqrt{2\xi - 1}}$, and $\xi = \frac{K_0 \Gamma_i}{\hat{\tau}^2}$.

Beyond the damage zone ($x > c$), the interface remains elastic, and the shear stress $\tau(x)$ is related to the shear displacement $u(x)$ by the linear relationship as in Eq. (D.3). With the boundary condition of zero displacement at infinity, the shear displacement in the elastic part ($x > c$) is obtained in the form:

$$u(x) = A\exp\left(-\frac{\lambda x}{h_f}\right) \tag{D.9}$$

To determine the three coefficients in Eqs. (D.8) and (D.9), the traction boundary conditions at $x = 0$ and the continuity conditions at $x = c$ are applied as,

$$\sigma(x=0) = -\sigma_f,\ \sigma\left(x=c^-\right) = \sigma\left(x=c^+\right), \text{ and } u\left(x=c^-\right) = u\left(x=c^+\right) = \delta_0 \tag{D.10}$$

With an additional condition in Eq. (D.10), the damage zone size can also be determined.

We obtain the displacement in the two parts:

$$u(0<x<c) = \left(\frac{\sigma_f}{\bar{E}_f k}\tan(kc) + \frac{\delta_0 - \delta_c}{\cos(kc)}\right)\cos(kx) - \frac{\sigma_f}{\bar{E}_f k}\sin(kx) + \delta_c \tag{D.11}$$

$$u(x>c) = \delta_0 \exp\left(-\lambda\frac{x-c}{h_f}\right) \tag{D.12}$$

In addition, the damage zone size c is governed by:

$$\cos(kc) + \sqrt{2\xi - 1}\sin(kc) = \frac{\lambda\sigma_f}{\hat{\tau}} \tag{D.13}$$

The shear displacement at the root of the channel crack is thus

$$u(0)=\delta_c-\frac{\delta_c-\delta_0}{\cos(kc)}+\frac{\sigma_f}{\overline{E}_f k}\tan(kc) \tag{D.14}$$

Initiation of interfacial delamination is predicted when $u(x=0)=\delta_c$, which gives the critical stress in the dimensionless form

$$\frac{\sigma_c}{\hat{\tau}}=\frac{\sqrt{2\xi-1}}{\lambda\sin(kc_f)} \tag{D.15}$$

where c_f is the final damage zone. Plug Eq. (D.15) into (D.13), c_f can be solved by the equation,

$$\cos(kc_f)\left[1-\sqrt{2\xi-1}\frac{\cos(kc_f)}{\sin(kc_f)}\right]=0 \tag{D.16}$$

Eqs. (D.12) and (D.13) show that for fixed elastic stiffness K_0, the size of the fully formed damage zone, and consequently the normalized critical normal traction, at delamination initiation only depend on the fracture length scale, which is proportional to the normalized value $K_0\Gamma_i/\hat{\tau}^2$.

Note that the above shear-lag model assumes the rigid substrate. To consider the substrate deformation, an integral equation governing the interfacial shear stress is to be solved [38].

Bibilography

1. Ho, P.S., Wang, G., Ding, M., Zhao, J.H., Dai, X., *Reliability issues for flip-chip packages.* Microelectronics Reliability, 2004. **44**: p. 719-737.
2. Liu, X.H., Lane, M.W., Shaw, T.M., Liniger, E.G., Rosenberg, R.R., Edelstein, D.C., *Low-k BEOL mechanical modeling.* Advanced Metallization Conference, 2004: p. 361-367.
3. Wagner, S., Lacour, S.P., Jones, J., Hsu, P.I., Sturm, J.C., Li, T., Suo, Z., *Electronic skin: architecture and components.* Physica E, 2004. **25**: p. 326-334.
4. Khang, D.Y., Jiang, H.Q., Huang, Y., Rogers, J.A., *A stretchable form of single-crystal silicon for high-performance electronics on rubber substrate.* Science, 2006. **311**: p. 208-212.
5. Lacour, S.P., Jones, J., Wagner, S., Li, T., Suo, Z., *Stretchable interconnects for elastic electronic surfaces.* Proceedings of the IEEE, 2005. **93**: p. 1459-1467
6. Rogers, J.A., Someya, T., Huang, Y., *Materials and Mechanics for Stretchable Electronics.* Science, 2010. **327**: p. 1603-1607
7. Gao, H., *Application of fracture mechanics concepts to hierarchical biomechanics of bone and bone-like materials.* International Journal of Fracture, 2006. **138**: p. 101-137.
8. Genzer, J., Groenewold, J., *Soft matter with hard skin: from skin wrinkles to templating and material characterization.* Soft Matter 2006. **2**: p. 310-323
9. Bowden, N., Brittain, S., Evans, A.G., Hutchinson, J.W., Whitesides, G.M., *Spontaneous formation of ordered structures in thin films of metals supported on an elastomeric polymer.* Nature, 1998. **393**: p. 146-149
10. Watanabe, M., Shirai, H., Hirai, T., *Wrinkled polypyrrole electrode for electroactive polymer actuators.* Journal of Applied Physics, 2002. **92**: p. 4631-4637.
11. Harrison, C., Stafford, C.M., Zhang, W., Karim, A., *Sinusoidal phase grating created by a tunably buckled surface.* Applied Physics Letters, 2004. **85**: p. 4016-

4018.

12. Chan, E.P., Smith, E.J., Hayward, R.C., Crosby, A.J., *Surface wrinkles for smart adhesion* Advanced Materials, 2008. **20**: p. 711-716.
13. Chan, E.P., Page, K.A., Im, S.H., Patton, D.L., Huang, R., Stafford, C.M., *Viscoelastic properties of confined polymer films measured via thermal wrinkling.* Soft Matter, 2009. **5**: p. 4638-4641.
14. Stafford, C.M., Harrison, C., Beers, K.L., Karim, A., Amis, E.J., VanLandingham, M.R., Kim, H.C., Volksen, W., Miller, R.D., Simonyi, E.E., *A buckling-based metrology for measuring the elastic moduli of polymeric thin films.* Nature Materials, 2004. **3**: p. 545-550
15. Chung, J.Y., Nolte, A.J., Stafford, C.M., *Surface wrinkling: a versatile platform for measuring thin-film properties.* Advanced Materials 2011. **23**: p. 349-368
16. Stafford, C.M., Vogt, B.D., Harrison, C., Julthongpiput, D., Huang, R., *Elastic moduli of untrathin amorphous polymer films.* Macromolecules, 2006. **39**: p. 5095-5099.
17. Moon, M.W., Chung, J.W., Lee, K.R., Oh, K.H., Wang, R., Evans, A.G., *An experimental study of the influence of imperfections on the buckling of compressed thin films.* Acta Materialia, 2002. **50**: p. 1219-1227.
18. Cotterell, B., Chen, Z., *Buckling and cracking of thin films on compliant substrates under compression.* International Journal of Fracture, 2000. **104**: p. 169-179.
19. Parry, G., Colin, J., Coupeau, C., Foucher, F., Cimetiere, A., Grilhe, J., *Effect of substrate compliance on the global unilateral post-buckling of coatings: AFM observations and finite element calculations.* Acta Materialia, 2005. **53**: p. 441-447.
20. Vella, D., Bico, J., Boudaoud, A., Roman, B., Reis, P.M., *The macroscopic delamination of thin films from elastic substrates.* Proceedings of the National Academy of Sciences, 2009. **106**: p. 10901-10906.
21. Nolte, A.J., Chung, J.Y., Stafford, C.M., *Wrinkling delamination of thin polymer*

films on compliant substrates. Submitted for review, 2011.

22. Faulhaber, S., Mercer, C., Moon, M.W., Hutchinson, J.W., Evans, A.G., *Buckling delamination in compressed multilayers on curved substrates with accompanying ridge cracks.* Journal of Mechanics and Physics of Solids, 2006. **54**: p. 1004-1028.
23. Aoyanagi, Y., Hure, J., Bico, J., Roman, B., *Random blisters on stickers: metrology through defects.* Soft Matter, 2010. **6**: p. 5720-5728.
24. Cook, R.F., Liniger, E.G., *Stress-corrosion cracking of low-deilectric-constant spin-on-glass thin film.* Journal of the Electrochemical Society, 1999. **146**: p. 4439-4448.
25. Tsui, T.Y., McKerrow, A.J., Vlassak, J.J., *Constraint effects on thin film channel cracking behavior.* Journal of Materials Research, 2005. **20**: p. 2266-2273.
26. Beuth, J.L., *Cracking of thin bonded film in residual tension.* International Journal of Solids and Structures, 1992. **29**: p. 63-191
27. Huang, R., Prevost, J.H., Suo, Z., *Channel-cracking of thin films with the extended finite element method.* Engineering Fracture Mechanics, 2003. **70**: p. 2513-2526.
28. Kattamis, A.Z., Cherenack, K.H., Cheng, I.C., Long, K., Sturm, J.C., Wagner, S., *Fracture mechanisms of SiNx thin-films on compliant substrates.* Material Research Society Symposium Proceedings 2008: p. 1078-M14-02.
29. Chow, W.W.Y., Lei, K.F., Shi, G., Li, W.J., Huang, Q., *Microfluidic channel fabrication by PDMS-interface bonding.* Smart Materials and Structures., 2007. **15**: p. S112-S116.
30. Huh, D., Mills, K.L., Thouless, M.D., Takayama, S., *Tunable elastomeric nanochannels for nanofluidic manipulation.* Nature Materials, 2007. **6**: p. 424-428.
31. Zhu, X.Y., Mills, K.L., Peters, P.R., Bahng, J.H., Liu, E.H., Shim, J., Naruse, K., Csete, M.E., Thouless, M.D., Takayama, S., *Fabrication of reconfigurable protein matrices by cracking.* Nature Materials, 2005. **4**: p. 403-406.
32. Mills, K.L., Zhu, X., Takayama, S., Thouless, M.D., *The michanical properties of a surface-modified layer on poly (dimethylsiloxane).* Journal of Materials

Research 2008. **23**: p. 37-48.

33. Uchida, T., Mills, K.L., Kuo, C.H., Tung, Y.C., Garner, A.L., Koide, K., Thouless, M.D., Takayama, S., *External compression-induced fracture patterning on the surface of poly (dimethylsiloxane) cubes and microspheres.* Langmuir, 2009. **25**: p. 3102-3107.
34. Alaca, B.E., Sehitoglu, H., Saif, T.M., *Guided self-assembly of metallic nanowires and channels.* Applied Physics Letters, 2004. **84**: p. 4669.
35. Mani, S., Saif, T.M., *Mechanism of controlled crack formation in thin-film dielectrics.* Applied Physics Letters, 2005. **86**: p. 201903.
36. Adelung, R., Aktas, O.C., Franc, J., Biswas, A., Kunz, R., Elbahri, M., Kanzow, J., Schurmann, U., Faupel, F., *Strain-controlled growth of nanowires within thin-film cracks.* Nature Materials, 2004. **3**: p. 375-379.
37. He, J., Xu, G., Suo, Z., *Experimental determination of crack driving forces in integrated structures.* Proc. 7th Int. Workshop on stress-induced phenomena in metallization, 2004: p. 3-14.
38. Freund, L.B., Suresh, S., *Thin film materials: stress, defect deformation and surface evolution*. 2003, London Cambridge University Press.
39. Hutchinson, J.W., Suo, Z., *Mixed-mode cracking in layered materials.* Advances in Applied Mechanics, 1992. **29**: p. 63-191.
40. Williams, M.L., *The stress around a fault or crack in dissimilar media.* Bulletin of the Seismological Society of America, 1959. **49**: p. 199-204
41. Cherepanov, G.P., *The propagation of cracks in a continuous medium, Journal of Applied Mathematics and Mechanics.* Journal of Applied Mathematics and Mechanics, 1967. **31**: p. 503-512.
42. England, A.H., *A crack between dissimilar media.* Journal of Applied Mechanics, 1965. **32**: p. 400-402
43. Erdogan, F., *Stress distribution in bonded dissimilar materials with cracks.* Journal of Applied Mechanics, 1965. **32**: p. 403-410
44. Rice, J.R., Shi, G.C., *Plane problems of crack in dissimilar media.* Journal of

Applied Mechanics, 1965. **32**: p. 418-423.

45. Rice, J.R., *Elastic fracture mechanics concepts for interfacial cracks.* Journal of Applied Mechanics, 1988. **55**: p. 98-103
46. Dundars, J., *Edge-bonded dissimilar orthogonal elastic wedges.* Journal of Applied Mechanics, 1969. **36**: p. 650-652
47. Rice, J.R., *A path independent integral and the approximate analysis of strain concentration by notches and cracks.* Journal of Applied Mechanics, 1968. **35**: p. . 379-386.
48. Thouless, M.D., *Fracture of a model interface under mixed-mode loading.* Acta Metallurgica Materialia 1990. **38**: p. 1135-1140.
49. Wang, J.S., Suo, Z., *Experimental determination of interfacial toughness using brazol-nut-sandwich.* Acta Metallurgica et Materialia, 1990. **38**: p. 1279-1290.
50. Liechti, K.M., Chai, Y.S., *Asymmetric shielding in interfacial fracture under in-plane shear.* Journal of Applied Mechanics, 1992. **59**: p. 295-304.
51. Liechti, K.M., Chai, Y.S., *Biaxial loading experiments for determining interfacial toughness.* ASME Journal of applied mechanics, 1991. **58**: p. 680-687.
52. Needleman, A., *A continuum model for void nucleation by inclusion debonding.* Journal of Applied Mechanics, 1987. **54**: p. 525-553.
53. Tvergaard, V., Hutchinson, J.W., *The relation between crack growth resistance and fracture process parameters in elastic-plastic solids.* Journal of Mechanics and Physics of Solids, 1992. **40**: p. 1377-1397
54. Davila, C.G., Camanho, P.P., De Moura, M.F. *Mixed-mode decohesion elements for analysis of progressive delamination*. in *42nd AIAA/ASME/ASCE/AHS/ASC structures, structural dynamics and material conference*. 2001. Washington: USA: AIAA-01-1486.
55. Camanho, P.P., Davila, C.G., Pinho, S.T., *Fracture analysis of composite co-cured structural joints using decohesion elements.* Fatigue and Fracture of Engineering Materials and Structures, 2004. **27**: p. 745-757.
56. van Hal, B.A.E., Peerlings, R.H.J., Geer, M.G.D., van der Sluis, O., *Cohesive*

zone modeling for structural integrity analysis IC interconnects. Microelectronics Reliability, 2007. **47**: p. 1251-1261.

57. Parmigiani, J.P., Thouless, M.D., *The effects of cohesive strength and toughness on mixed-mode delamination of beam-like geometries.* Engineering Fracture Mechanics, 2007. **74**: p. 2675-2699
58. Mohammed, I., Liechti, K. M., *Cohesive zone modeling of crack nucleation at bimaterial corners.* Journal of Mechanics and Physics of Solids, 2000. **48**: p. 735-764.
59. Barenblatt, G.I., *The formation of equilibrium cracks during brittle fracture.* Journal of Applied Mathematics and Mechanics, 1959. **23**: p. 622-636
60. Dugdale, D.S., *Yielding of steel sheets containing slits.* Journal of Mechanics and Physics of Solids, 1960. **8**: p. 100-104.
61. Barenblatt, G.I., *The mathematical theory of equilibrium cracks in brittle fracture.* Advances in Applied Mechanics, 1962. **7**: p. 55-129.
62. Cottrell, A.H., *Mechanics of fracture.* Tewksbry Symposium on Fracture, 1963: p. 1-27.
63. Bao, G., Suo, Z., *Remarks on crack-bridging concepts.* Applied Mechanics Review, 1992. **45**: p. 355-366
64. Hutchinson, J.W., Evans, A.G., *Mechanics of materials: top down approaches to fracture.* Acta Materialia, 2000. **48**: p. 125-135.
65. Cox, B.N., Marshall, D.B., *The determination of crack bridging forces.* International Journal of Fracture, 1991. **49**: p. 159-176.
66. Sorensen, B.F., Jacobsen, T.K., *Determination of cohesive laws by the J-integral approach.* Engineering Fracture Mechanics, 2003. **70**: p. 1841-1858
67. Lane, M., Dauskardt, R.H., Vainchtein A., Gao, H, *Plasticity contributions to interface adhesion in thin-film interconnect structures.* Journal of Materials Research, 2000. **15**: p. 2758-2769.
68. ABAQUS. version 6.8, USA: Dassault Systemes Simulia Corp.: Providence, RI.
69. Wei, Y.G., Hutchinson, J.W., *Interface strength, work of adhesion and plasticity in*

peel test. International Journal of Fracture, 1998. **93**: p. 315-333

70. de Moura, M.F.S.F., Gonçalves, J.P.M., Marques, A.T., de Castro, P.M.S.T., *Prediction of compressive strength of carbon–epoxy laminates containing delamination by using a mixed-mode damage model.* Composites Structures, 2000. **50**: p. 151-157
71. Reddy Jr, E.D., Mello, F.J., Guess, T.R., *Modeling the initiation and growth of delaminations in composite structures.* Journal of Composite Materials, 1997. **31**: p. 812-831
72. Chen, J., Crisfield, M.A., Kinloch, A.J., Busso, E.P., Matthews, F.L. , Qiu, Y., *Predicting progressive delamination of composite material specimens via interface elements.* Mechanics of Composite Materials and Structures, 1999. **6**: p. 301-317
73. Biot, M.A., *Folding instability of a layered viscoelastic medium under compression.* Proceedings of the Royal Society of London, 1957. **242**: p. 444-454.
74. Allen, H.G., *Analysis and Design of Structural Sandwich Panels*. 1969, New York: Pergamon Press.
75. Shield, T.W., Kim, K.S., Shield, R.T., *The buckling of an elastic layer bonded to an elastic substrate in plane strain.* Journal of Applied Mechanics, 1994. **61**: p. 231-235.
76. Groenewold, J., *Wrinkling of plates coupled with soft elastic media.* Physica, 2001. **A298**: p. 32-45.
77. Huang, R., Suo, Z., *Instability of a compressed elastic film on a viscous layer.* International Journal of Solids and Structures, 2002. **39**: p. 1791-1802.
78. Chen, X., Hutchinson, J.W., *Herringbone buckling patterns of compressed thin films on compliant substrates.* Journal of Applied Mechanics, 2004. **71**: p. 597-603.
79. Huang, R., Im, S.H., *Dynamics of wrinkle growth and coarsening in stressed thin films.* Physical Review E, 2006. **74**: p. 026214.
80. Jiang, H.Q., Khang, D.Y., Song, J., Sun, Y., Huang, Y., Rogers, J.A., *Finite*

deformation mechanics in buckled thin films on compliant supports. Proceedings of the National Academy of Sciences, 2007. **104**: p. 15607-15612.

81. Lee, D., Triantafyllidis, N., Barbar, J.R., Thouless, M.D., *Surface instability of an elastic half space with material properties varying with depth.* Journal of Mechanics and Physics of Solids, 2008. **56**: p. 858-868.
82. Audoly, B., Boudaoud, A., *Buckling of a stiff film bound to a compliant substrate. Part I: formulation, linear stability of cylindrical patterns, secondary bifurcations.* Journal of the Mechanics and Physics of Solids, 2008. **56**: p. 2401-2421.
83. Im, S.H., Huang, R., *Wrinkle Patterns of Anisotropic Crystal Films on Viscoelastic Substrates.* Journal of Mechanics and Physics of Solids, 2008. **56**: p. 3315-3330.
84. Sun, J.Y., Xia, S., Moon, M.W., Oh, K.H., Kim, K.S., *Folding wrinkles of a thin stiff layer on a soft substrate.* Submitted for review, 2011.
85. Cai, S., Breid, D., Crosby, A.J., Suo, Z., Hutchinson, J.W., *Periodic patterns and energy states of buckled films on compliant substrates.* submitted for review, 2011.
86. Liang, J., Huang, R., Yin, H., Sturm, J.C., Hobart, K.D., Suo, Z., *Relaxation of compressed elastic islands on a viscous layer.* Acta Materialia, 2002. **50**: p. 2933-2944.
87. Mei, H., Huang, R., Chung, J.Y., Stafford, C.M., Yu, H.H., *Buckling modes of elastic thin films on elastic substrates.* Applied Physics Letters, 2007. **90**: p. 151902.
88. Goyal, S., Srinivasan, K., Subbarayan, G., Siegmund, T., *On instability-induced debond initiation in thin film systems.* Engineering Fracture Mechanics, 2010. **77**: p. 1298-1313.
89. Chai, H., Babcock, C.D., Knauss, W.G., *One dimensional modeling of failure in laminated plates by delamination buckling.* International Journal of Solids and Structures, 1981. **17**: p. 1069-1083.
90. Hutchinson, J.W., Thouless, M.D., Liniger, E.G., *Growth and Configurational Stability of Circular, Buckling-Driven Film Delaminations.* Acta Metallurgica et

Materialia, 1992. **40**: p. 295-308

91. Ortiz, M., Gioia, G., *Delamination of compressed thin films.* Advances in Applied Mechanics, 1997. **33**: p. 119-192.
92. Huang, Z.Y., Hong, W., Suo, Z., *Nonlinear analysis of wrinkling in a film bonded to a compliant substrate.* Journal of Mechanics and Physics of Solids, 2005. **53**: p. 2101-2118.
93. Huang, R., *Kinetic wrinkling of an elastic film on a viscoelastic substrate.* Journal of Mechanics and Physics of Solids, 2005. **53**: p. 63-89.
94. Coupeau, C., *Atomic force microscopy study of the morphological shape of thin film buckling.* Thin Solid Films, 2002. **406**: p. 190-194.
95. Yu, H.H., Hutchinson, J.W., *Influence of substrate compliance on buckling delamination of thin films.* International Journal of Fracture, 2002. **113**: p. 39-55.
96. Xia, Z.C., Hutchinson, J.W., *Crack patterns in thin films.* Journal of Mechanics and Physics of Solids, 2000. **48**: p. 1107-1131.
97. Ambrico, J.M., Begley, M.R., *The role of initial flaw size and plasticity in adjacent layers in channeling crack growth in thin films.* Thin Solid Films, 2002. **419**: p. 144-153
98. Zak, A.R., Williams, M.L., *Crack point stress singularities at a bi-material interface.* Journal of Applied Mechanics, 1963. **30**: p. 142-143.
99. Nakamura, T., Kamath, S.M. , *Three-dimensional effects in thin-film fracture mechanics.* Mechanics of Materials 1992. **13**: p. 67-77.
100. He, M.Y., Hutchinson, J.W., *Crack deflection at an interface between dissimilar elastic materials.* International Journal of Solids and Structures, 1989a. **25**: p. 1053-1067.
101. Ye, T., Suo, Z., Evans, A.G., *Thin film cracking and the roles of substrate and interface.* International Journal of Solids and Structures, 1992. **29**: p. 2639-2648
102. Yu, H.H., He, M.Y., Hutchinson, J.W., *Edge effects in thin film delamination.* Acta Materialia, 2001. **49**: p. 93-107.
103. Suo, Z., Hutchinson, J.W., *Interface crack between two elastic layers.*

International Journal of Fracture, 1990. **43**: p. 1-18.

104. Liu, X.H., Lane, M.W., Shaw, T.M., Simonyi, E., *Delamination in patterned films.* International Journal of Solids and Structures, 2007. **44**: p. 1706-1718.
105. Li, T., Suo, Z., *Ductility of thin metal films on polymer substrates modulated by interfacail adhesion.* International Journal of Solids and Structures, 2007. **44**: p. 1696-1705.
106. Flinn, B.D., Lo, C.S., Zok, F.W., Evans, A.G., *Fracture-resistance characteristics of a metal-toughened ceramic.* Journal of the American Ceramic Society, 1993. **76**: p. 369-375.
107. Mello, A.V., Liechti, K.M., *The effect of self-assembled monolayers on interfacial fracture.* Journal of Applied Mechanics, 2006. **73**: p. 860-870.
108. Li, S., Thouless, M.D., Waas, A.M., Schroeder, J.A., Zavattieri, P.D., *Use of a cohesive-zone model to analyze the fracture of a fiber-reinforced polymer-matrix composite.* Composites Science and Technology, 2005. **65**: p. 537-549.
109. Shirani, A., Liechti, K.M., *A calibrated fracture process zone model for thin film blistering.* International Journal of Fracture, 1998. **93**: p. 281-314.
110. Pandya, K.C., J.G. Williams, J.G., *Measurement of cohesive zone parameters in tough polyethylene.* Polymer engineering and science, 2000a. **40**: p. 1765-1776.
111. Pandya, K.C., Williams, J.G., *Cohesive zone modeling of crack growth in polymers. Part 1- experimental measurement of cohesive law.* Plastics, rubber and composites, 2000b. **29**: p. 439-446.
112. Pandya, K.C., Ivankovic, A., J.G. Williams, J.G., *Cohesive zone modeling of crack growth in polymers. Part 2- numerical simulation of crack growth.* Plastics, rubber and composites, 2000c. **29**: p. 447-452.
113. Li, V.C., Chan, C.M., Leung, C.K.Y., *Experimental determination of the tension softening relations for cementitious composites.* Cement and Concrete Research, 1987. **17**: p. 441-452.
114. Teramura, S., Nomura, N., Hashida, T., Takahashi, H., Mihashi, H., *Development of a core-based testing method for determining fracture energy and tension-*

softening relations of concrete. Micromechanics of failure of quasi-brittle materials, ed. S.P. Shah, Swartz, S.E., Wang, M.L. 1990, London: Elsevier Applied Science, London. 463-473.

115. Li, V.C., Ward, R., *A novel testing technique for post-peak tensile behavior of cementitious materials*. Fracture toughness and fracture energy-testing methods for concrete and rocks, ed. H. Mihashi, Takahashi, F.H., Wittmann, A.A. 1989: Balkema, Rotterdam. 183-195.
116. Leung, C.K.Y., Li, V.C., *Determination of fracture toughness parameter of quasi-brittle materials with laboratory-size specimens.* Journal of Materials Science, 1989. **24**: p. 854-862.
117. Rokugo, K., Iwasa, M., Seko, S., Koyanagi, W., *Tension softening diagrams of steel fiber reinforced concrete, in: Fracture of concrete and rock: recent developments*. Fracture of concrete and rock: recent developments, ed. S.P. Shah, Swartz, S.E., Barr, B. 1989, England: Elsevier Applied Science. 513-522.
118. Chong, K.P., Li, V.C., Einstein, H.H., *Size effects, process zone and tension softening behavior in fracture of geomaterials.* Engineering Fracture Mechanics, 1989. **34**: p. 669-678.
119. Li, V.C., Maalej, M., Hashida, T., *Experimental determination of the stress-crack opening relation in fibre cementitious composites with a crack-tip singularity.* Journal of materials science, 1994. **29**: p. 2719-2724.
120. Sorensen, B.F., *Cohesive law and notch sensitivity of adhesive joints.* Acta Materialia, 2002. **50**: p. 1053-1061.
121. Zhu, Y., Liechti, K.M., Ravi-Chandar, K., *Direct extraction of rate-dependent traction-separation laws for polyurea/steel interfaces.* International Journal of Solids and Structures, 2009. **46**: p. 31-51.
122. Tamuzs, V., Tarasovs, S., Vilks, U., *Progressive delamination and fiber bridging modeling in double cantilever beam composite specimen.* Engineering Fracture Mechanics, 2001. **68**: p. 513-525.
123. Gowrishankar, S., Mei, H., Liechti, K., Huang, R., *Determination of traction-*

separation relations of interfaces using interferometry. SRC TECHCON 2010, 2010.

124. Liechti, K.M., *On the use of classical interferometry techniques in fracture mechanics*. III ed. Experimental techniques in Fracure, ed. J.S. Epstein. 1993, New York: VCH Publishers. 95-124.
125. Kanninen, M.F., *An augmented double-cantilever beam model for studying crack propagation and arrest.* International Journal of Fracture, 1973. **9**: p. 83-92.
126. Williams, J.G., Hadavinia, H., *Analytical solutions for cohesive zone models.* Journal of the Mechanics and Physics of Solids, 2002. **50**: p. 809-825
127. Li, S., Wang, J., Thouless, M.D., *The effects of shear on delamination of beam-like geometries.* Journal of the Mechanics and Physics of Solids, 2004. **52**: p. 193-214.
128. Williams, J.G., *End corrections for orthotropic DCB specimens.* Composites Science and Technology, 1989. **35**: p. 367-376.
129. Carka, D., Landis, C.M., *The Dirichlet-to-Neumann map for two-dimensional crack problems. Computer Methods in Applied Mechanics and Engineering* Computer Methods in Applied Mechanics and Engineering, 2011. **200**: p. 1263-1271.
130. He, M.Y., Hutchinson, J.W., *Kinking of a crack out of an interface.* Journal of Applied Mechanics, 1989b. **56**: p. 270-278.
131. Hayashi, K., Nemat-Nasser S., *Energy-release rate and crack kinking under combined loading.* Journal of Applied Mechanics, 1981. **48**: p. 520-524.
132. Cotterell, B., *On brittle fracture paths.* International Journal of Fracture Mechanics, 1965. **1**: p. 96-103.
133. Cotterell, B., Rice, J.R., *Slightly curved and kinked cracks.* International Journal of Fracture, 1980. **16**: p. 155-169.

Vita

Haixia Mei was born in Huangmei, Hubei Province, China. After completing her classes at the 1st High School of Huangmei in 1997, she entered Beijing Institute of Technology and received her B.E. degree with honors in 2001. At the same year, she was admitted to the graduate school of Tsinghua University, Beijing, China, and received her M.E. degree in July 2004. She started her Ph.D. study in Civil Engineering Department at the University of Texas at Austin in August 2004. One year later, she transferred to the Department of Aerospace Engineering and Engineering Mechanics and continued her Ph.D. study in Professor Rui Huang' group.

Email address: hxmei@utexas.edu

This dissertation was typed by Haixia Mei.